

# Experimental Investigation of Unsteady Wake Structure of Bluff Bodies

by

Mostafa Rahimpour  
B.Sc., Persian Gulf University, Iran, 2006  
M.Sc., Shahid Bahonar University, Iran, 2009

A Dissertation Submitted in Partial Fulfillment  
of the Requirements for the Degree of

DOCTOR OF PHILOSOPHY

in the Department of Mechanical Engineering

© Mostafa Rahimpour, 2020  
University of Victoria

All rights reserved. This dissertation may not be reproduced in whole or in part, by  
photocopy or other means, without the permission of the author.

We acknowledge with respect the Lekwungen peoples on whose traditional territory the  
university stands and the Songhees, Esquimalt and WSÁNEĆ peoples whose historical  
relationships with the land continue to this day.

## Supervisory Committee

Experimental Investigation of Unsteady Wake Structure of Bluff Bodies

by

Mostafa Rahimpour  
B.Sc., Persian Gulf University, 2006  
M.Sc., Shahid Bahonar University, 2009

### Supervisory Committee

---

Dr. Peter Oshkai, Department of Mechanical Engineering  
**Supervisor**

---

Dr. Ned Djilali, Department of Mechanical Engineering  
**Departmental Member**

---

Dr. Curran Crawford, Department of Mechanical Engineering  
**Departmental Member**

---

Dr. Boualem Khouider, Department of Mathematics and Statistics  
**Outside Member**

## Abstract

### Supervisory Committee

Dr. Peter Oshkai, Department of Mechanical Engineering  
Supervisor

Dr. Ned Djilali, Department of Mechanical Engineering  
Departmental Member

Dr. Curran Crawford, Department of Mechanical Engineering  
Departmental Member

Dr. Boualem Khouider, Department of Mathematics and Statistics  
Outside Member

The interaction between a bluff body and the impinging fluid flow, can involve detached boundary layers, massive flow separations, free shear layers, development of recirculation zones and formation of a highly disturbed and complex region downstream of the bluff body, which can be categorized as wake. The present research aims to experimentally investigate such fluid-structure interaction and provide insight into the wake structure of two bluff bodies. To this end, the airwake over the helicopter platform of a Canadian Coast Guard (CCG) polar icebreaker was studied using high-speed particle image velocimetry (PIV). The experiments were conducted on a scaled model of the polar icebreaker situated on a custom-built and computer-controlled turntable, which provided the ability to accurately change the incidence angle of the impinging flow with a given rate of change for incidence angle. Quantitative flow field data were obtained in several vertical and horizontal planes. The obtained velocity field was then used to calculate the time-averaged flow structure and turbulence metrics over the helicopter platform of the vessel. The present work compared the effects of two types of inflow conditions: (i) a uniform flow and (ii) a simulated atmospheric boundary layer (ABL) on the flow structure over the helicopter platform of the ship. Moreover, for the bluff scaled model, the effects of the Reynolds number on the wake structure and the flow patterns were investigated. The incidence angle ( $\alpha$ ) between the oncoming flow and the orientation of the ship varied between  $0^\circ$  to  $330^\circ$  with the increment of  $30^\circ$ . It was observed that higher maximum values

of the turbulence intensity were associated with the simulated ABL. Moreover, it was found that for both inflow conditions, the incidence angle of  $300^\circ$  corresponded to the highest turbulence levels over the helicopter platform. Building on the results obtained for a stationary vessel in the simulated ABL, this work aimed to quantify the effects of the unsteady change in the direction of the impinging wind, simulated by rotating the model at a certain rate,  $\dot{\alpha}$ . It was observed that the increase of the rate of change of the inflow direction resulted in an increase of the turbulent intensity over the helicopter platform. However, an exception was observed for the case of  $\alpha = 60^\circ$ , where clockwise rotation of the ship model with respect to the inflow exposed the helicopter platform to increased turbulent velocity fluctuations, while counterclockwise rotation diminished the flow unsteadiness over the helicopter platform. Moreover, aiming to identify the origins of the unsteady forces applied on bluff elongated plates with high chord-to thickness ratio ( $c/t = 23$ ) at zero incidence, direct force measurement as well as PIV were used to identify the effect of transverse perforations on the flow-induced loading on the flow structure in the near-wake of the plates. The experiments were conducted in a water channel, where the plates were located at the center of channel, parallel to the upstream flow direction. Plates with various characteristic diameter of the perforation as well as a reference case without perforations were considered. The spectra of the trailing-edge vortex shedding and flow-induced forces were compared and it was observed that the vortex shedding frequencies were in very good agreement with those of the measured flow-induced forces for all considered perforation patterns. Thus, it was determined that the trailing-edge vortex shedding was the main mechanism of generating the unsteady loading on the plates. The staggered patterns of the perforations created a three-dimensional flow structure at the vicinity of the trailing edge and in the near wake, which was investigated using PIV at several data acquisition planes. It was found that in the cross-sectional planes corresponding to the close proximity of the perforations to the downstream edge, the periodic trailing-edge vortex shedding were suppressed. Furthermore, it was observed that for small perforations, the velocity fluctuations in the near wake were enhanced. However, further increase of the perforation diameter led to suppression of the velocity fluctuations.

**Keywords:** Ship airwake; Perforated plate; flow-induced loading; wake structure; PIV.

## Table of Contents

Supervisory Committee .....	ii
Abstract .....	iii
Table of Contents .....	v
List of Figures .....	viii
Nomenclature .....	xi
Acknowledgments .....	xiii
Dedication .....	xiv
<b>1 Introduction.....</b>	<b>1</b>
1.1 Background and Motivation .....	1
1.1.1 Bluff body wake dynamics .....	1
1.1.2 Ship airwake.....	6
1.1.3 Wake of perforated plates .....	10
1.2 Methodology .....	15
1.2.1 Flow facility .....	15
1.2.2 Experimental apparatus.....	16
1.2.3 Measurement techniques.....	22
1.3 Research Contributions .....	24
1.4 Dissertation Outline .....	26
<b>2 Experimental Investigation of Airflow over the Helicopter Platform of a Polar Icebreaker.....</b>	<b>28</b>
Preamble .....	28
Abstract.....	29
2.1 Introduction.....	29
2.2 Experimental system and techniques .....	34
2.2.1 Inflow conditions .....	34
2.2.2 Scaled model.....	35
2.2.3 Quantitative flow imaging .....	36
2.3 Results and discussion .....	40

2.3.1	Effects of Reynolds number.....	40
2.3.2	Effect of the incidence angle.....	52
2.4	Conclusions.....	63
3	The effects of unsteady change in wind direction on the airflow over the helicopter platform of a polar icebreaker.....	64
	Preamble .....	64
	Abstract.....	65
3.1	Introduction.....	65
3.2	Experimental system and techniques .....	67
3.2.1	Inflow conditions .....	67
3.2.2	Scaled model.....	69
3.2.3	Quantitative flow imaging and phase-averaging .....	72
3.3	Results and discussion .....	73
3.3.1	Effect of the rate of change of the incidence angle.....	73
3.4	Conclusions.....	87
4	Flow-induced loading on and unsteady flow structure in the wake of bluff perforated plates at zero incidence .....	89
	Preamble .....	89
	Abstract.....	90
4.1	Introduction.....	90
4.2	Experimental systems and techniques .....	92
4.2.1	Flow facility .....	92
4.2.2	Perforated plates.....	94
4.2.3	Force measurements.....	95
4.2.4	Flow velocity measurements.....	95
4.2.5	Time-averaging of PIV images .....	96
4.3	Results and discussion .....	97
4.3.1	Flow-induced loading on plates .....	97
4.3.2	Separated flow structure .....	102
4.4	Conclusions.....	118
5	Conclusions and future works.....	120

- 5.1 Ship airwake..... 120
  - 5.1.1 Key findings..... 120
  - 5.1.2 Future work..... 122
- 5.2 Wake of perforated plates ..... 122
  - 5.2.1 Key findings..... 123
  - 5.2.2 Future work..... 124
- Bibliography ..... 125
- Appendix A Uncertainty of PIV measurements ..... 134
- Appendix B Permission letters for copyrighted materials ..... 137

## List of Figures

Fig. 1-1. Canadian Coast Guard (CCG) icebreaker (VardMarine, 2019).....	2
Fig. 1-2. The rotary flow-control valve: (a) simplified schematics (Bossi, 2016) and (b) valve assembly (Bossi and Malavasi, 2014).....	2
Fig. 1-3. (a) Two-dimensional (Bardera-Mora, 2014a) and (b) three-dimensional backward-facing step (Tinney and Ukeiley, 2009).....	4
Fig. 1-4. The water channel at the Fluids Dynamics Research Laboratory at the Department of Mechanical Engineering of University of Victoria. ....	16
Fig. 1-5. The schematics of the scaled model of CCG icebreaker: (a) side view, (b) plan view (c) closeup of the superstructure. ....	17
Fig. 1-6. Schematic of flow conditioning elements. ....	18
Fig. 1-7. Schematic of the experimental system, including main components of the PIV system. ....	21
Fig. 1-8. Schematic of the perforated plate.....	21
Fig. 2-1. Schematic of flow conditioning elements. ....	36
Fig. 2-2. Distribution of time-averaged streamwise velocity in the simulated ABL.....	36
Fig. 2-3. The schematics of CCG icebreaker: (a) side view, (b) plan view (c) closeup of the superstructure.....	37
Fig. 2-4. Schematic of the experimental setup: (a) vertical (b) horizontal data acquisition planes. ....	38
Fig. 2-5. Time-averaged streamlines and contours of out-of-plane vorticity at $y = 0$ : (a), (c), (e) - uniform inflow; (b), (d), (f) – ABL.....	41
Fig. 2-6. Location of the reattachment points on the helicopter platform for recirculation zones $A_2$ and $B_2$ . ....	44
Fig. 2-7. Time-averaged velocity distribution at the centerline of the helicopter platform ( $y_{PIV}/L=0$ ).....	45
Fig. 2-8. Components of the Reynolds stress tensor at the centerline of the helicopter platform ( $y_{PIV}/L = 0$ ) as functions of the downstream distance ( $x/L$ ) at two elevations above the platform: (a), (c), (e) - uniform inflow; (b), (d), (f) - simulated ABL.....	49

Fig. 2-9. Components of the Reynolds stress tensor at the centerline of the helicopter platform ( $y_{PIV}/L = 0$ ) as functions of the elevation above the platform ( $z/L$ ) at: (a), (c), (e) - uniform inflow; (b), (d), (f) - simulated ABL.....	51
Fig. 2-10. Maximum values of turbulence intensity: (a) - uniform inflow, (b) - simulated ABL.....	54
Fig. 2-11. Location of the peak values of turbulence intensity $I_u$ , max, (a) – x-y plane (b) – x-z plane.....	55
Fig. 2-12. Location of the peak values of turbulence intensity $I_w$ , max, (a) – x-y plane (b) – x-z plane.....	56
Fig. 2-13. Variation of turbulence intensities, $I_u$ and $I_w$ , at the center of the flight deck, with the incidence angle: (a), (c) - uniform inflow; (b), (d) - simulated ABL.....	57
Fig. 2-14. Time-averaged streamlines and contours of the out-of-plane vorticity in the x-y plane at $z_{PIV}/L = 0.25$ : (a), (c), (e) - uniform inflow; (b), (d), (f) - simulated ABL.....	58
Fig. 2-15. Time-averaged streamlines and contours of the out-of-plane vorticity in the x-y plane at $z_{PIV}/L = 0.40$ : (a), (c), (e) - uniform inflow; (b), (d), (f) - simulated ABL.....	61
Fig. 3-1. Schematic of the experimental setup.....	68
Fig. 3-2. Distribution of (a) time-averaged streamwise velocity component and (b) streamwise turbulence intensity in the simulated ABL. ....	70
Fig. 3-3. Schematics of the CCG icebreaker: (a) side view, (b) plan view, (c) closeup of the superstructure (d) definition of reference frame for the inflow incidence angle. ....	71
Fig. 3-4. Time-averaged streamlines and contours of out-of-plane vorticity at $\alpha = 0^\circ$ , at $y_{PIV} = 0$ : (a) $\dot{\alpha}L/U = 0$ , (b) $\dot{\alpha}L/U = 0.083$ , (c) $\dot{\alpha}L/U = 0.167$ , (d) $\dot{\alpha}L/U = 0.25$ .....	74
Fig. 3-5. Time-averaged streamlines and contours of out-of-plane vorticity at $\alpha = 60^\circ$ , at $y_{PIV} = 0$ : (a) $\dot{\alpha}L/U = 0$ , (b) $\dot{\alpha}L/U = 0.083$ , (c) $\dot{\alpha}L/U = 0.167$ , (d) $\dot{\alpha}L/U = 0.25$ , (e) $\dot{\alpha}L/U = -0.167$ , (f) $\dot{\alpha}L/U = -0.25$ . ....	78
Fig. 3-6. Maximum values of turbulence intensity $I_u$ and $I_w$ , as a function of the rate of change of the incident flow direction at: (a) $\alpha = 0^\circ$ and (b) $\alpha = 60^\circ$ .....	84
Fig. 3-7. Variation of turbulence intensities: $I_u$ (a) and $I_w$ (b) at the center of the helicopter platform, as a function of the rate of change of the incident flow direction at $\alpha = 0^\circ$ .....	85

Fig. 3-8. Variation of turbulence intensities: $I_u$ (a) and $I_w$ (b) at the center of the helicopter platform, as a function of the rate of change of the incident flow direction at $\alpha = 60^\circ$ ....	86
Fig. 4-1. Schematic of the experimental system. ....	93
Fig. 4-2. Schematic of the perforated plate. ....	93
Fig. 4-3. Perforated patterns P1 (a), P2 (b) and P3 (c). ....	94
Fig. 4-4. Schematic of the perforation patterns and location of the PIV data acquisition planes (DAPs). ....	96
Fig. 4-5. Variation of the mean drag coefficient as a function of the Reynolds number (Bossi et al., 2017a). ....	98
Fig. 4-6. Variation of the fluctuating lift coefficient as a function of the Reynolds number (Bossi et al., 2017a). ....	99
Fig. 4-7. Power spectral density of the flow-induced loading on the plates as a function of the inflow velocity and frequency: (a) P0, (b) P1, (c) P2 and (d) P3. ....	100
Fig. 4-8. Strouhal number of the unsteady loading as a function of Reynolds number. ....	102
Fig. 4-9. Leading-edge separation bubble, $U = 0.55$ m/s: (a) P0 and (b) P3, DAP2. ....	103
Fig. 4-10. Dimensionless reattachment length as a function of Reynolds number. ....	104
Fig. 4-11. Power spectral density for transverse flow velocity fluctuations as a function of the inflow velocity and frequency for (a) P0, (b) P1, (c) P2, (d) P3. The data for the plates P1, P2, P3 correspond to DAP2. ....	106
Fig. 4-12. Strouhal number of the unsteady loading as a function of Reynolds number. ....	108
Fig. 4-13. Dimensionless distribution of the rms of the transverse velocity fluctuations in the wake of the perforated plates, $U = 0.55$ m/s, in DAP1: P1 (a), P2 (b) and P3 (c). ....	109
Fig. 4-14. Variation of the maximum of the rms of the transverse dimensionless velocity fluctuation as a function of the perforation diameter at DAP1. ....	110
Fig. 4-15. Variation of the wake width as a function of the Reynolds number for the perforated plate P3. ....	112
Fig. 4-16. Boundary layer at different upstream velocities: — solid plate, $\circ$ perforated plate P3 ( $\delta_h = 19.5$ mm) at DAP1 (a), DAP2 (b) and DAP3 (c). ....	113
Fig. 4-17. Distribution of the rms of the transverse dimensionless velocity fluctuations in the wake of the plate, $U = 0.55$ m/s: Solid plate (a); Perforated plate P3: DAP1 (b), DAP2 (c) and DAP3 (d). ....	115

## Nomenclature

$A_t$	Total wetted area
$A_p$	Area of an individual perforation
$\overline{C_D}$	Mean drag coefficient
$C_L'$	Fluctuating lift coefficient
$\overline{D}$	Mean drag force
$E$	Modulus of elasticity
$G$	Modulus of rigidity
$I$	Turbulence intensity
$K_R$	Rayleigh conductivity
$L$	Characteristic length
$L_r$	leading-edge reattachment length
$N$	Number of PIV image pairs
Re	Reynolds number
$R$	Perforation radius
$R_{uu}, R_{vv}, R_{ww}, R_{uw}, R_{vw}$	Components of Reynolds stress tensor
St	Strouhal number
$U$	Characteristic Velocity
$W$	Free surface level
$X_{PIV}, Y_{PIV}, Z_{PIV}$	PIV coordinate system
$c$	Chord length
$d'$	Wake width
$f$	Frequency
$f_0$	Natural vibrational frequency
$l'$	Fluctuating lift force
$n$	Number of perforations
$t$	Thickness
$u, v, w$	Components of velocity vector

$u_x, u_y, u_z$	Components of velocity vector
$u', v', w'$	Fluctuating components of velocity vector
$x_r$	Location of reattachment point
$z^*$	Vertical location in atmospheric boundary layer

### **Greek letters**

$\alpha$	Incidence angle
$\dot{\alpha}$	Rate of rotation
$\beta$	Equivalent area ratio
$\delta$	Boundary layer thickness
$\delta_h$	Perforation diameter
$\sigma$	Standard deviation
$\rho$	Density
$\mu$	Dynamic viscosity
$\nu$	Kinematic viscosity
$\omega$	Out-of-plane vorticity

### **Subscripts**

$LC$	Load cell
$PIV$	Particle image velocimetry
$ref$	Reference
$rms$	Root mean square
$u$	Velocity component in x-direction
$v$	Velocity component in y-direction
$w$	Velocity component in z-direction

## Acknowledgments

I would like to express my sincere gratitude to my PhD supervisor, Prof. Peter Oshkai for his thoughtful consideration, continuous support and valuable mentorship. His deep insight, extensive knowledge and infinite guidance brightened my way throughout my PhD studies. I acknowledge his inspirations and immeasurable patience and care and I will never forget many lessons he thought me.

Further to this, I would like to acknowledge the valuable contributions of Prof. Stefano Malavasi, Dr. Filippo Carlo Bossi and Dr. Oleksandr Barannyk. Their support was essential for the present research.

I am also extending my earnest appreciation to Prof. Zuomin Dong for his limitless support towards my graduate studies. I will be forever proud to be a member of his team and have him as my mentor and guide.

Moreover, I extend special thanks to the dedicated staff at the Institute for Integrated Energy Systems at the University of Victoria (IESVic), Ms. Susan Walton, Ms. Pauline Shepherd and Ms. Peggy White, Senior Scientific Assistants at Department of Mechanical Engineering of the University of Victoria, Mr. Rodney Katz and Mr. Patrick Chang as well as my friends and colleagues at the Engineering and Computer Science Co-operative Education Office of the University of Victoria.

I am also grateful to my friends Dr. Alireza Akhgar, Dr. Majid Soleimani nia, Mr. Amin Cheraghi, Dr. Behnam Rahimi, Dr. Afshin Jooshesh, Dr. Hamed Akbari Khorami, Mr. Kevin Andersen, Mr. Jonathan Reaume, Mr. Andrew Richards and Mr. Dylan Iverson.

I also gratefully acknowledge the financial support of the Natural Sciences and Engineering Research Council of Canada (NSERC) as well as contributions of VARD Group and PIBIVIESSE S.R.L.

## Dedication

*To my Family*

*Your love warms my heart, your wisdom lights my way and your encouragement moves me forward.*

# 1 Introduction

## 1.1 Background and Motivation

This section provides an overview of the previous work and the state-of-the art as relevant to the bluff body configurations investigated in this research. Additionally, the motivation and the novelty of the present study are discussed in the following sections. Parts of this chapter are repeated in the subsequent chapters corresponding to the published journal articles based on the present research.

### 1.1.1 Bluff body wake dynamics

The interaction between fluid flow and a body can create a region downstream of the body known as wake, which is associated with change in velocity field compared with the upstream. In this research, the wake of bluff, or non-streamlined, bodies were investigated, where the wake region was associated with flow separation from the body creating a region of disturbed and highly unsteady flow downstream of the body. Such region, herein called bluff body wake or simply wake, often contains many complex phenomena such as boundary layer separation and reattachment, vortex shedding, free shear layers, and high turbulence (Roshko, 1993). Examples of bluff body wake can be found in the interaction between atmospheric wind with large-scale structures such as vehicles (Bearman, 1980; Al-Garni and Bernal, 2010), buildings (Hertwig et al., 2019), bridges (Diana et al., 2013), wind turbines (Hu et al., 2012), and vessels and ship superstructures (Shukla et al., 2019). Furthermore, many engineering applications involve bluff body wake, such as internal flow applications and the interaction between the impinging working fluid with components of the flow control valves, air-conditioning systems and heat exchangers (Derakhshandeh and Alam, 2019).

In the present research, the wake of two bluff body configurations, a scaled model of a Canadian Coast Guard (CCG) icebreaker (Fig. 1-1) as well as perforated plates used in a rotary flow-control valve (Fig. 1-2), were investigated. In order to have a better

understanding of the physics and the origins of wake of these bluff bodies, it is useful to draw analogy between these configurations and the benchmarked bluff geometry of backward-facing step (Eaton and Johnston, 1982; Reddy et al., 2000) and bluff rectangular plate (Kiya and Sasaki, 1983; Cherry et al. 1984; Welsh et al., 1984; Stokes and Welsh, 1986; Nakamura et al. 1991), where in sufficiently large Reynolds number the wake of the considered bluff configurations is mainly the result of separation of the boundary layers at the sharp edges of the body, which in turn can lead to increased velocity fluctuations in the wake region.



Fig. 1-1. Canadian Coast Guard (CCG) icebreaker (VardMarine, 2019).

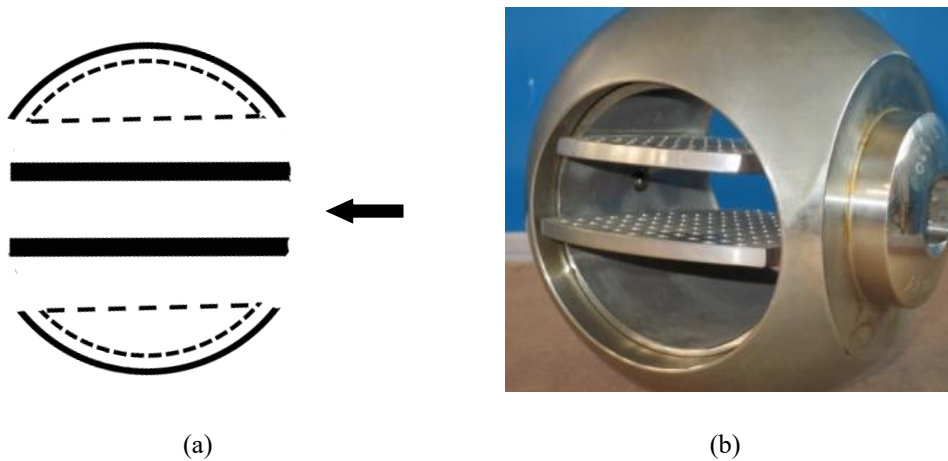


Fig. 1-2. The rotary flow-control valve: (a) simplified schematics (Bossi, 2016) and (b) valve assembly (Bossi and Malavasi, 2014).

The CCG icebreaker can be considered as a modified backward-facing step configuration (Reddy et al., 2000; Tinney and Ukeiley, 2009; Bardera-Mora, 2014a). In a simplified two-dimensional case and with no crosswind (Fig. 1-3(a)), the step represents the hanger and the helicopter platform of the vessel. Despite simple geometry, backward-facing step exhibits a complex flow (Aider et al. 2007): The boundary layer developed over the step always separates at the edge and creates an unsteady shear layer downstream of the edge, which can give rise to spanwise Kelvin–Helmholtz vortices. Eventually the shear layer reattaches to the bottom wall, which leads to creation of a recirculation zone between the unsteady reattachment line (Eaton and Johnston, 1982). This complex integration can be categorized in three regimes, depending on whether the flow is laminar or turbulent at separation and reattachment points (Kim et al. 1980 ; Nie and Armaly, 2004): (1) laminar-laminar, where the boundary layer is laminar at both separation and reattachment; (2) laminar-turbulent, where boundary layer is laminar at separation and turbulent at reattachment. Here, instabilities appear in the shear layer near the separation point and the shear layer becomes turbulent before the reattachment; (3) turbulent-turbulent, where boundary layer is turbulent at both separation and reattachment points. Here, the shear layer becomes turbulent very soon after separation, and the reattachment point becomes independent of the Reynolds number. For a three-dimensional step, the shear layers also separate from the sides and front of the of the step, which can create more complex recirculation zones and vortical structures such as horseshoe vortex (Fig. 1-3(b)). Additionally, for a more complex geometry that includes a superstructure, there exist vortices shed from the superstructure. Such highly complex flow over the helicopter platform of the vessel creates a region , which contains large spatial and temporal velocity gradients, and is associated with high turbulence (Zan, 2002). This complex flow structure can exert substantial unsteady forces on the helicopter and its rotor operating from the ship, which can significantly influence the overall trajectory of the helicopter and affect the workload of the pilot (Lee and Horn, 2004; Lee and Horn, 2005). Additionally, considering the transient effects of the change of the incoming wind direction, the wake structure and wake-helicopter interaction can become even more complex. Thus, in order to minimize the risks involved in helicopter operations, a deep understanding of the airwake over the helicopter platform is crucial.

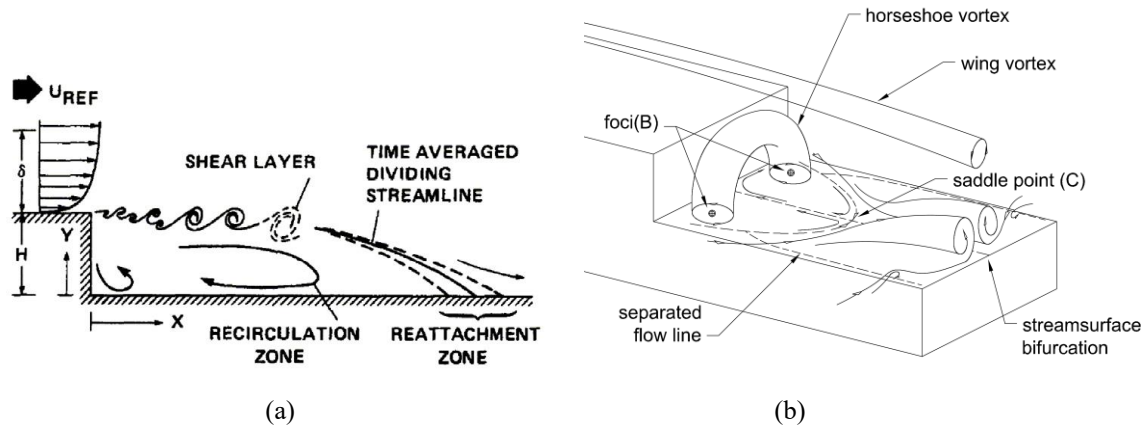


Fig. 1-3. (a) Two-dimensional (Bardera-Mora, 2014a) and (b) three-dimensional backward-facing step (Tinney and Ukeiley, 2009).

The rotary flow-control valve shown in Fig. 1-2 is composed of a ball valve with perforated plates inside the sphere trim, where the change in the opening of the valve, i.e. the incidence angle with respect to the oncoming flow, controls the flowrate. It was observed that such valve, which featured plates with high chord-to-thickness ratio and staggered perforation patterns, the flow-control system would undergo increased vibrations at the incidence angle of zero (Bossi, 2016). These vibrations are mainly due to the unsteady forces exerted on the perforated plates, which are the result of the interaction between the impinging flow and the bluff elongated plates (Bossi et al., 2017a). Similar to the classic problem of solid bluff rectangular plates (Kiya and Sasaki 1983; Cherry et al. 1984; Suksangpanomrung et al. 2000), this interaction can generate vortical structures in the wake and result in a highly complex flow field, which can involve the leading-edge boundary layer and flow separation and the consequent reattachment (Parker and Welsh, 1983; Stokes and Welsh, 1986; Nakamura et al., 1991), free shear layers (Roshko, 1955), vortex shedding (Bearman, 1997), bluff body wake (Mills et al., 2003) and the overall velocity deficit in downstream of the bluff body (Wynanski et al., 1986).

For a sufficiently large Reynolds number, the oncoming flow always separates from the sharp corner at the leading-edge and depending on the chord-to-thickness ratio reattaches to the side of the bluff plate (see section 1.1.3) and create a separation bubble with negative surface pressure coefficient (Cherry et al. 1984; Djilali and Gartshore, 1991; Suksangpanomrung et al. 2000). Similar to the backward-facing step configuration,

depending on the type of the boundary layer at the separation point, three regime of (Ota et al. 1981; Djilali and Gartshore, 1991): (1) laminar separation-laminar reattachment, where the reattachment length increases with the increase of Reynolds number; (2) laminar separation-turbulent reattachment, where the separated shear layer exhibits instability and becomes turbulent before reattaching to the plate; (3) turbulent separation-turbulent reattachment, where the reattachment length do not vary significantly for Reynolds number (based on the plate thickness) larger than  $2 \times 10^4$ . This unsteady structure is associated with a low frequency “flapping” of the separated shear layer, as well as large-scale pseudo-periodic vortex shedding from the separation bubble (Cherry et al. 1984). Downstream of this leading-edge separation bubble, for a plate with high thickness-to-chord ratio, the boundary layer develops along the plate and will inevitably separates from the sharp corner of the trailing edge, which will lead to development of recirculation zones in the near wake. Although many aspects of such phenomena for a solid plate with high chord-to-thickness ratio in zero incidence are previously studied, the issue of the effects of transverse perforations on the fluids-structure interaction and the resulting unsteady forces applied on the plate, and in turn on the valve as a whole, are not yet investigated. Therefore, it is necessary to investigate the wake structure of the perforated plates in zero incidence to provide insight into the origins of the loading on and vibrations of the valve. In specific, in this research, the near wake structure and the role of the trailing-edge vortex shedding in unsteady loading on the bluff plates were investigated.

Closely related to the benchmarked bluff configurations of backward-facing step and rectangular plate, the wake of the bluff bodies investigated in this research are largely the result of the separation of boundary layers at the sharp edges of the body, which in turn creates vortical structures in the vicinity of the separation point, e.g. over the helicopter platform of the CCG icebreaker and the near wake of the perforated plates. Furthermore, these configurations allowed the investigation of various aspects of the flow field and the generated wake, namely, the effects of the inflow conditions (spatially uniform, or a simulated boundary layer), the structural effects (absence or presence of structural vibrations), scale and geometry effects and the Reynolds number dependence. Although the results of this research contributes to the body of work on the external flow (e.g. ship

airwake) as well as internal flow (e.g. application of perforated plates in flow control systems), the measurement and analysis techniques are largely common. In this work, the wake of a scaled model of the icebreaker, associated with many sharp edges and separated boundary layers, as well as bluff perforated plates, associated with leading- and trailing-edge flow separations, were studied using flow measurement technique of two-dimensional particle image velocimetry. Both configurations resulted in highly three-dimensional wakes, which were investigated by considering several spatially varying data acquisition planes to capture such three-dimensionality. Additionally, the velocity field were analyzed in terms of the time-average flow data as well as turbulence metrics, e.g. root-mean-square of the velocity fluctuations.

### **1.1.2 Ship airwake**

The interaction between the impinging airflow, resulting from the ship motion and the atmospheric wind, and the ship's superstructure creates a highly disturbed region which contains vortical structures associated with temporal and spatial velocity gradients. This region is also known as ship airwake (Healey, 1987). The escalated level of turbulence in combination with spatial velocity gradients over the helicopter platform of the vessel is known to interfere with the pilot's ability to control the helicopter and increases the pilot's workload (Lee and Horn, 2004; Lee and Horn, 2005; Kääriä et al., 2012; Kääriä et al., 2013; Forrest et al., 2016). This scenario can be further complicated since the wind may change its direction unsteadily (Rahimpour and Oshkai, 2019). In order to minimize the risks associated with such complex phenomena and the resulting increased workload for the pilot a deep understanding of the airwake over the helicopter platform of a vessel, generated by airflow over the superstructure is crucial and necessitates systematic investigations of the effects of oncoming airflow and the ship motion. In addition, the yaw angle of the ship with respect to the oncoming airflow (Johns and Healey, 1989) and the unsteady change in the impinging wind direction (Rahimpour and Oshkai, 2019) are significant parameters. To this end, the ship airwake has been studied by field measurements, scaled model investigation and numerical simulations. As early examples of such studies, the effects of various yaw angles on the airwake were investigated experimentally by studying a 1:140 scaled model of the USN DD-963 Class Destroyer in

a boundary layer wind-tunnel using a smoke generator and the yaw angles associated with the highest turbulence over the center of the landing deck were qualitatively identified. The hot-wire anemometry was used by Rhoades (1991) to investigate the ship airwake on the 1:165 scaled model and the effect of the yaw angle on increased turbulence level over the landing deck was studied. Using a finite volume scheme, Tai and Carico (1995) discretized the Reynolds-averaged Navier-Stokes equations and studied the airwake of a USN DD-963 Class Destroyer in atmospheric winds of 10 and 30 kn at the wind angle of 30°. They compared the numerical results with those of wind tunnel studies and observed good agreement between numerical and experimental results for the time-averaged velocity components. Using hot-film anemometry, Zan et al. (1998) performed investigations on a scaled model of a Halifax-Class Patrol Frigate in 0° and 12° yaw angle in an atmospheric boundary layer wind tunnel. In addition, full-scale field measurements and computational fluid dynamics (CFD) were performed and the results showed agreement between the scaled-model tests and the full-scale measurements, but numerical results were associated with higher gradients in velocity fields, compared to the experimental data. Further investigations (Sezer-Uzol et al., 2005; Woodson and Ghee, 2005) showed that CFD and numerical simulations are capable of capturing the dominant flow characteristics, predict the flow separation locations and they showed a general agreement of the dominant shedding frequencies with observed experimental results. Thornber et al. (2010) in a more recent study employed implicit large eddy simulations (ILES) to investigate the airwake of two different Royal Navy vessels in an ABL at several incidence angles. They reported a good agreement between numerical results and those of wind tunnel experiments and full-scale measurements.

Due to the complex geometry of the vessels and their superstructure, the investigation of the airwake and its structure can become prohibitively expensive for numerical studies, therefore through the Technical Co-Operation Program (TTCP) (Wilkinson et al., 1998; Reddy et al., 2000), two generic 3D frigate models, Simple Frigate Shape (SFS1) and its successor SFS2, were chosen for numerical simulations, and wind tunnel experiments to provide benchmarking results. In their research, Reddy et al. (2000) performed a series of numerical simulations to analyze airwake of the simplified geometries using computational

code FLUENT. The simulations were performed using a structured grid and the  $k-\varepsilon$  turbulence modeling. They concluded that in a steady-state ship airwake, circulation zones and shed vortices dominate the flow field in the flight-deck region. They also recommended the use of RNG  $k-\varepsilon$  model and an unstructured grid to yield improved predictions of flow characteristics. Using CFD, Toffoletto et al. (2003) investigated the flow field over the flight deck of simplified geometries of SFS1 and SFS2 and the results were compared with those of water tunnel flow visualization experiments. The authors stated that time-averaged velocity fields over the flight deck were relatively similar and, comparison between numerical and experimental results showed numerical simulations could predict the general structure of the flow field. Large eddy simulation were used by Polsky (2003) to investigate the ship airwake in wind with  $90^\circ$  incidence angle for SFS1 geometry. The results of this numerical study were validated by wind tunnel time-averaged surface pressure measurements, which showed that the numerical results were very sensitive to the grid size and a coarse grid would result in considerably over-predicted separation region. More importantly, this study showed that, in contrast to a uniform inflow/outflow condition, application of an atmospheric boundary layer as an inflow/outflow boundary condition would greatly improve the results, in comparison with the field measurements. For the SFS1 and SFS2 geometry in incidence angles of  $0^\circ$ ,  $45^\circ$ ,  $90^\circ$  and  $330^\circ$ , Yesilel and Edis (2007) conducted a series of steady and unsteady numerical investigations. Several turbulence models were used for Reynolds-averaged Navier-Stokes equations and the obtained time-averaged velocity fields were validated by comparison with wind tunnel data. The lattice-Boltzmann method (LBM) was used by Syms (2008) to simulated the flow over SFS1 and SFS2 geometries in  $0^\circ$ ,  $45^\circ$  and showed that the lattice-Boltzmann algorithm could provide mean and unsteady flow field of a frigate-like shape accurately. As shown by Forrest and Owen (2010), using an atmospheric boundary layer (ABL) velocity profile as inflow condition would provide a better agreement between numerical results and those of wind tunnel and full-scale field measurements. They performed detached eddy simulations (DES) to study the airwake of SFS2 geometry as well as a Royal Navy vessel with detailed geometry, at several incidence angles. Although the results for the simplified and detailed geometries varied, it was shown that ABL as the inflow condition would improve the numerical results significantly in comparison with

those of experiments and field measurements. The SFS1 geometry was further studied by Bardera-Mora (2014a) who conducted wind tunnel measurements on a model with SFS1 geometry. Using PIV and laser doppler anemometry (LDA), velocity fields were obtained and used to calculate the time-averaged velocity components and the turbulence intensity over the helicopter platform for several angles of incidence between  $0^\circ$  to  $180^\circ$ . The incidence angles associated with the highest turbulence levels were identified and it was shown that despite the discrepancy between results for small incidence angles, the SFS1 role o geometry was capable of predicting the airflow over the helicopter platform. Building on the earlier studies, further modifications were applied to the Simple Frigate Shape and the effects of hangar roof curvatures on the near airwake of a modified SFS were investigated by Bardera-Mora and Meseguer (2014). The authors obtained the instantaneous velocity fields using PIV and evaluated the Reynolds stresses. They showed that by rounding the hangar roof the effects of the separated shear layer on the operation of helicopters could be reduced. In a more recent work, Forrest et al. (2016) performed numerical analysis utilized a SST  $k-\omega$  detached eddy simulation (DES) scheme to account for turbulence and investigated the effects of geometric modifications of vertical hangar edge.

As recent examples of full-scale field measurements, the in-situ measurements in the near-wake of a naval vessel by Snyder et al. (2011) and Brownell et al. (2012). By obtaining the velocity components at various locations on the flight deck using ultrasonic anemometers, the mean flow, Reynolds stresses and turbulent intensity were calculated, which could be used for validation of numerical simulations. Showing the importance of the ABL as an influential parameter on the flow field over the helicopter platform, Bardera-Mora (2014b) compared the field measurements of velocity components on the flight deck of a frigate with wind tunnel measurements, where the wind tunnel results were obtained in a uniform inflow condition whereas the in-situ measurements were captured in a oceanic boundary layer. As a result, a relatively high discrepancy between field data and wind tunnel results was observed.

While the previous investigations significantly contributed to the understanding of the fluid mechanics of ship airwake, several issues remain unresolved. In particular, to the

best of author's knowledge, none of the prior studies considered the effects of transient changes of the inflow direction on the wake of the superstructure. The transient changes in the inflow can occur both naturally and due to maneuvering of the vessel. While the vessel operation can be controlled, natural wind fluctuations in the azimuthal direction can interfere with helicopter operation.

The present experimental investigation was performed on a 1:522 scaled model of a Canadian Coast Guard polar icebreaker, which is positioned on a computer-controlled turntable. Although the ship-helicopter interaction and the operation of the helicopter from the flight deck will inevitably alter the ship airwake over the helicopter platform, a deep understanding of the wake structure in the absence of the helicopter is still crucial for the design of offshore helicopter platforms (CAP437, 2008). The experiments are conducted in a water channel, which featured apparatuses to create a simulated ABL. The flow field and wake of the vessel are studied using PIV in several vertical and horizontal data acquisition planes to capture the 3D effects of the flow field. As the first step, the effects of the oncoming flow is evaluated and two types of inflow conditions are compared: a uniform flow and a simulated atmospheric boundary layer (ABL). Then, the effects of the transient changes of the inflow direction is investigated. By rotating the scaled model of the ship with respect to the oncoming flow, the transient effects of the change in the wind direction is captured and both the rate of rotation and the direction of rotation as well as the resulting wake are analyzed.

### **1.1.3 Wake of perforated plates**

Many engineering systems involve fluid flow impinging on bluff bodies with sharp edges, e.g. rectangular plates. As an example, single plates or arrays of plates can be used to condition the flow, change the flowrate or alter the flow field downstream of the plate(s). Such flow-structure interaction in turn exerts forces and moments on the plate as well as the system as a whole, creates flow-induced vibrations and alters the flow past the plates. Developing a framework for understanding the sources of the flow-induced excitation and providing insight into the physics of such flow-structure interaction, a number of studies were focused on investigation of rectangular elongated plates at zero incidence with respect

to the incoming flow. As an earlier work, Parker (1966) performed a series of experiments in a low speed wind tunnel and studied single plate as well as cascade of flat plates parallel to the impinging flow, with different material properties (brass and light alloy) and thickness, resulting in different natural vibrational frequencies. In addition, a range of inflow velocities were considered. It was shown that the main frequencies associated with the flow (obtained by using microphone probes upstream and downstream of the plate(s)) would increase with the increase of impinging velocity in a relatively linear manner. The slope of such line (frequency vs the impinging velocity) was nearly constant for each plate, and the ratio of frequency/velocity could be non-dimensionalized using a characteristic length (here, the plate thickness) to obtain a constant value for each plate. This dimensionless number is known as Strouhal number (Naudascher and Rockwell, 1994). Okajima (1982) conducted a series of tests in a wind tunnel as well as a water tank and experimentally studied the vortex-shedding frequencies of various rectangular cylinders. Using hot-wire probes in the wake of the plate, the peak frequencies of shed vortices were obtained for the rectangular cylinders with the cord-to-thickness ratio between 1 to 4. Additionally, the inflow velocity of the wind tunnel and the water tank was controlled so that the Reynolds number varied between  $70 \leq Re \leq 2 \times 10^4$  ( $Re = U.t/\nu$ , where  $U$ ,  $t$  and  $\nu$  are the inflow velocity, thickness of the rectangular cylinders and the kinematic viscosity of the working fluid respectively). This study showed that for the cord-to-thickness ratios of 2 and 3, there existed critical Reynolds numbers associated with an abrupt change in the flow patterns and the wake of the cylinders as well as the vortex-shedding frequencies. The author attributed this change to the reattachment of the separated flow from the leading edge to the side of the cylinders: below the critical Reynolds number, the separated shear layer would always reattach to the side of the plate, but at the critical Reynolds number, the flow would only periodically reattach to the side of the cylinders. Using hot-wire measurements in the wake of flat plates, with squared or semicircular leading edge, positioned in an open-jet wind tunnel, Parker and Welsh (1983) studied the vortex shedding frequencies and flow patterns of the separated shear layers and investigated the effects of the chord-to-thickness ratio ( $c/t$ , varied between 0.055 to 52) as well as Reynolds number ( $1.48 \times 10^4 \leq Re \leq 3.11 \times 10^4$ ). Using smoke flow visualization technique, they studied the separation bubble and the possibility of the reattachment of the separated shear layers from

the leading edge of the plate. Moreover, the spectra of the non-dimensionalized frequencies of the vortex shedding in the wake of the plates were investigated with and without the presence of an excitation source, i.e. applied sound at specific frequencies. Their results showed that the applied sound would change the size and the location of leading-edge recirculation zone and the reattachment length. More importantly, they characterized the flow in the near wake of the plates based on the chord-to-thickness ratio and observed four flow regimes: For smaller chord-to-thickness ratio ( $c/t < 3.2$ ), the separated shear layer from the leading edge did not reattach to the plate. The increase in the chord-to-thickness ratio ( $3.2 < c/t < 7.6$ ) was associated with the leading-edge shear layer reattaching periodically to the plate. For  $7.6 < c/t < 16$ , the shear layer would always reattach to the side of the plate upstream of the trailing edge and form a recirculation zone, which would fluctuate in length. As the chord-to-thickness ratio increased further ( $16 < c/t < 52$ ), the separated shear layer from the leading edge would always reattach, but the location of the reattachment point was well upstream of the trailing edge of the plate. Such wake structure would influence the spectra of the data obtained by the hot-wire measurements in the wake, and in turn would alter the observed spectral peak frequencies of the vortex shedding. The unsteady flow structure and the vortex shedding associated with the elongated rectangular cylinders with chord-to-thickness ratios of  $3.0 \leq c/t \leq 16$  were further studied experimentally and numerically by Nakamura et al. (1991) and Nakamura et al. (1996) in the range of  $200 \leq Re \leq 3 \times 10^4$ . They verified the existence of the regimes observed by Parker and Welsh (1983). Moreover, they showed that the increase of chord-to-thickness ratio would cause an abrupt transition in the Strouhal number based on the peak spectral frequencies of vortex shedding, which showed a stepwise increase by the increase of the chord-to-thickness ratio. In addition, such transition in the flow pattern and the associated Strouhal number was independent of the Reynolds number for the considered range. Furthermore, other elongated bluff bodies were investigated, for example, Nakamura and Nakashima (1986) conducted a series of wind tunnel experiments on bluff prisms with elongated H and  $\perp$  shaped rectangular cross-sections and measured the frequencies of the vortex shedding from such bluff bodies using hot-wire measurements in their wake for various inflow velocities for the wind tunnel. They observed the variation of the non-dimensionalized peak frequencies in the power spectra with respect to various depth-to-

height ratio and the impinging flow velocity. Such studies, among others, have established that the flow structure around bluff rectangular plates can be classified based on the leading-edge flow separation and the possibility of reattachment of the separated shear layer to the side of the bluff body, as well as the location of the reattachment point relative to the trailing edge. Moreover, such studies provided valuable insight into the complex and unsteady wake associated with a stationary elongated bluff body at zero incidence and created a framework for understanding of such fluid-structure interactions in terms of the non-dimensionalized frequencies, i.e. Strouhal number,  $St = fL/U$ . Here  $f$  is the characteristic frequencies of the vortex shedding, the flow velocity, external excitation source, and/or structure oscillations/vibrations (often the peak spectral frequencies),  $L$  is the characteristic length (often chord or thickness of the bluff body), and  $U$  is the characteristic flow velocity (often the velocity of the impinging flow). The fluid flow impinging on elongated cylinder and rectangular plates continued to be a subject of many studies. Guillaume and LaRue (2001), using hot-wire sensors located in the near wake region, compared the vortex shedding of a single flat plate with those of an array of similar plates. In their experiments for a single plate, it was shown that  $c/t \approx 6$  and 11 were associated with an abrupt jump in Strouhal number, where the Strouhal number was calculated based on the peak frequencies in the velocity spectra, and the chord of the plate. They also observed that, unlike the case of a single plate, an array of six similar plates exhibited a rather linear increase in the Strouhal number with the increase of chord-to-thickness ratio. Additionally, they observed that the Strouhal number based on the thickness of the plate would only show an abrupt jump in  $c/t \approx 4$  and it remained relatively constant for  $c/t > 4$ . Guillaume and LaRue (2005) later compared the flow field on bounded and unbounded side of a plate in a two-plate configuration using smoke visualization technique. Observing the flow patterns and the reattachment points on the bounded and unbounded side of a plate, they found that the recirculation zone on the bounded side would be smaller and the flow reattachment would occur at shorter distance from the leading edge of the plate, due to the acceleration of the flow between the plates. They attributed the lack abrupt change in the Strouhal number observed for an array of plate to such accelerated flow and the resulting favorable pressure gradient. Malavasi and Guadagnini (2007) studied the effects of wall confinement as well as the interactions between a rectangular

cylinder and free surface in a series of experiments conducted in a water channel, where the asymmetry of the flow on different sides of the cylinder was controlled by changing the water level as well as the vertical location of the cylinder. They measured the exerted forces by the impinging flow using two dynameters attached to the sides of the rectangular cylinders and investigated lift and drag forces as well as the Strouhal number based on the peak frequencies of the spectra of the measured forces. Later Malavasi and Zappa (2009) studied the fluid dynamic loading of a rectangular plate at different angles of attack and investigated the effects of the wall confinement on one side of the plate in a wind tunnel, by means of direct force measurement. The obtained force signal were then used to calculate force coefficients as well as the peak frequencies of the force signal, which were non-dimensionalized in the form of a Strouhal number. Negri et al. (2011) performed PIV to investigate the flow field and the near wake of a plate located in a free-surface water channel. More importantly, they obtained the frequencies of the vortex shedding and compared the resulting Strouhal numbers with those of Malavasi and Guadagnini (2007), which showed good agreement between the Strouhal numbers based on the vortex shedding frequencies and those of direct lift measurements. Elasticity of the plate has also been investigated in previous works, as an example, Jaworski and Peake (2013) theoretically studied the effects of elasticity and porosity of a semi-infinite plate interacting with a turbulent eddy on radiated acoustic noise using the Weiner–Hopf technique. Moreover, Clark et al. (2014) conducted the related experimental measurements of the fluctuating pressure due to flow over a porous surface with flexible bristles. In addition to the work of Parker (1966) and Parker and Welsh (1983), flow-acoustic resonance and the coupling of the flow oscillations with acoustic pressure pulsations received significant attention over the years. As examples of such work, Bossi and Malavasi (2014) investigated a rotary control valve with perforated plates utilized for flowrate control and studied the acoustical response of the valve. Oshkai and Velikorodny (2013) experimentally studied the coupling between the separated shear layers from a splinter plate, located in a duct at the location of two symmetric side branches, with the standing acoustic waves inside the duct and side branches. In their work, they used a combination of PIV and the measurements of the acoustic pressure using pressure transducers located at the end of the side branches.

While many aspects of the fluid flow interacting with a bluff rectangular plate in zero incidence have been studied before, the present work focuses on some of unanswered questions. In this work, PIV as well as the direct force measurements are used to identify the effects of the transverse perforations on the near wake of bluff elongated flat plates as well as the resulted unsteady loading exerted on the plate and its frequencies. Moreover, the role of perforations and their local effects on the formed boundary layer and magnitude of velocity fluctuations in the wake are investigated. In addition, the present research provides insight into the origin of the flow-induced loading on perforated plates.

## **1.2 Methodology**

This section summarizes the experimental apparatuses and the data acquisition techniques and systems used in the present research. The information presented in this chapter is partly repeated in the subsequent chapters 2, 3 and 4, which are corresponding to the published articles based on this work.

### **1.2.1 Flow facility**

The present experimental study was conducted in a flow visualization water channel located at the Fluids Dynamics Research Laboratory at the Department of Mechanical Engineering of University of Victoria (Fig. 1-4). The water channel is of a re-circulating design, where the flow is driven using a pump powered by a 25 HP motor. This configuration allows a variable flow velocity, using the controllers for the driving motor. The water channel featured a test section with a length of 2.5 m, where the water level can be adjusted to the maximum water level of 45 cm. The test section can also be confined using costume-built lids placed on top of the flow-visualization test section. The test section, in the confined configuration has a square cross-section of 45 cm  $\times$  45 cm. The flow is conditioned upstream of the visualization section using several fine meshes as well as a honeycomb section. Moreover, the water channel featured a converging section immediately upstream of the test section. Such configuration resulted in a uniform velocity at the inlet of the test section.



Fig. 1-4. The water channel at the Fluids Dynamics Research Laboratory at the Department of Mechanical Engineering of University of Victoria.

## 1.2.2 Experimental apparatus

### 1.2.2.1 *Ship airwake*

The experiments were conducted using a 1:522 model of the Canadian Coast Guard icebreaker, which included aerodynamically-relevant features of the full-scale vessel. The schematics of the scaled model is shown in Fig. 1-5. The scale factor of 1:522 was chosen so that the blockage ratio of the scaled model with respect to the cross-sectional area of the water channel was less than 6% for all incidence angles. In this research, the maximum blockage ratio was 5.5%, which was associated with the incidence angle of  $90^\circ$ . The model was placed on a custom-built computer-controlled turntable, which allowed accurate control of the incidence angle with respect to the oncoming flow as well as the rate at which the scaled model could be rotated. The turntable, attached to a programmable motor, was placed on the top wall of the water channel through an access hatch (Fig. 1-6) so that the visualization section was confined. In this research, it is assumed that the vortical structures in the wake over the helicopter platform are mainly due to the ship forward motion and the interaction with the impinging wind, therefore, following recent scaled model experiments,

as reviewed by Shukla et al. (2019), only the effects of change in incidence angle of the vessel with respect to oncoming flow were studied, and the effects of the sea waves were neglected. Thus, other degrees of freedom, i.e. the heave, sway, roll and pitch motions were not considered. This assumption is in agreement with the numerical simulations of Dooley et al. (2020), which showed that only in very rough sea conditions, associated with large wave amplitudes, the ship airwake would deviate from that of calm sea.

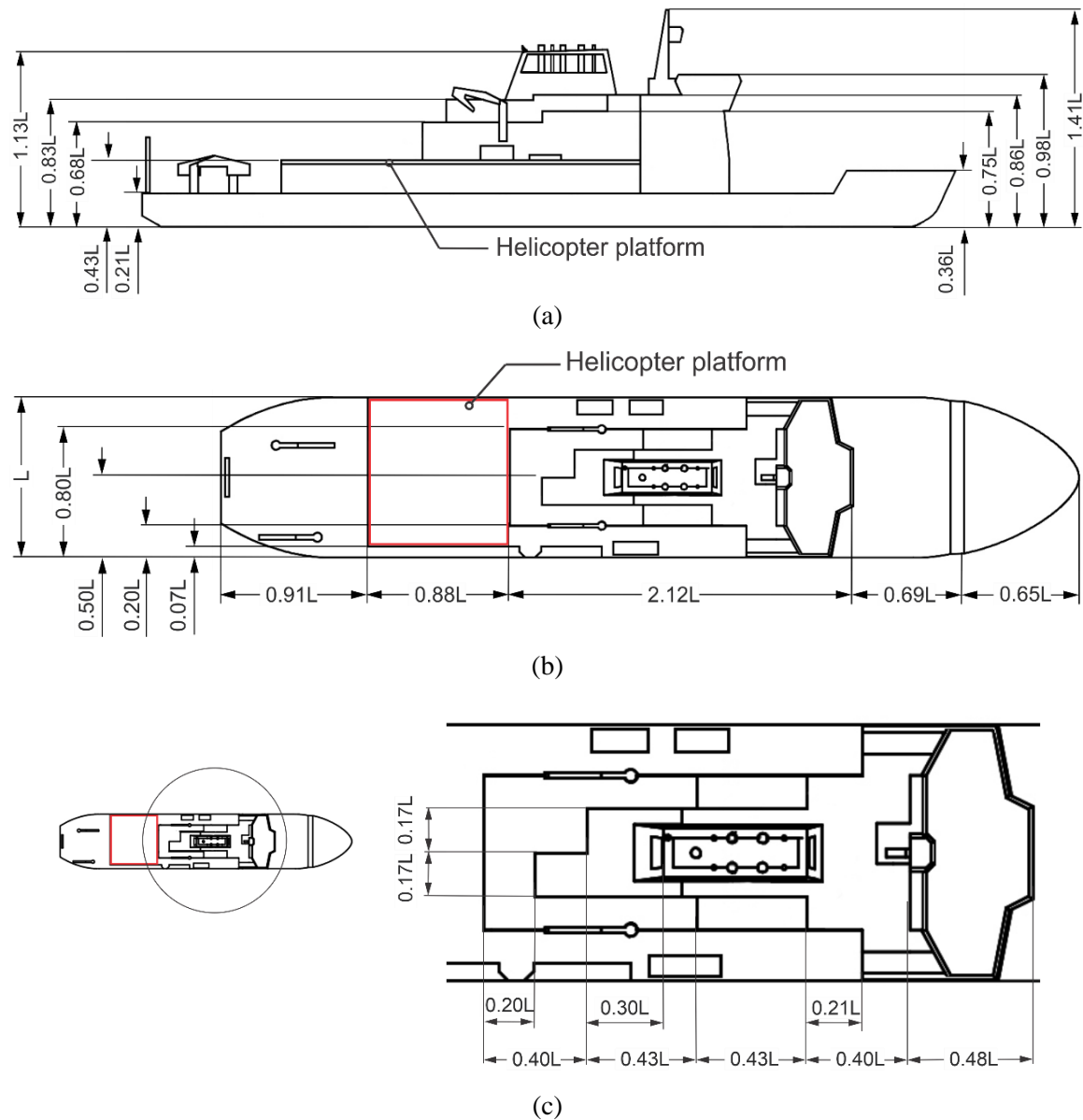


Fig. 1-5. The schematics of the scaled model of CCG icebreaker: (a) side view, (b) plan view (c) closeup of the superstructure.

In order to simulate the ABL in the water channel, an experimental configuration of the type developed by Irwin (1981) was used. In this setup, three triangular spires with the height of  $h = 7/9 H$  were positioned at the entrance of the test section of water channel, where  $H$  is the maximum water level in the test section. In the immediate downstream of the spirals, over the length of  $l = 3.16 H$ , distributed surface roughness elements (cubes with the height  $b = 1/90 H$ ) were positioned. The width of the spires at the wall of the test section was equal to  $0.075 H$ , and the spacing between them was equal to  $0.16 H$ . The spacing between the roughness elements in the streamwise and the transverse directions was equal to  $0.035 H$  as shown in Fig. 1-6.

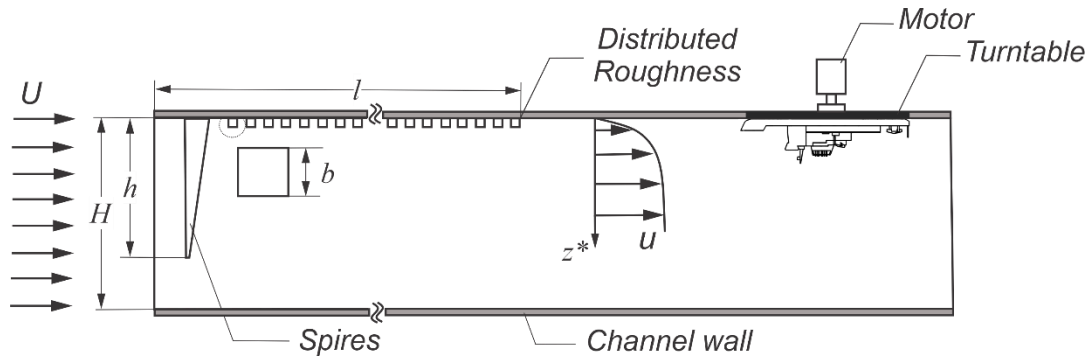


Fig. 1-6. Schematic of flow conditioning elements.

The desired boundary layer conditions were achieved 125 cm downstream of the entrance of the test section, at which, the distribution of the of streamwise velocity component and turbulence intensity for the simulated ABL were in good agreement with the power law profile associate with open sea conditions (Counihan, 1975; Zhou and Kareem, 2002):

$$\frac{u(z^*)}{u_\delta} = \left( \frac{z^*}{\delta} \right)^{0.13}, \quad (1-1)$$

$$\frac{I_u(z^*)}{I_{u,\delta}} = \left( \frac{z^*}{\delta} \right)^{0.13}. \quad (1-2)$$

Here  $z^*$  is the vertical position in the simulated ABL from the wall of the water channel and  $\delta$  is the thickness of the generated boundary layer (Fig. 1-6). In this research,

the location of the edge of generated boundary layer was used as the reference point in the power law profile (Eqs. 1-1, 1-2, 2-1, 3-1 and 3-2), as shown in Fig. 2-2 and Fig. 3-2, which is discussed further in section 2.2.1.

In addition to small blockage ratio, the scale factor of 1:522 resulted in a scaled model of CCG icebreaker that was positioned entirely inside the simulated ABL so that the height of the superstructure was approximately equal to 28% of the generated boundary layer. Considering the height of the full-scale CCG icebreaker, the simulated ABL corresponded to an atmospheric wind with gradient height of 200 m. The variation of air density with elevation corresponding to this height is less than 2%. Moreover, the decrease in air density with elevation corresponding to the height of CCG icebreaker in full scale is only 0.38% (Diehl, 1978). Therefore, the variation of fluid density across the simulated ABL was not replicated.

In this study, the Reynolds number was defined based on the velocity at the entrance of the water channel as the characteristic velocity and, following Healey (1992) and Greenwell and Barrett (2006), the beam of the scaled model as the characteristic length, which resulted in the Reynolds numbers of  $Re = 47900$ ,  $Re = 50500$  and  $Re = 61000$  for both uniform inflow and the simulated ABL. For both inflow conditions this range of Reynolds number is well above the minimum of 11000 recommended for wind tunnel testing of ships (Healey, 1992). For the CCG icebreaker in full scale, the wake over the helicopter platform is the result of the vessel's forward motion (here simulated by the uniform inflow) and the impinging atmospheric wind (here represented by the simulated ABL). At the design speed of 18 knots, the Reynolds number associated with the forward motion of the CCG icebreaker is approximately  $Re = 20 \times 10^6$ . Moreover, considering a typical wind velocity in open sea conditions (Eq. 1-1), the Reynolds number based on the wind velocity at the height of the superstructure in full scale is approximately  $Re = 25.8 \times 10^6$ . The effects of the Reynolds number on the wake structure and the fluid dynamic similarity between the scaled model and the full-scale icebreaker will be discussed in section 2.3.1.

### 1.2.2.2 Wake of perforated plates

For experiments conducted on the elongated plates, three plates with transverse perforations, as well as a reference plate with no perforations, were considered. Herein, the reference plate is referred to as P0. The three perforated plates had similar staggered pattern for perforations, but featured different perforation diameters of  $\delta_h = 9.4$  mm, 12.7 mm, 19.5 mm, herein, referred to as patterns P1, P2 and P3, respectively. The spacing between the perforations was also equal to  $\delta_h$ , therefore, all three plates had the same equivalent area ratio,  $\beta = (nA_p/A_t)^{0.5} = 0.4$ , where  $n$  is the number of perforations,  $A_p$  is the area of a single perforation,  $A_t$  is the total wetted area of the plate. The thickness of the plates P0, P1 and P2 was  $t = 12.5$  mm and P3 had a thickness of  $t = 12.3$  mm. The chord length for all plates were equal as  $c = 292.1$  mm. The geometry of the plates, including the equivalent area ratio, perforation pattern and the chord-to-thickness ratio ( $c/t \approx 23$ ), was chosen to match the perforated plates used in the rotary flow-control valve shown in Fig. 1-2. The plates were made of clear polycarbonate plastic sheet, with the material properties of: density  $\rho = 1245.6$  kg/m<sup>3</sup>, modulus of elasticity  $E = 2.6$  GPa and modulus of rigidity of  $G = 2.3$  GPa. The plates were positioned at the center of the flow-visualization section of the water channel, parallel to the oncoming flow. Moreover, the plates were cantilevered at the top edge and attached to the frame of the water channel by a support structure that incorporated a load cell for direct force measurements (Fig. 1-7 and Fig. 1-8). In order to minimize the effects of the flow separation from the free edge of the plates, the plate was located 2.5 mm away from the bottom of the test section of the water channel. As shown in Fig. 1-8, the depth of the water in the test section was equal for all cases,  $W = 41.5$  cm, so that the free-surface level coincided with the edge of the clamp. Furthermore, Fig. 1-8 shows the vertical location of the PIV laser light sheet, i.e. the PIV data acquisition plane,  $e_l$ , which will be discussed in section 4.2.4. The damped natural vibrational frequency ( $f_0$ ) of the plates was measured by conducting damping tests in still water (zero inflow velocity at the entrance of the water channel), where a force, creating nonvisible deflection, was applied to the plates and then removed. The free decay torque signal was recorded and then analyzed by applying Fourier transform to the signal to obtain the damped natural vibrational frequency. The test in still water was repeated for several impact points of the applied force, which

showed relatively similar results. The obtained natural frequencies were averaged for individual plates, which yielded the damped natural frequencies of  $f_0 = 5.1$  Hz and  $f_0 = 7.8$  Hz for the solid and the perforated plates, respectively.

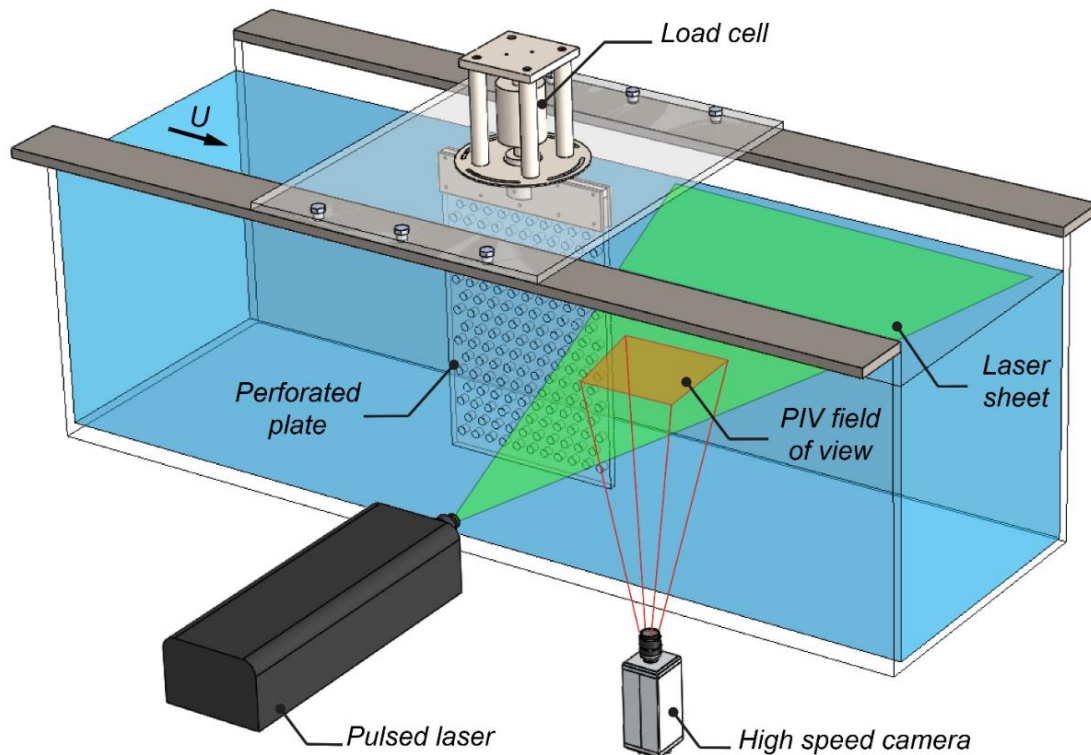


Fig. 1-7. Schematic of the experimental system, including main components of the PIV system.

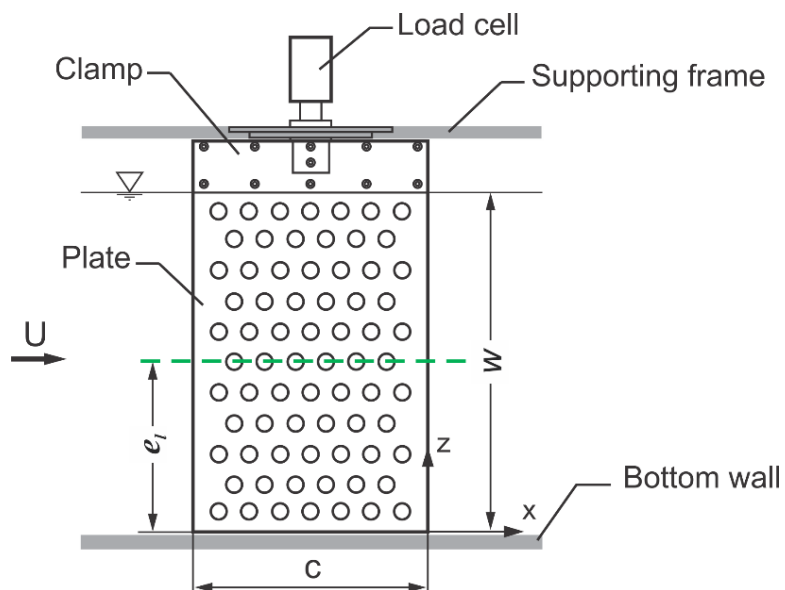


Fig. 1-8. Schematic of the perforated plate.

### 1.2.3 Measurement techniques

#### 1.2.3.1 Flow field measurements

Global, instantaneous velocity measurements were obtained using high-speed particle image velocimetry (PIV). Implementation of PIV involved seeding the flow with tracer particles that were illuminated by a pulsed laser and photographed using a high-resolution digital camera. In this investigation, the PIV system consisted of (i) a 25 mJ Nd:YLF dual diode-pumped laser (Darvin-Duo series by Quatronic) used to produce a planar laser light sheet, (ii) a  $1024 \times 1024$  pixels CMOS camera and (iii) a PC equipped with hardware for PIV image acquisition and software (LaVision DaVis versions 7.2 and 8.0) for image processing.

The instantaneous velocity fields were calculated by cross-correlating the patterns of tracer particles in interrogation windows in consecutive images, by applying the discrete fast Fourier transform (FFT) to the image intensity field for two interrogation windows in consecutive images, followed by a complex-conjugate multiplication of the resulting Fourier coefficients. The cross-correlation function (in spatial domain) was then computed by taking inverse Fourier transform of the product. For each interrogation window, the location of the dominant peak of the cross-correlation function indicated the average particle displacement vector, and based on the frequency of PIV image acquisition, the instantaneous velocity components were calculated (Raffel et al., 2007). The details of the implementation of the PIV for investigation of the wake of the scaled model of the Canadian Coast Guard icebreaker as well as that of the elongated plate are discussed in chapters 2, 3 and 4, which includes the details of the used optical lenses, size of interrogation windows and spatial and temporal resolution of the obtained dataset.

The obtained instantaneous velocity at each data point then is used to calculate the time-averaged velocity field ( $u$ ,  $v$ ,  $w$ ), the root-mean-square (r.m.s) of the velocity fluctuations and Reynolds stresses:

$$\langle u, v, w \rangle = \frac{1}{N} \sum_{i=1}^N [u_i(x, y, z), v_i(x, y, z), w_i(x, y, z)] \quad (1-3)$$

$$\begin{aligned}
u_{rms} &= \sqrt{\frac{1}{N-1} \sum_{i=1}^N [u_i(x, y) - \langle u_i(x, y) \rangle]^2}, \\
v_{rms} &= \sqrt{\frac{1}{N-1} \sum_{i=1}^N [v_i(x, y) - \langle v_i(x, y) \rangle]^2}, \\
w_{rms} &= \sqrt{\frac{1}{N-1} \sum_{i=1}^N [w_i(x, y) - \langle w_i(x, y) \rangle]^2}
\end{aligned} \tag{1-4}$$

$$\begin{aligned}
R_{uu} &= \langle u' u' \rangle, R_{vv} = \langle v' v' \rangle, R_{ww} = \langle w' w' \rangle, \\
R_{uv} &= -\langle u' v' \rangle, R_{uw} = -\langle u' w' \rangle, R_{vw} = -\langle v' w' \rangle
\end{aligned} \tag{1-5}$$

Here,  $N$  is the total number of PIV image pairs and  $u' = u - \langle u \rangle$ ,  $v' = v - \langle v \rangle$  and  $w' = w - \langle w \rangle$  are the instantaneous velocity components.

### 1.2.3.2 Unsteady force measurements

A three-axis load cell, Novatech F233-Z3712, was used for the direct force and torque measurements, which was connected to LabView software through the 16-bit resolution Digital Acquisition system (DAQ). The load cell was capable of capturing the streamwise (drag) and lateral (lift) force components as well as torque around the vertical axis. Three Novatech SGA/A amplifiers were also connected to each channels of the load cell. The force and torque signals were filtered using a low pass filter to avoid aliasing and to reduce noise. The maximum measurable force in srteamwise and lateral directions were 80 N, and the maximum measurable torque around the vertical axis was 4 Nm. The uncertainty of the load-cell is estimated at  $\pm 0.7\%$  of the rated value for the three channels.

In the present work, the calibration centre of the load cell was such that it corresponded to the centre of gravity of the plates. The obtained force and torque signals in time were analyzed by applying Fourier transform to the signals. Additionally, the time-averaged values of streamwise (drag) force component and the root-mean-square if the lateral (lift) force component were obtained.

### 1.3 Research Contributions

The present research contributes to the areas of maritime aerodynamics, bluff body fluids dynamics, and fluid-structure interaction. This work first focused on the aerodynamics of a Canadian Coast Guard icebreaker and investigated the effects of the inflow conditions. This work further expanded to identify the effects of the transient change in the wind direction. Then, the interaction of the impinging fluid flow and high aspect ratio rectangular plates with transverse perforations was studied. In summary, the main contributions of this work are as follows:

- 1- **Quantifying the effects of the inflow conditions on the wake of the ship superstructure:** The airwake and the associated escalated turbulence level were investigated experimentally, using PIV. As the main objective, the influence of the inflow conditions were studied. In the present research, two types of inflow conditions were considered: a uniform inflow and a simulated ABL. The velocity fields associated with different inflow conditions were obtained for a range of incidence angles, which were then used to obtain the turbulence level and identify the incidence angles with highest turbulence. It was observed that the simulated atmospheric boundary layer promoted the development of higher turbulent velocity fluctuations over the helicopter platform, specifically for the incidence angles associated with larger-scale flow separation from the superstructure of the vessel. It is worth mentioning that the dependence of the experimental results on the Reynolds number was studied and it was observed that, in accordance with previous studies, for relatively high Reynolds numbers ( $\sim 1.0 \times 10^4$ ), the wake structure is relatively independent of the Reynolds number, which can be attributed to the separation of boundary layer from the bluff scaled model.
- 2- **Quantifying the effects of the unsteady changes in the wind direction on the wake of the ship superstructure:** Building on the results obtained for a stationary vessel in the atmospheric wind, which was associated with higher turbulence, this work aimed to quantify the effects of the unsteady change in the direction of the impinging wind. In order to capture the three-dimensionality of

the flow, several vertical and horizontal data acquisition planes were considered. In order to simulate the changes in the direction of the impinging wind, a novel approach was considered, which involved positioning the scaled model on a computer-controlled turntable. The changes in wind direction were simulated by rotating the scaled model at a certain rate. Generally, the increase of the rate of change of the inflow direction resulted in an increase of the turbulent intensity. However, as the flow over the helicopter landing platform was dominated by the wake of the asymmetric superstructure, the effect depended on the nominal direction of the inflow. In particular, when the inflow was coming from  $\alpha = 60^\circ$ , clockwise rotation of the ship model with respect to the inflow exposed the helicopter platform to increased turbulent velocity fluctuations, while counterclockwise rotation diminished the flow unsteadiness over the helicopter platform.

- 3- **Quantifying the effects of the transverse perforations and the Reynolds number on wake structure of and the resulted unsteady loading on high aspect ratio rectangular plates:** In an effort to identify the origins of the unsteady loadings on and the resulting flow-induced vibrations of the perforated plates at zero incidence, the direct force measurement as well as PIV were used. It was observed that the vortex shedding frequencies were in very good agreement with those of the measured flow-induced forces for all considered perforation patterns. Therefore, it was determined that the trailing-edge vortex shedding was the main mechanism of generating the unsteady loading on the plates. For small perforations, the velocity fluctuations in the near wake were enhanced. However, further increase of the perforation diameter led to suppression of the velocity fluctuations. The staggered patterns of the perforations created a three-dimensional boundary layer, whose thickness increased with the decrease of the distance of the most downstream perforation from the trailing edge of the plate. Moreover, the proximity of the perforations to the trailing edge highly influenced the three-dimensional structure of the near wake: In the cross-sectional planes corresponding to the close proximity of the perforations to the downstream edge,

periodic trailing-edge vortex shedding were suppressed. Moreover, the largest considered perforation diameter resulted in the resonance between trailing-edge vortex shedding and transverse oscillations, where these frequencies remained locked on the natural vibrational frequency of the plate.

It is noteworthy that the main contributions of this dissertation are presented in three journal articles (Rahimpour and Oshkai, 2016; Rahimpour et al., 2018; Rahimpour and Oshkai, 2019).

#### **1.4 Dissertation Outline**

This dissertation is organized in five chapters. After discussing the motivation of the present research, reviewing the previous relevant work as well as discussing the methodology and the main contributions in Chapter 1, the remaining chapters are as follows:

In Chapter 2, the experimental investigation of the wake of a polar icebreaker, as a bluff body characterized by sharp edges, is presented. Scaled model experiments were performed in a water channel and PIV were used to study the separated flow and the consequent highly disturbed region over helicopter platform of the vessel. In order to compare the effects of the oncoming flow, two type of inflow conditions for the water channel were considered: (i) uniform and (ii) a simulated atmospheric boundary layer. The main objective of this chapter is to identify the incidence angles of the impinging wind associated with high turbulence as well the effects of the inflow conditions.

Chapter 3 aims to build on the results of Chapter 2 by investigating the effects of unsteady change in the wind direction, using a programmable and computer-controlled turntable, which housed the scaled model of the vessel. In this chapter the flow over the helicopter platform was studied to identify both the rate of change in the wind direction as well as the incidence angles associated with the highest turbulence over the helicopter platform.

In Chapter 4, the results of a series of experiments on bluff elongated flat plates are discussed. Using direct force measurement as well as PIV, the effects of the transverse perforations on the unsteady loading on the bluff body as well as the generated wake were investigated. In specific, the role of the trailing-edge vortex shedding, the origins of the unsteady loading on the plate and the velocity fluctuations in the wake and its structure were studied.

In conclusion, in Chapter 5, a summary of contributions and the conclusions from previous chapters, along with recommendations for future research, are provided.

## 2 Experimental Investigation of Airflow over the Helicopter Platform of a Polar Icebreaker

### Preamble

The body of this chapter has been published as: Mostafa Rahimpour, Peter Oshkai, 2016. Experimental investigation of airflow over the helicopter platform of a polar icebreaker, *Ocean Engineering*, 121, 98-111.

DOI: 10.1016/j.oceaneng.2016.05.023.

Explicit permission to reprint the material, as detailed above, in the present dissertation is granted by Elsevier, as the publisher of *Ocean Engineering*.

Contributions: M. Rahimpour designed the study and experimental system, conducted the measurements, collected and post processed the data, performed the analysis and prepared the initial manuscript. P. Oshkai supervised the research, provided insight and contributed to the development of manuscript drafts.

## Abstract

The airwake over the helicopter platform of a Canadian Coast Guard (CCG) polar icebreaker was studied experimentally. By application of high-speed particle image velocimetry (PIV) on a 1:522 scaled model of the polar icebreaker, quantitative flow field data were obtained in several vertical and horizontal planes. The investigation compared the effects of two types of inflow conditions: (i) a uniform flow and (ii) a simulated atmospheric boundary layer (ABL) on the flow structure over the helicopter platform of the ship. The incidence angle ( $\alpha$ ) between the oncoming flow and the orientation of the ship varied between  $0^\circ$  to  $330^\circ$  with the increment of  $30^\circ$ . The unsteadiness of the flow and the turbulent fluctuations were quantified by calculating the components of the Reynolds stress tensor and the turbulence intensity. Higher maximum values of the turbulence intensity were observed in the case of the simulated ABL. For both inflow conditions, the incidence angle of  $300^\circ$  corresponded to the highest turbulence levels over the helicopter platform.

**Keywords:** Ship airwake; Atmospheric boundary layer; Particle image velocimetry, Turbulence metrics.

## 2.1 Introduction

A combination of ship motion and prevailing wind, interacting with vessel's superstructure, creates a region of highly disturbed flow, which is referred to as ship airwake. The airwake is produced as a result of bluff body separation. It contains unsteady turbulent flow structures and is characterized by large spatial and temporal velocity gradients. Such significant increase in the turbulence levels, as well as the escalated temporal and spatial gradients of wind velocities, compared to the undisturbed flow conditions, are known to interfere with maneuverability of helicopters, which can result in loss of control during operation from ship-based platforms (Healey, 1987 ). In compensating for the large-scale disturbances that are present in this complex and unsteady flow, the pilot may be forced to fly the aircraft dangerously close to the superstructure or the helideck, or unexpected gusts

may carry the helicopter away from the vessel (Johns and Healey, 1989). Due to significant challenges for the pilots during the launch and the landing, an in-depth understanding of the ship airwakes, particularly in the vicinity of the helicopter platform, is crucial to minimize the risks involved in helicopter operation.

In analysis of complex flow phenomena, such as 3D boundary layer separation and wake, experimental investigations are the main approach for providing an insight into the flow physics. The full-scale field measurements are often not suitable for a comprehensive study due to the lack of repeatable flow conditions. Additionally, in the full-scale field tests, in order to sample a highly non-uniform flow field, only few strategically placed anemometers can be used, which results in low spatial resolution. In contrast, investigations on scaled models provide repeatable flow condition and yield results with significantly higher spatial resolution. In an early study, in 1987, the prospects for investigation of helicopter/ship interface were discussed by Healey (Healey, 1987). The author commented that a ship airwake was highly complex, and its dynamics was virtually unknown at the time. He identified the oncoming airflow and the ship motion as the important parameters in investigation of this phenomenon.

Another important parameter that determines the structure of the ship airwake is the yaw angle of the ship with respect to the oncoming airflow. Johns and Healey (1989) performed a flow-visualization study on the 1:140 scaled model of the USN DD-963 Class Destroyer in a boundary layer wind-tunnel using a smoke generator. Through this study, the effects of yaw angles of  $30^\circ$ ,  $15^\circ$ ,  $0^\circ$ ,  $330^\circ$  and  $345^\circ$  on the airwake were investigated. It was observed that, in general, the level of turbulence on the flight deck was higher when the relative wind was on the starboard side. In addition, it was shown that the yaw angle of  $330^\circ$  corresponded with the highest turbulence over the center portion. Rhoades (1991) investigated the ship airwake using hot-wire anemometry on the 1:165 scaled model of another vessel. The authors indicated that the turbulence levels and the size of the recirculation zones over the deck of that ship increased as the ship was yawed. The maximum turbulence level was found to correspond to the  $50^\circ$  incidence angle, which began to decrease until it was relatively small in  $110^\circ$ . Tai and Carico (1995) performed numerical simulation of the airwake of a USN DD-963 Class Destroyer in atmospheric

winds of 10 and 30 kn at the wind angle of 30°. In this study, a finite volume algorithm was used to for discretization of Reynolds-averaged Navier-Stokes equations. Moreover, the Baldwin-Lomax model with the Degani-Schiff modification was employed for turbulence modelling. As the main feature of the flow, regions of massive flow separation were observed. There was also a good agreement between numerical results for time-averaged velocity components with those of wind tunnel studies. In order to analyze the airwake behind the superstructure of the Halifax-Class Patrol Frigate, Zan et al. (1998) performed investigations on a 1:50 scaled model of the vessel in an atmospheric boundary layer wind tunnel. By application of hot-film anemometers, the flow field in the vicinity of flight deck was studied at 0° and 12° yaw angle with respect to the oncoming airflow. This investigation was complemented with numerical simulations as well as full-scale field measurements using vane-type anemometers. The authors employed CFD-ACE, a commercially available computational fluid dynamics (CFD) flow solver, for numerical simulation. Comparison between the scaled-model tests and the full-scale measurements revealed a good agreement between the results obtained by both methods. There was a qualitative agreement between the experimental results and the results of the numerical simulation, where both predicted the same flow topology. The CFD simulations produced higher gradients in velocity fields, compared to the experimental data. The details of this numerical work and the comparison with the experimental results are reported by Syms (2004).

Through the Technical Co-Operation Program (TTCP) (Wilkinson et al., 1998; Reddy et al., 2000), two generic 3D frigate models, Simple Frigate Shape (SFS1) and its successor SFS2, were chosen for wind tunnel experiments and numerical simulations to produce results representative of vessels of the same class. As example of these studies, Toffoletto et al. (2003) used computational fluid dynamics to compare the flow over the flight-deck region for SFS1 and SFS2. The RNG  $k-\varepsilon$  turbulence modelling scheme was used and the results were compared with water tunnel flow visualization data. It was shown that for the case of SFS2 velocity varied more frequently, but magnitude of velocity variations were relatively smaller compared with results for SFS1. Furthermore, the results revealed that the time-averaged velocity fields over the flight-deck region were not

significantly different. Moreover, comparison with the water channel visualization data showed that the numerical simulation could in fact predict the general structure of the flow field. Polsky (2003) investigated the ship airwake in beam winds using a monotone integrated large eddy simulation (MILES). This numerical study was validated using the time-averaged surface pressure measurements in a wind tunnel for a scaled SFS1. It was shown that grid quality is of great significance, and that a coarse grid would result in considerably over-predicted separation region. The validated code was then employed to investigate the airwake of a US Navy vessel and the results were compared with those of full-scale field measurements. In contrast to the uniform inflow/outflow boundary condition, with the ocean surface modeled as an inviscid wall, it was shown that the application of an atmospheric boundary layer as an inflow/outflow boundary condition and considering the ocean surface as a viscous wall boundary significantly improved the results. Yesilel and Edis (2007) performed steady and unsteady numerical investigation for SFS1 and SFS2 model and presented the results for wind angles of  $0^\circ$ ,  $45^\circ$ ,  $90^\circ$  and  $330^\circ$ . In this investigation the Reynolds-averaged Navier-Stokes equations were solved by employing several turbulence models. The obtained time-averaged velocity fields were also validated by comparison with wind tunnel data. Syms (2008) simulated the flow around SFS1 and SFS2 in  $0^\circ$ ,  $45^\circ$  yaw using the lattice-Boltzmann flow solver PowerFLOW. As the main finding, this investigation showed that mean and unsteady flow field of a frigate-like shape could be captured accurately using a lattice-Boltzmann algorithm. Forrest and Owen (2010) studied the airwake of SFS2 as well as a Royal Navy vessel, at several incidence angles, using detached eddy simulations (DES). The results of this study were compared with wind tunnel data (for SFS2) and field measurement (for Royal Navy frigate). It was concluded that using an ABL velocity profile as a boundary condition improved the agreement between the field data and the numerical results. Using implicit large eddy simulations (ILES), Thornber et al. (2010) studied the airwakes of two different Royal Navy vessels in an ABL at several incidence angles ranging from  $0^\circ$  to  $180^\circ$ . A good agreement between numerical results and those of wind tunnel experiments and full-scale measurements was observed for mean flow, fluctuating quantities and power spectral density. The authors identified the five main features in the ship airwake, corresponding to the turbulent flow structures generated by the masts, the horseshoe-like

vortices located between the hull and sea surface, as well as the shear layers shed from the sides and the top of the hangar, the edge of the flight deck itself, and the longitudinal vortices that were located along the ship deck. Bardera-Mora (2014a) performed wind tunnel measurements on a model with SFS1 geometry. In this investigation, the oil film technique was used for flow visualization over the surface of the flight deck. The velocity fields were obtained using PIV as well as laser Doppler anemometry (LDA). In addition to time-averaged velocity components, turbulence intensity was also calculated for several angles of incidence between  $0^\circ$  to  $180^\circ$ . It was shown that high turbulence levels corresponded to incidence angles of  $20^\circ$ ,  $40^\circ$  and  $100^\circ$ . This study also compared the real frigate geometry with that of SFS1. Despite the discrepancy between results for small incidence angles, it was concluded that the SFS1 geometry was capable of predicting the airflow over the helicopter platform. Bardera-Mora and Meseguer (2014) investigated the effects of hangar roof curvatures on the near airwake of a modified SFS. Using PIV, the authors investigated the velocity fields and evaluated the Reynolds stresses. Moreover, pressure distribution in the wake was measured using electronic scanners. It was shown that rounding the hangar roof would reduce the effect of the separated shear layer on the operation of helicopters.

In addition to small-scale experiments and numerical simulations, full-scale measurements have been performed. For instance, Brownell et al. (2012) conducted in-situ measurements in the near-wake of a naval vessel for a case of  $0^\circ$  inflow (headwind). In addition to mean flow, Reynolds stresses and turbulent intensity were also obtained at different locations on the flight deck. Bardera-Mora (2014b) compared the field measurements of velocity components on the flight deck of a frigate with wind tunnel measurements. In contrast with the uniform inflow employed in the wind tunnel experiments, the field data was obtained in the oceanic boundary layer and, therefore, relatively high discrepancy between field data and wind tunnel results was observed. It should be noted that due to inherent limitations of the field conditions, in-situ measurements often lack repeatability and have limited spatial resolution.

In investigations of small-scale streamlined models in water channels and wind tunnels, Reynolds number similarity between the full-scale and the small-scale test subjects

is commonly required. However, while aerodynamics of streamlined bodies is significantly dependent on the Reynolds number, there exists evidence of Reynolds number independence in the case of bluff bodies, provided that the Reynolds number exceeds a certain minimum value. Previous studies, identified this minimum value for buildings and vessels as  $Re = 11000$  (Healey, 1987; Healey, 1992; ASCE, 1996)

The present experimental investigation was performed on a 1:522 scaled model of a CCG polar icebreaker. In order to evaluate the effect of the oncoming flow, this study was conducted in two types of inflow conditions: a uniform flow and a simulated atmospheric boundary layer (ABL). Formation of the ship airwake is due to the combined effect of the forward motion of the ship and the prevailing wind (Forrest and Owen, 2010; Kääriä et al., 2013), which correspond to the uniform inflow and the simulated ABL, respectively. Incidence angles of the vessel with respect to the oncoming velocity ( $\alpha$ ) varied between  $0^\circ$  and  $330^\circ$ . Velocity fields in several vertical and horizontal planes were obtained and used to calculate streamlines, patterns of the out-of-plane vorticity and turbulence metrics, i.e. Reynolds stresses and turbulence levels, over the helicopter platform. The turbulence metrics are indicative of intensity of turbulent fluctuations and are required for the prediction of unsteady loading on a helicopter operating in the ship airwake (Brownell et al., 2012). These fluctuating forces and moments on the rotor and fuselage, caused by airwake disturbances and severe spatial velocity gradients, are known to significantly impact the pilot's workload (Kääriä et al. 2012; Kääriä et al., 2013) and influence the design of helicopter landing platforms (CAP437, 2008).

## **2.2 Experimental system and techniques**

### **2.2.1 Inflow conditions**

Experiments were conducted in a flow visualization water tunnel with a test section that had 2.5 m of working length, and 45 cm of width and depth. Water was used as a working fluid to represent the airflow over the superstructure of the vessel. In order to simulate the ABL in the water channel, an experimental configuration of the type developed by Irwin

(1981) was used. As shown in Fig. 2-1, the setup involved placing triangular spires with the height  $h = 7/9 H$ , where  $H = 45$  cm is the height of the test section, at the entrance of the water channel and distributed surface roughness elements (cubes with the height  $b = 1/90 H$ ) downstream of the spires over the length  $l = 3.16 H$ . The width of the spires at the wall of the test section was equal to  $0.075 H$ , and the spacing between them was equal to  $0.16 H$ . The spacing between the roughness elements in the streamwise and the transverse directions was equal to  $0.035 H$ . This configuration resulted in the development of a boundary layer with the thickness  $\delta = 0.52 H$  (see Fig. 2-1).

The distribution of time-averaged streamwise velocity component in the simulated ABL, normalized by the streamwise velocity at the edge of the generated boundary layer,  $u_\delta$ , is shown in Fig. 2-2. The velocity profile for an atmospheric boundary layer can be described by a power law profile (Zhou and Kareem, 2002), in which, for open sea conditions, the exponent is equal 0.13 (Counihan, 1975):

$$\frac{u}{u_{ref}} = \left( \frac{z^*}{z_{ref}^*} \right)^{0.13} . \quad (2-1)$$

Considering  $u_{ref} = u_\delta$  and  $z_{ref}^* = \delta$ , Fig. 2-2 shows that the velocity profile for the simulated ABL is in good agreement with the power law curve recommended by Counihan (1975). Fig. 2-2 also shows the scaled model of the CCG icebreaker, which is positioned entirely inside of the generated ABL.

### 2.2.2 Scaled model

Considering the dimensions of the test section as well as the blockage effects, a 1:522 model of the CCG icebreaker was selected for the experiments. The scaled model included aerodynamically-relevant features of the full-scale polar icebreaker. The schematics of the scaled model is shown in Fig. 2-3. The blockage ratio was evaluated at different angles of incidence and ranged between 1% and 5.5%. In the current study, the data was not corrected for blockage due to the relatively low blockage ratio, following West and Apelt (1982), Norberg (1993), ASCE (1996), Okajima et al. (1997) and Blocken et al. (2013). The model

was placed on a custom-built turntable, which was rotated with respect to the oncoming flow using a computer-controlled positioning system, as shown in Fig. 2-4. This setup allowed the incidence angles,  $\alpha$ , to vary between  $0^\circ$  and  $330^\circ$  with a  $30^\circ$  increment.

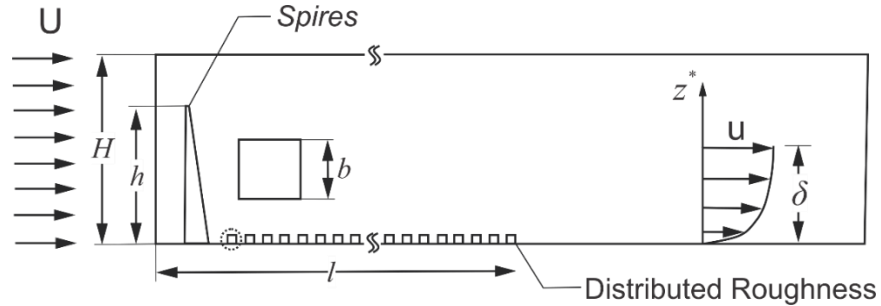


Fig. 2-1. Schematic of flow conditioning elements.

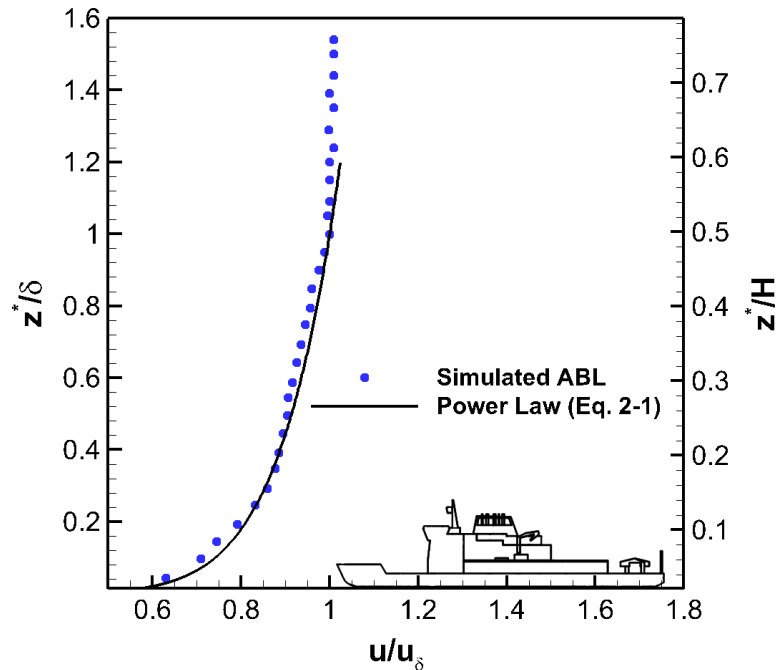


Fig. 2-2. Distribution of time-averaged streamwise velocity in the simulated ABL.

### 2.2.3 Quantitative flow imaging

Global, instantaneous velocity measurements in several vertical and horizontal data acquisition planes were obtained using high-speed particle image velocimetry (PIV). Implementation of PIV involved seeding the flow with tracer particles that were illuminated by a pulsed laser and photographed using a high-resolution digital camera. The

PIV system consisted of a Nd:YLF dual diode-pumped laser (Darwin-Duo series by Quatronix) that had a power output of 25 mJ/pulse, a camera with a complementary metal oxide semiconductor (CMOS) sensor that contained  $1024 \times 1024$  pixels and a computer equipped with hardware for synchronization of the laser pulsing and image capture as well as software for controlling the data acquisition and processing of the raw PIV data (LaVision DaVis 7.2). Silver-coated hollow glass spheres with the average diameter of  $13\mu\text{m}$  and the density of 1.6 g/cc were used as flow tracers.

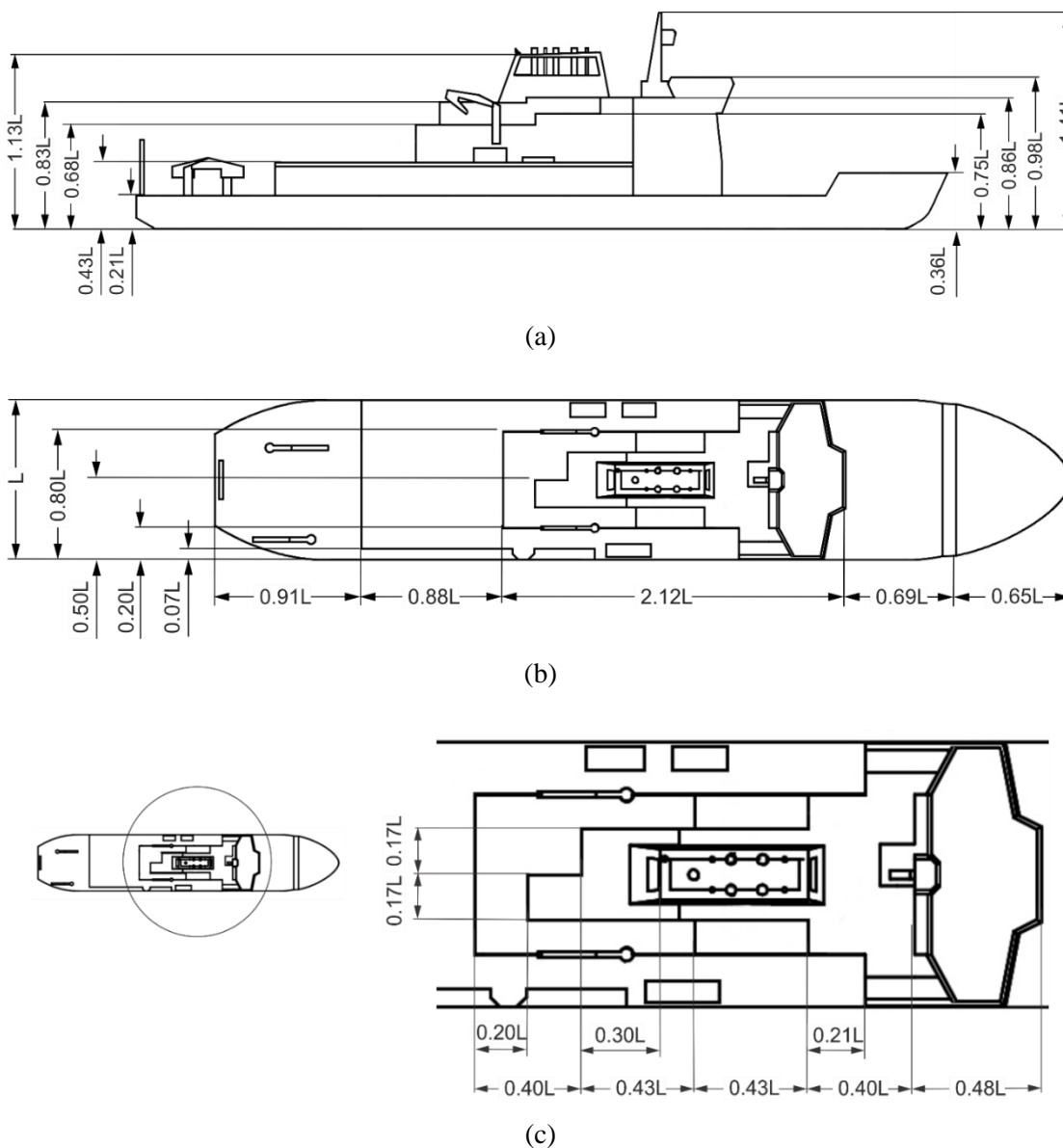
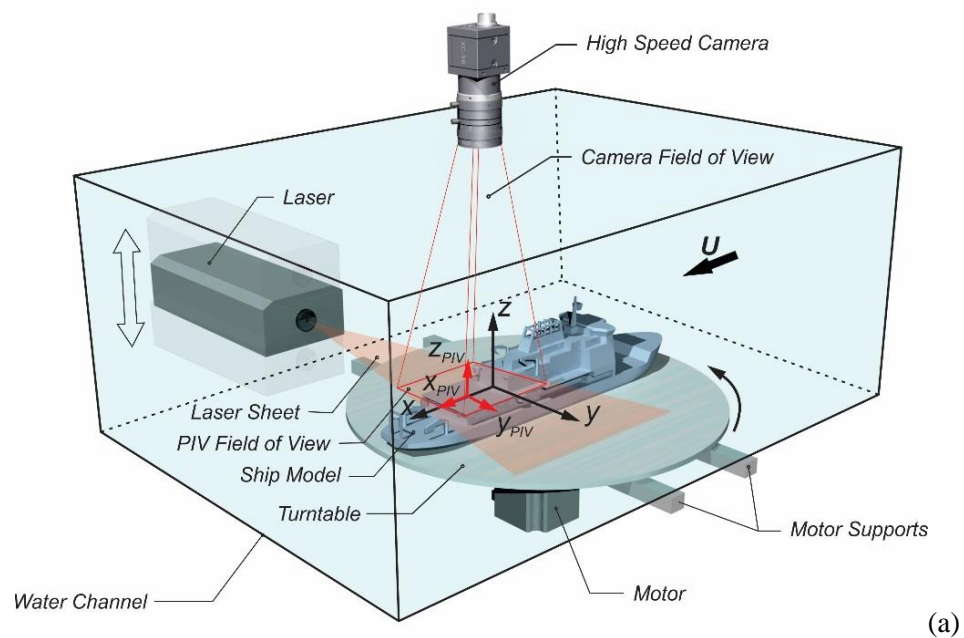
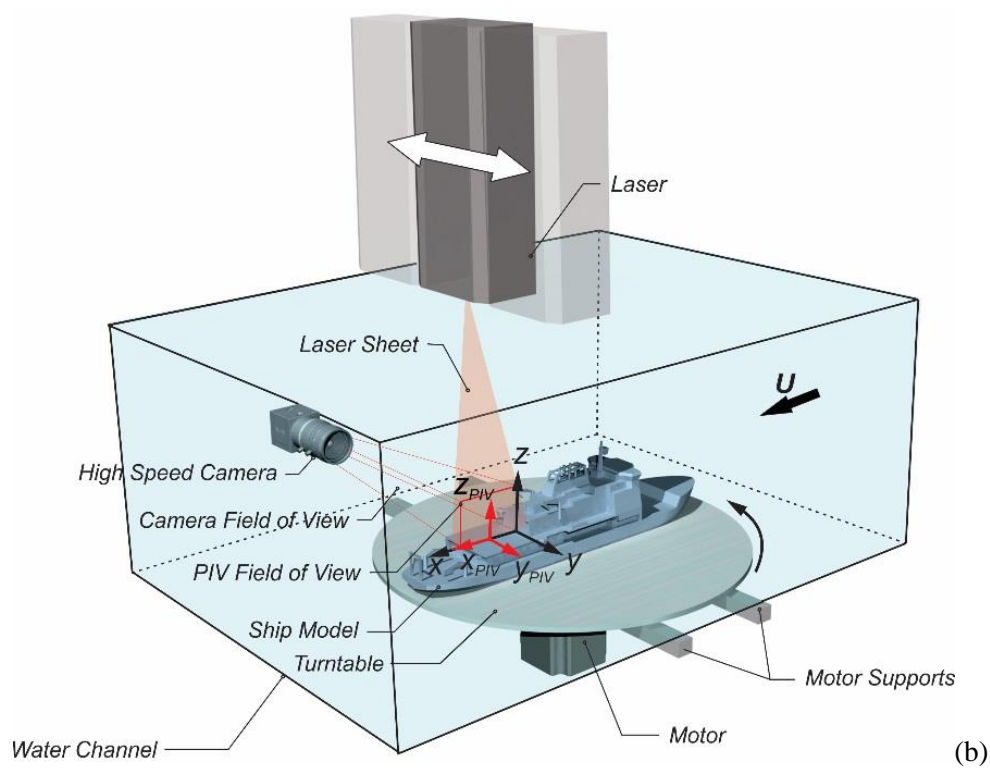


Fig. 2-3. The schematics of CCG icebreaker: (a) side view, (b) plan view (c) closeup of the superstructure.



(a)



(b)

Fig. 2-4. Schematic of the experimental setup: (a) vertical (b) horizontal data acquisition planes.

The laser beam was transformed into a planar light sheet that defined the data acquisition plane. The thickness of the laser sheet was approximately equal to 1.5 mm, which corresponded to 2.96% of the characteristic length (the beam of the ship). The light scattered by the tracer particles was recorded by the CMOS camera. For each experimental condition, a time sequence of 1,800 images were acquired at the frequency ranging from 450 to 550 Hz, depending on the characteristic flow speed. The images were sub-divided into smaller regions, i.e. interrogation windows, which ultimately determined the spatial resolution of the obtained velocity field. The instantaneous velocity fields were calculated using LaVision DaVis 8.2 software by cross-correlating the patterns of tracer particles in interrogation windows in consecutive images. In order to reduce the computation cost of the direct cross-correlation in the spatial domain, the frequency domain-based correlation was used. In the latter approach, the discrete fast Fourier transform (FFT) was applied to the image intensity field for two interrogation windows in consecutive images, followed by a complex-conjugate multiplication of the resulting Fourier coefficients. The cross-correlation function (in spatial domain) was then computed by taking inverse Fourier transform of the product. For each interrogation window, the location of the dominant peak of the cross-correlation function indicated the average particle displacement vector, and based on the frequency of PIV image acquisition, the velocity components were calculated (Raffel et al., 2007).

A multi-pass interrogation algorithm with the initial window size of 64 x 64 pixels that was subsequently reduced to 16 x 16 pixels, was applied for both the vertical and the horizontal data acquisition planes. This interrogation algorithm included a 50% overlap between the adjacent interrogation windows. The obtained velocity field had the spatial resolution of approximately 0.460 and 0.604 vector/mm in vertical and horizontal data acquisition planes, respectively. This spatial resolution corresponded to 23 and 30 data points per characteristic length (beam of the ship). In the current investigation, following Benedict and Gould (1996), uncertainty associated with the sampling of a random process was evaluated and it was verified that statistical convergence for the ensemble-averaged parameters (denoted by  $\langle \rangle$ ) was achieved.

Fig. 2-4 shows the scaled model, the PIV system arrangement, as well as the motion control system. In the coordinate system, located on the flight deck,  $x$ ,  $y$  and  $z$  are the streamwise, spanwise and vertical directions, respectively. Additionally, a PIV data acquisition coordinate system ( $x_{PIV}$ ,  $y_{PIV}$ ,  $z_{PIV}$ ) was introduced and located at the center of the flight deck. The PIV coordinate system was fixed in the laboratory frame and did not rotate with the scaled model. The horizontal data acquisition planes were located in  $x_{PIV}$ - $y_{PIV}$  planes at two elevations over the helicopter platform:  $z_{PIV} = 0.25 L$  and  $z_{PIV} = 0.40 L$ , where  $L$  is the beam of the vessel. Furthermore, for each angle of incidence, data acquisition was performed in vertical ( $x_{PIV}$ - $z_{PIV}$ ) planes located at  $y_{PIV} = 0$ ,  $y_{PIV} = 0.20 L$  and  $y_{PIV} = -0.20 L$ .

## 2.3 Results and discussion

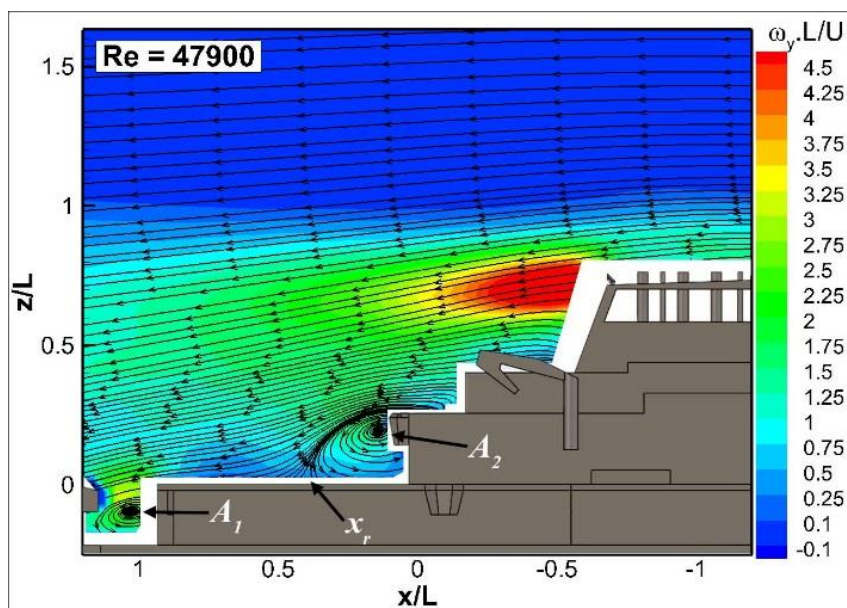
### 2.3.1 Effects of Reynolds number

In this study, the Reynolds number ( $Re = UL/\nu$ , where  $U$  is the characteristic flow velocity,  $L$  is the characteristic length, and  $\nu$  is the kinematic viscosity of the fluid) was defined based on the vessel beam ( $L$ ). The characteristic velocity ( $U$ ) corresponded to the freestream velocity value at the entrance of the test section (see Fig. 2-1). To study the effect of the Reynolds number, the characteristic velocity was varied, which resulted in the values of  $Re = 47900$ ,  $Re = 50500$  and  $Re = 61000$ . The PIV data acquisition in the  $x_{PIV}$ - $z_{PIV}$  plane was performed at  $y = 0$  and  $\alpha = 0^\circ$ .

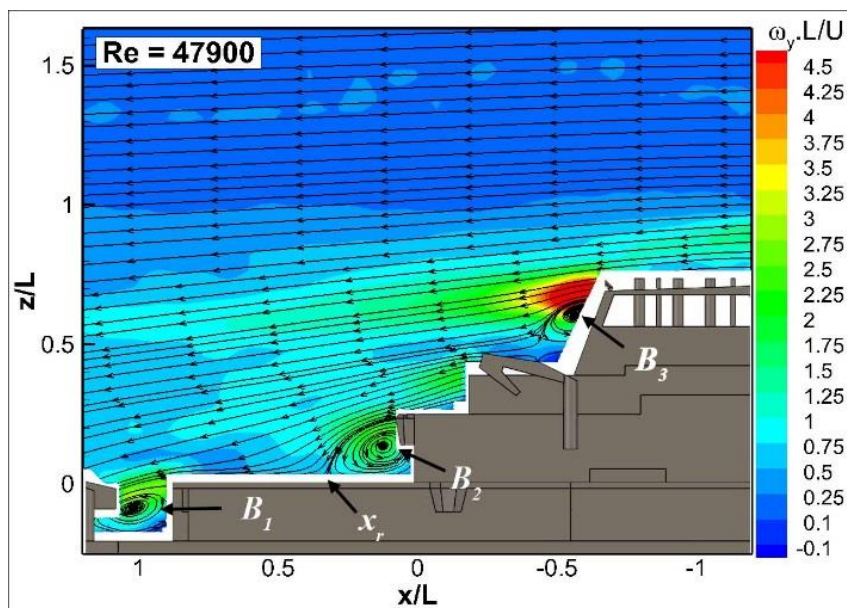
#### 2.3.1.1 Time-averaged flow structure

Fig. 2-5 shows time-averaged streamlines and contours of the out-of-plan vorticity, normalized using the time scale  $L/U$ . Unless specified otherwise, the flow in the figures is from right to left, and a minimum of 1800 instantaneous velocity fields were used to calculate the ensemble-averaged flow patterns. The instantaneous velocity fields were acquired over a time period that was significantly longer than any characteristic flow

oscillation frequencies encountered in these experiments, which make these data appropriate for statistical analysis of the turbulent flow.

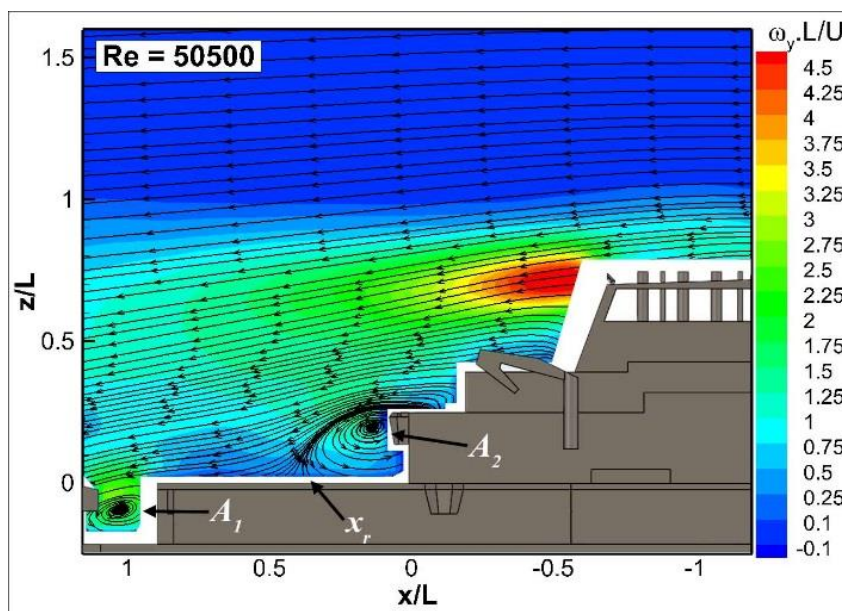


(a)

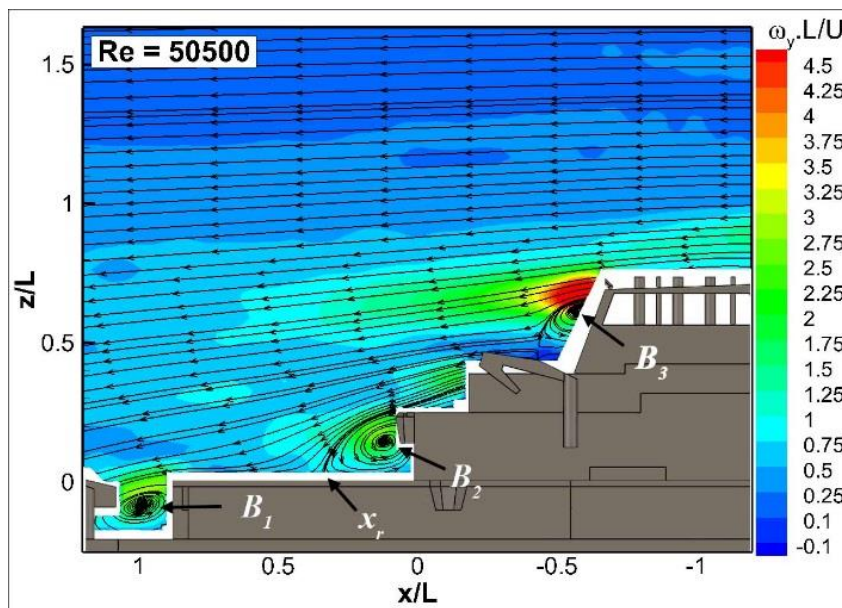


(b)

Fig. 2-5. Time-averaged streamlines and contours of out-of-plane vorticity at  $y = 0$ : (a), (c), (e) - uniform inflow; (b), (d), (f) - ABL.

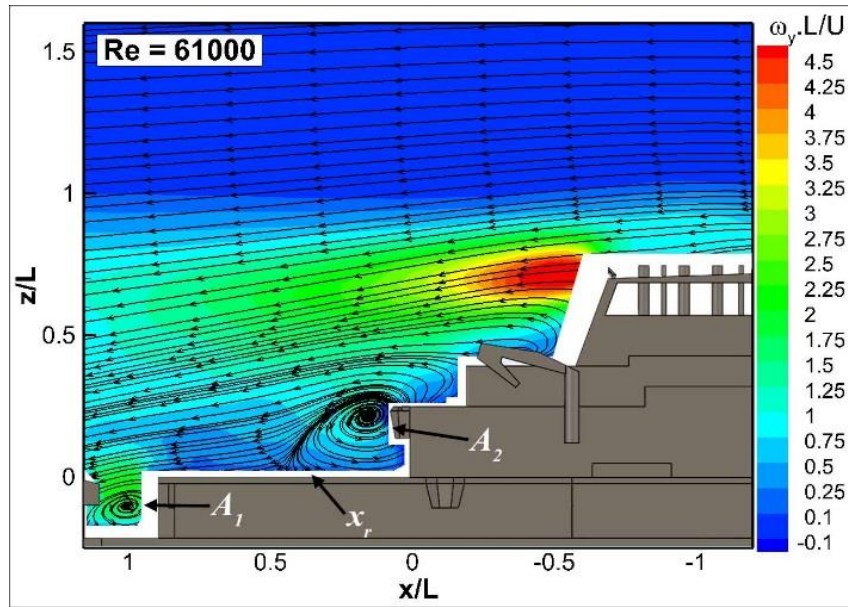


(c)

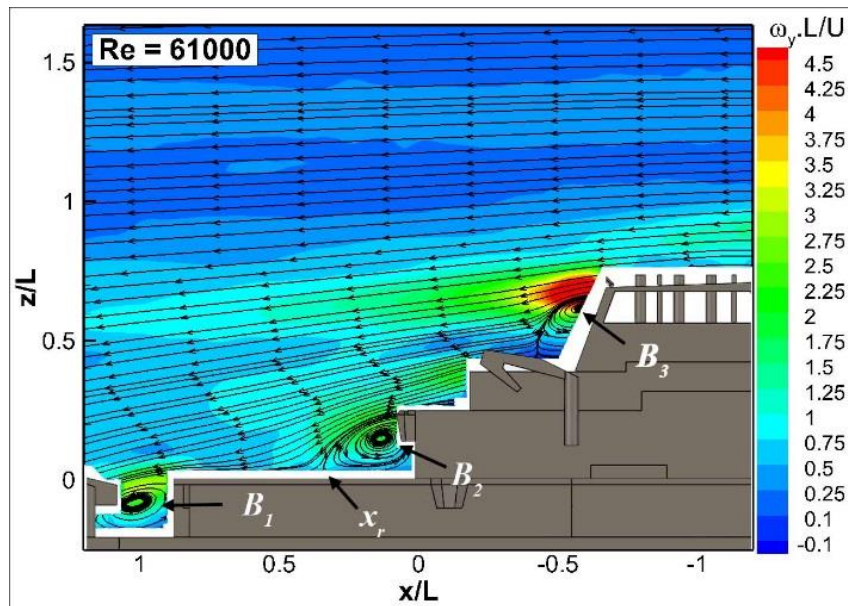


(d)

Fig. 2-5. Continued.



(e)



(f)

Fig. 2-5. Continued.

The recirculation flow zones that exist in the wake are labeled as  $A_i$  and  $B_i$  for the cases of the uniform inflow and the ABL, respectively. The flow reattachment points on the helicopter platform are labeled as  $x_r$ . In the case of the uniform inflow, two distinct recirculation zones,  $A_1$  and  $A_2$ , were evident. In the case of the simulated ABL, an

additional recirculation zone was observed at the top of the superstructure, and in total three pronounced recirculation zones, i.e.  $B_1$ ,  $B_2$  and  $B_3$ , were identified. The location of the flow reattachment points  $x_r$  corresponding to the recirculation zones  $A_2$  and  $B_2$  on the helicopter platform is plotted in Fig. 2-6 as a function of the Reynolds number. Evidently, the absolute values of  $x_r$  were dependent on the inflow condition, although both the uniform inflow and the ABL resulted in qualitatively similar trends of the reattachment length. In the case of the simulated ABL, the recirculation zones were located closer to the vessel than in the case of the uniform inflow. The simulated ABL was associated with shorter reattachment lengths, i.e. more spatially-confined recirculation zones, while the uniform inflow produced recirculation zones that extended farther downstream. This observation, which is based on the streamline patterns, is in agreement with the patterns of the out-of-plane vorticity, which show that the shear layers associated with the flow separation zones were more spatially-confined in the case of the ABL. This phenomenon can be attributed to the lower incident velocity at the superstructure for the case of the simulated ABL.

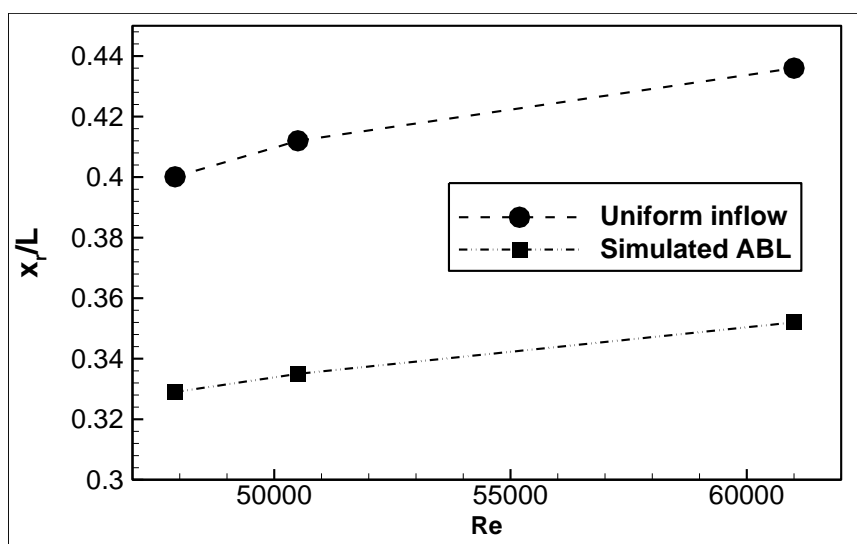


Fig. 2-6. Location of the reattachment points on the helicopter platform for recirculation zones  $A_2$  and  $B_2$ .

Profiles of the mean streamwise,  $\langle u_x \rangle$ , and vertical,  $\langle u_z \rangle$  components of the flow velocity at different locations over the helicopter deck are shown in Fig. 2-7. The mean velocity field did not vary significantly with the Reynolds number, but was strongly dependent on the inflow condition. As the location and the spatial extent of the recirculation

zones were different in the cases of the simulated ABL and the uniform inflow (as demonstrated in Fig. 2-5 and Fig. 2-6), the velocity distributions shown in Fig. 7 exhibited the corresponding qualitative differences. Fig. 2-7(a) and Fig. 2-7(c) show that the streamwise component of velocity increased along the  $x$ -direction. The simulated ABL inflow condition resulted in higher streamwise velocity along most of the length of the helicopter platform. As the downstream distance from the superstructure of the vessel increased, the values of the streamwise velocity corresponding to the uniform inflow reached and eventually surpassed those corresponding to the ABL. The more rapid increase of the streamwise velocity in the case of the uniform inflow can be attributed to the higher incident velocity that interacted with the superstructure, compared to the case of the ABL inflow.

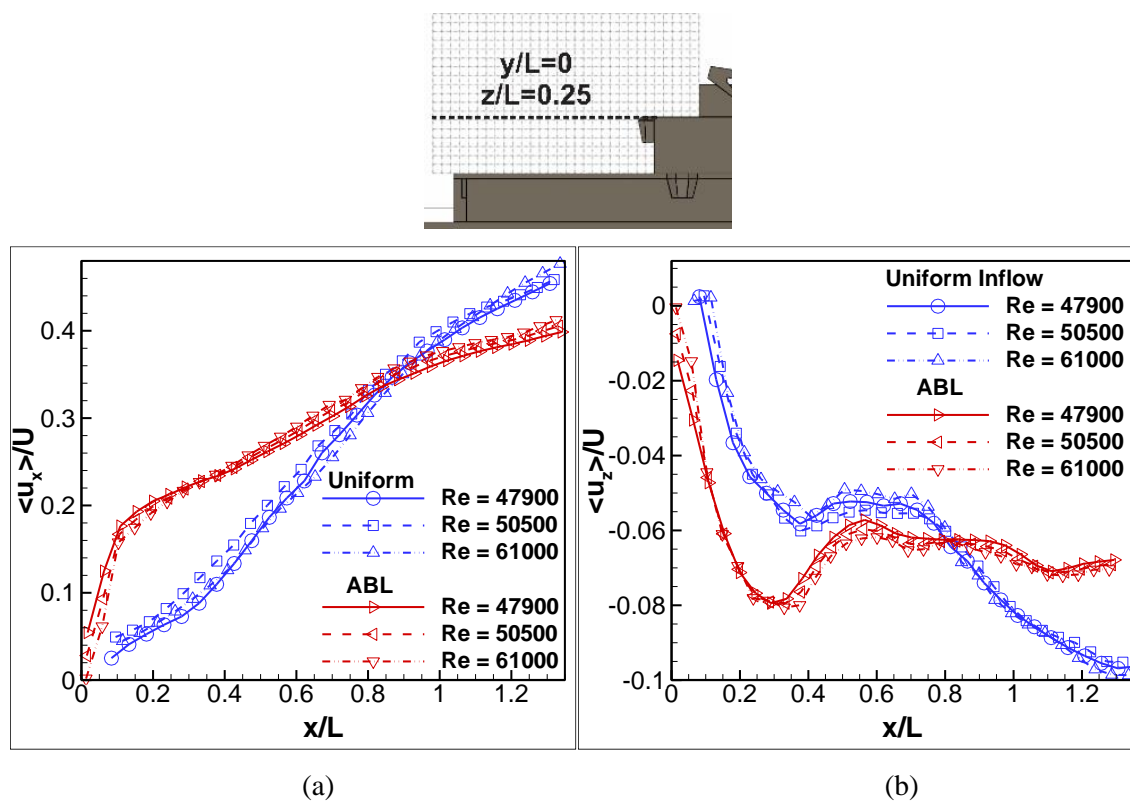
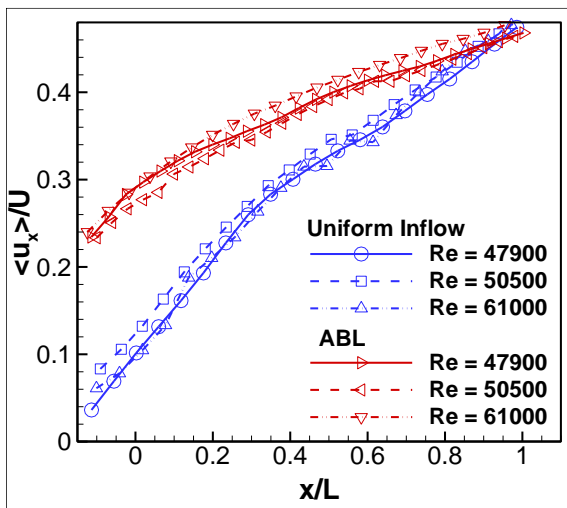
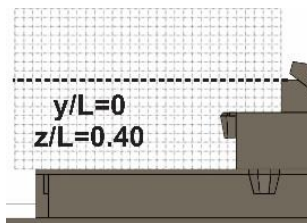
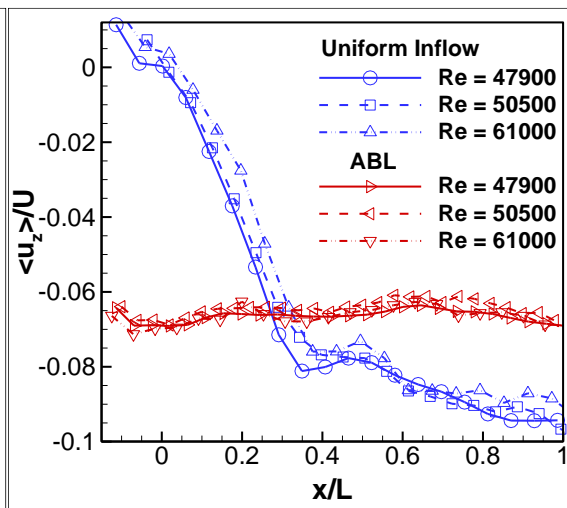


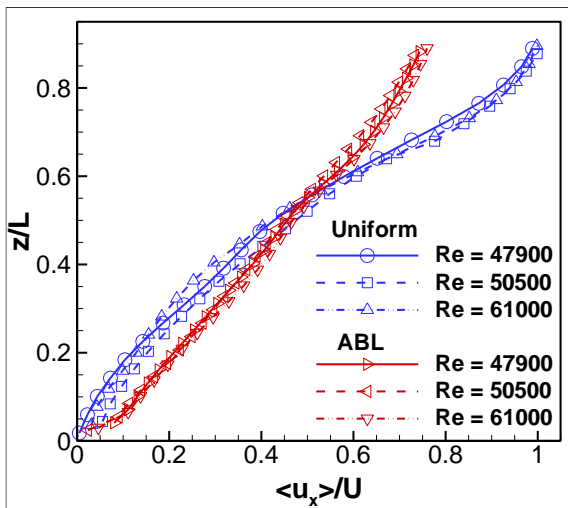
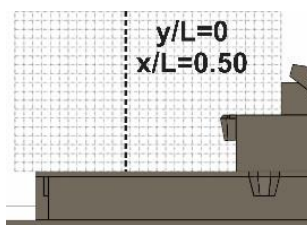
Fig. 2-7. Time-averaged velocity distribution at the centerline of the helicopter platform ( $y_{PIV}/L=0$ ).



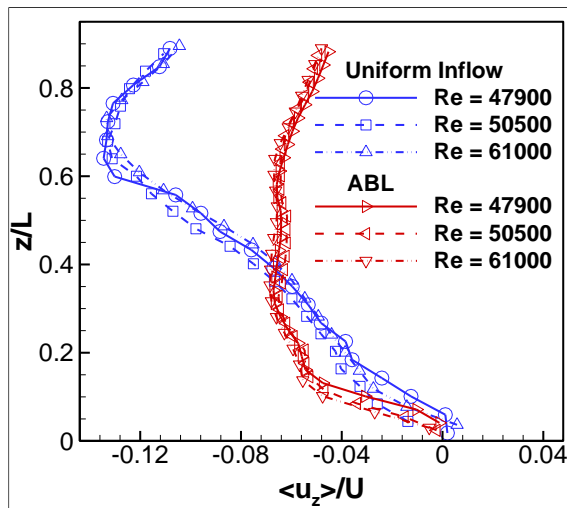
(c)



(d)



(e)



(f)

Fig. 2-7. Continued.

The variation of the vertical velocity component over the helicopter platform at different elevations are shown in Fig. 2-7(b) and Fig. 2-7(d). At  $z/L = 0.25$ , shown in Fig. 2-7(b), the simulated ABL inflow condition resulted in higher values for the magnitude of vertical velocity in the vicinity of the superstructure. As the downstream distance from the superstructure increased, the uniform inflow condition yielded higher velocity magnitudes. This observation is consistent with the trend of the streamwise velocity component, and it is due to the higher incident velocity at any given height in the case of the uniform inflow. Moreover, the local minima in the velocity distributions occurred at  $x/L = 0.3$  and  $x/L = 0.38$  for the cases of the ABL and the uniform inflow, respectively, which is consistent with the location of the recirculation zones shown in Fig. 2-5. At higher elevation ( $z/L = 0.40$ , shown in Fig. 2-7(d)), it was observed that the simulated ABL resulted in an approximately constant value of the vertical velocity along the helicopter platform, while the velocity trend corresponding to the uniform inflow remained similar to the one observed at  $z/L = 0.25$ .

Fig. 2-7(e) and Fig. 2-7(f) show the variation of the streamwise and the vertical velocity components with the elevation from the helicopter platform at  $x/L = 0.50$ . As expected, the velocity magnitude increased to eventually match that of the freestream at the edge of the wake. Furthermore, a peak in vertical component of velocity was observed in the case of the uniform inflow at  $z/L = 0.65$ . It can be inferred that this peak is due to separation of the flow from the top of the superstructure at  $z/L = 0.70$ , which can be observed in Fig. 2-5. In the case of the simulated ABL, this peak was less prominent. Instead, global minimum in the velocity profile occurred at  $z/L = 0.25$ , which corresponded to the separation of the flow from the part of the superstructure located at  $z/L = 0.25$ .

### 2.3.1.2 Turbulence metrics

The workload of the pilot is heavily influenced by the interaction between the ship airwake, associated with large spatial and temporal velocity gradients, and the helicopter (Kääriä et al., 2012; Kääriä et al., 2013). In order to predict the resulted unsteady forces and moments imposed on the rotor and fuselage, quantifying of the turbulent fluctuations is required (Brownell et al. 2012). In the current investigation, in order to evaluate the turbulent

fluctuations, we studied the distribution of the Reynolds stresses over the helicopter platform.

The components of the time-averaged Reynolds stress tensor are calculated as ensemble-averages of the correlations of the fluctuating velocity components  $\langle u'_i u'_j \rangle$  (Pope, 2000). The two-dimensional PIV technique that was employed in the present study yielded three components of the Reynolds stress tensor: the streamwise normal Reynolds stress ( $R_{uu} = \langle u'_x u'_x \rangle$ ), vertical normal Reynolds stress ( $R_{ww} = \langle u'_z u'_z \rangle$ ) and Reynolds shear stress ( $R_{uw} = -\langle u'_x u'_z \rangle$ ). Fig. 2-8 shows the variation of  $R_{uu}$ ,  $R_{ww}$  and  $R_{uw}$ , normalized by  $U^2$ , in the streamwise (x) direction along the centerline of the helicopter platform ( $y/L = 0$ ) at  $z/L = 0.25$  and  $z/L = 0.40$ . At  $z/L = 4.0$ , the peak values of the streamwise normal Reynolds stress  $R_{uu}$  were higher than those of  $R_{ww}$  and  $R_{uw}$ . This observation is in agreement with the results of in-situ measurements reported by Brownell et al. (2012). At the lower elevation ( $z/L = 0.25$ ), velocity fluctuations in the vertical direction, corresponding to the vertical normal Reynolds stress  $R_{ww}$ , were of comparable magnitude, and at certain locations exceeded the fluctuations in the streamwise direction, indicated by the  $R_{uu}$  values.

It should be noted that although the values of the Reynolds shear stress  $R_{uw}$  were lower than those of the normal stress components, they were not negligible, which indicates a substantial degree of anisotropy in the wake of the superstructure. This experimental result is significant because it points to the potential limitation of the fidelity of numerical simulations that employ turbulence models which assume isotropic flow.

The uniform inflow condition was associated with significantly larger values of the Reynolds stresses. For the case of the uniform inflow, the peak values of  $R_{uu}$ ,  $R_{ww}$  and  $R_{uw}$  were approximately two to three times higher than those of the case of simulated ABL. It was also found that, in terms of the peak values of the Reynolds stresses, the discrepancy between inflow conditions was more prominent for  $R_{ww}$  and  $R_{uw}$  (Fig. 2-8(c)-(f)). These observations are limited to the zero incidence angle of the oncoming flow and to the particular location in the  $x$ - $z$  plane ( $y/L = 0$ ), where the velocity data were acquired. The effect of the incidence angle is discussed in detail in Section 2.3.2.

The variation of the same components of Reynolds stress tensor ( $R_{uu}$ ,  $R_{ww}$  and  $R_{uw}$ ) in the vertical ( $z$ ) direction at  $y/L = 0$  and  $x/L = 0.50$  is shown in Fig. 2-9. Similar to the variation in the  $x$ -direction, the peaks in the Reynolds stress distribution corresponded to the location of the shear layers that formed when the oncoming flow separated from the sharp edges of the superstructures. These shear layers are indicated by the elevated values of the out-of-plane vorticity shown in Fig. 2-5.

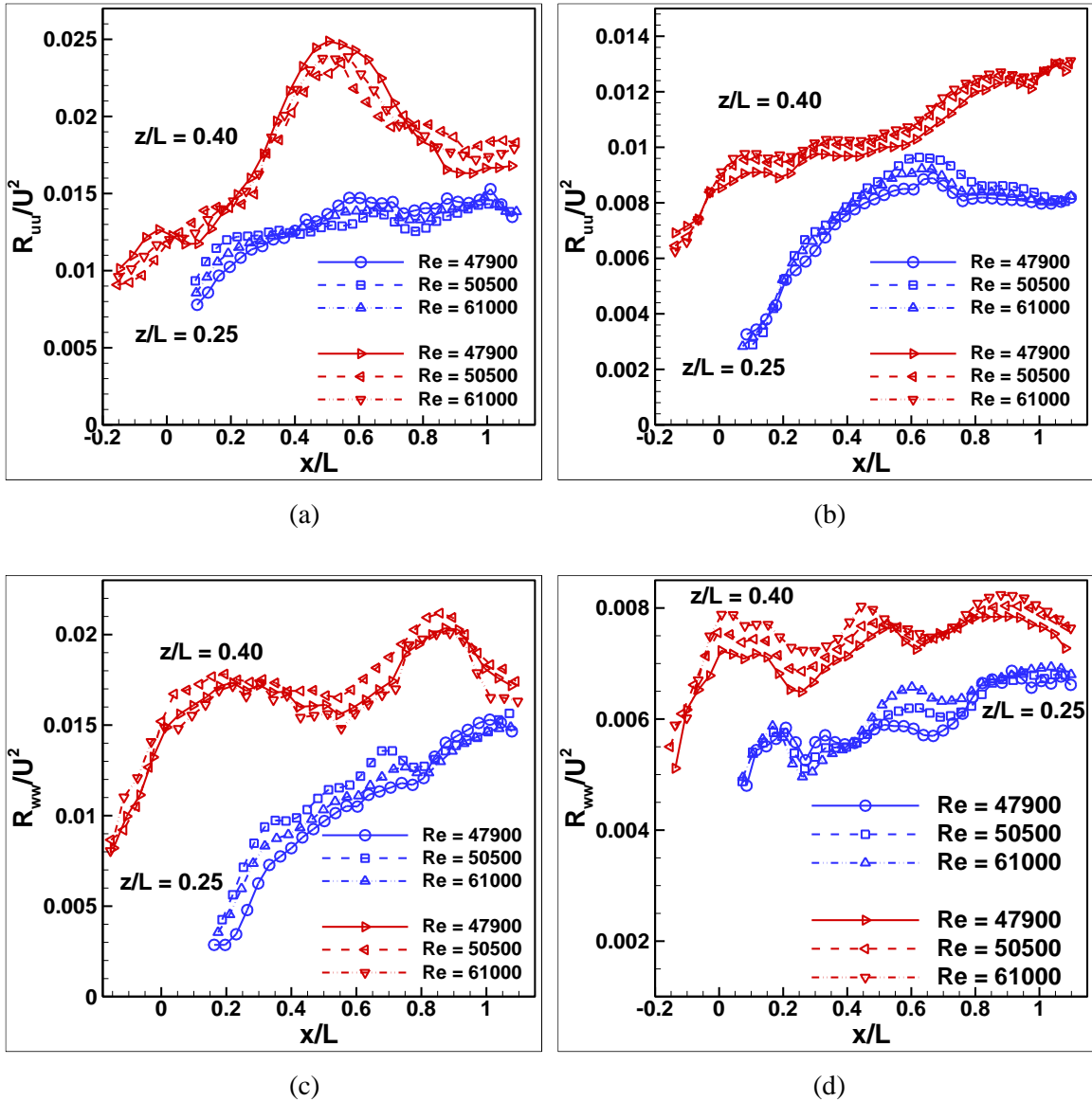


Fig. 2-8. Components of the Reynolds stress tensor at the centerline of the helicopter platform ( $y_{PIV}/L = 0$ ) as functions of the downstream distance ( $x/L$ ) at two elevations above the platform:

(a), (c), (e) - uniform inflow; (b), (d), (f) - simulated ABL.

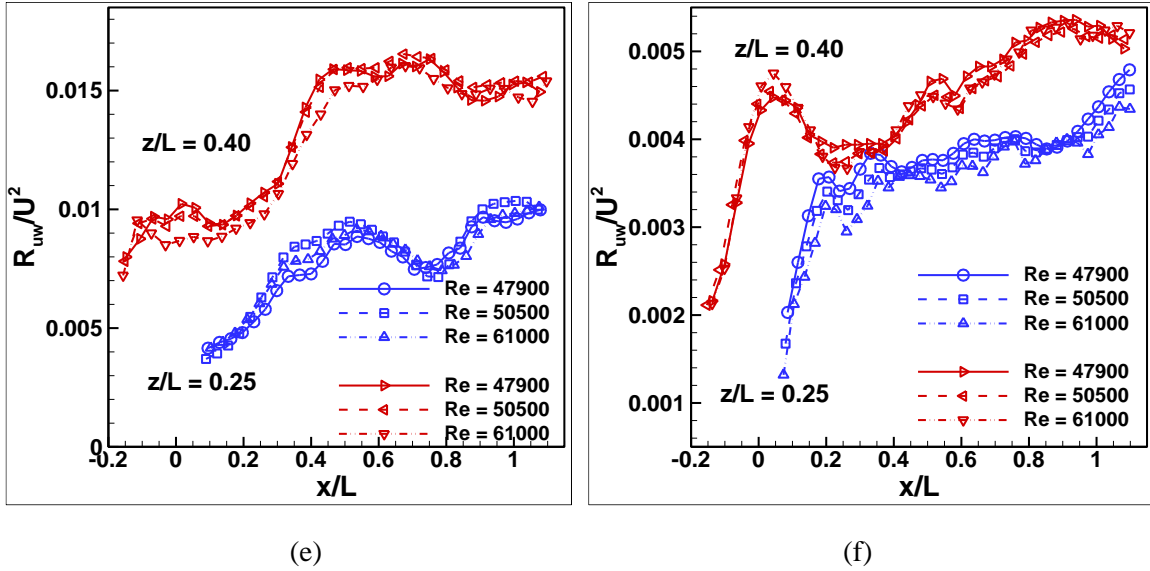


Fig. 2-8. Continued.

In general, the Reynolds stresses increase with elevation above the helicopter platform to a maximum value at approximately  $z/L = 0.65$  in the case of the uniform inflow and  $z/L = 0.55$  for the ABL inflow. The velocity fluctuations then decrease to eventually match the values present in the freestream. This observation is in agreement with the results of Tinney and Ukeiley (2009). In their investigation of a scale model of a simplified ship in uniform flow, the maximum Reynolds stress was observed at a height comparable to the hangar height, which corresponded to the location of the shear layer formed by separated flow. Similarly, the maximum values for  $R_{uu}$ ,  $R_{ww}$  and  $R_{uw}$  in the present study correspond to the height of superstructure at  $z/L = 0.70$  (shown in Fig. 2-4 and Fig. 2-5).

Similar to the results shown in Fig. 2-8, the peak values of Reynolds stresses were significantly higher for the case of the uniform inflow at zero incidence. Moreover, the difference between the peak values was more considerable for  $R_{ww}$  and  $R_{uw}$  (Fig. 2-9(c)-(f)).

### 2.3.1.3 Reynolds number dependence

The geometry of the superstructure of the CCG icebreaker is a bluff-body with sharp edges, which is associated with a large region of separated flow. In general, the structure of the flow around such bodies, where the separation points are well-defined (they typically

correspond to the sharp edges) is independent of the Reynolds number above a certain threshold value. Thus, the flow patterns at the model scale would be similar to those at the full scale. In this investigation, this assumption was tested by changing the inflow velocity at the entrance of the test section of the water channel. It was observed that the locations of the flow recirculation zones, i.e.  $A_1$  and  $A_2$  for the uniform flow and  $B_1$ ,  $B_2$  and  $B_3$  for the simulated ABL, did not vary significantly for different Reynolds numbers. Moreover, the variation of the location of the reattachment points with the change in the Reynolds number was not substantial (less than 4% of the characteristic length) for both considered inflow conditions. Additionally, as shown in Fig. 2-7, Fig. 2-8 and Fig. 2-9, the distribution of the mean velocity components as well as the Reynolds stresses did not vary significantly with the change in the Reynolds number. These results indicate that the flow patterns in the wake of the superstructure were characterized by massively-separated flow regions and were, in fact, independent of the Reynolds number. It was therefore concluded that the Reynolds number of  $Re = 61000$  was sufficiently large to ensure the fluid dynamic similarity between the scaled model and the full-scale CCG icebreaker. Based on this result, the effects of the incidence angle of the oncoming flow (discussed in Section 2.3.2) were investigated at  $Re = 61000$ .

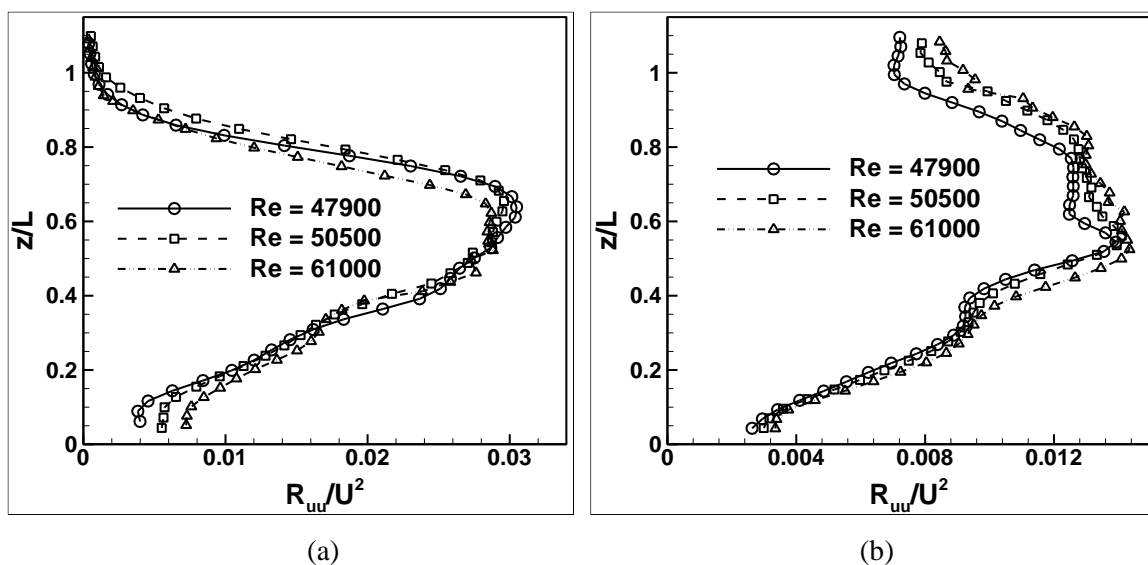
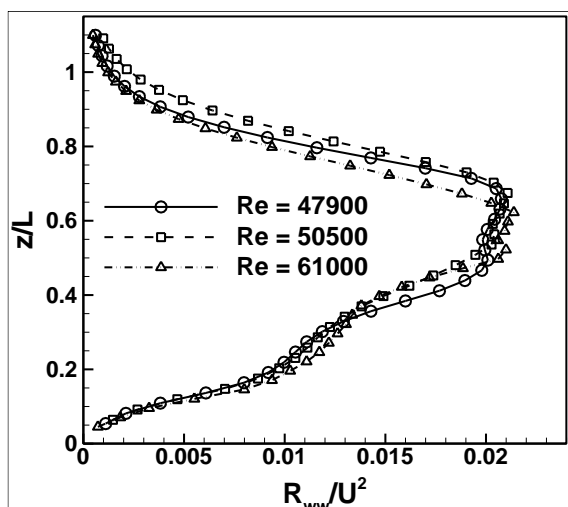
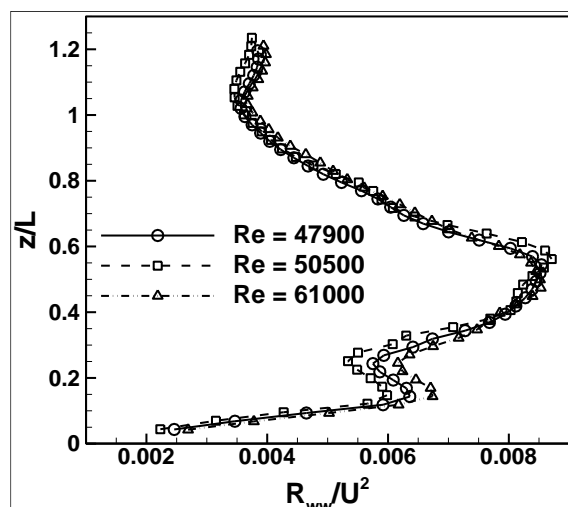


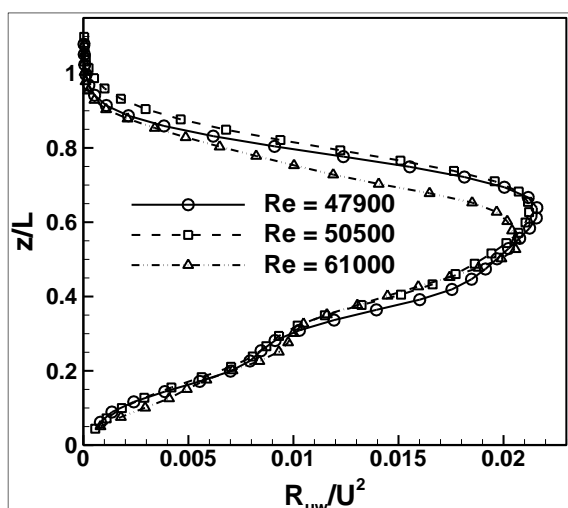
Fig. 2-9. Components of the Reynolds stress tensor at the centerline of the helicopter platform ( $y_{PIV}/L = 0$ ) as functions of the elevation above the platform ( $z/L$ ) at: (a), (c), (e) - uniform inflow; (b), (d), (f) - simulated ABL.



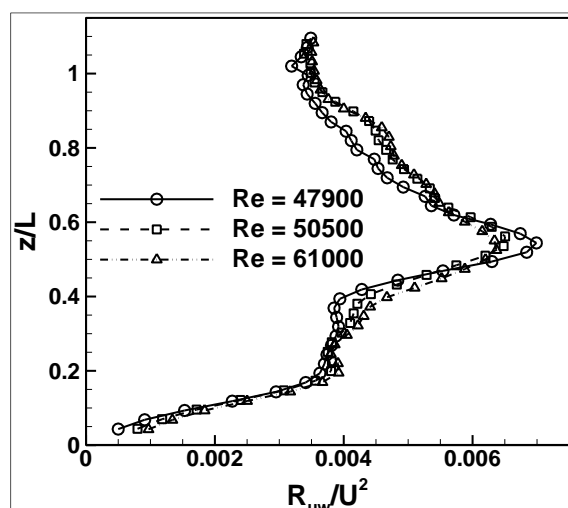
(c)



(d)



(e)



(f)

Fig. 2-9. Continued.

### 2.3.2 Effect of the incidence angle

The scaled model was positioned at various angles of incidence ( $\alpha$ ) with respect to the oncoming flow using a motorized turntable, as shown in Fig. 2-4. For each incidence angle, velocity fields were obtained in three vertical planes in  $x_{PIV}$ - $z_{PIV}$  plane at  $y_{PIV} = 0$ ,  $y_{PIV} = 0.20 L$  and  $y_{PIV} = -0.20 L$ . The obtained velocity fields were used to calculate the turbulence intensity over the helicopter platform. The turbulence intensity was calculated by dividing the standard deviation of the velocity components ( $\sigma_u$  and  $\sigma_w$ , respectively, for the

streamwise and the vertical components of velocity) by the characteristic velocity:  $I_u = \sigma_u/U$ ,  $I_w = \sigma_w/U$  and

$$\sigma_i = \sqrt{\frac{\sum_1^N (u_i - \langle u_i \rangle)^2}{N-1}}, \quad (2-2)$$

where  $N$  is the total number of PIV image pairs. Fig. 2-10 shows the maximum values of turbulent intensity,  $I_{u, max}$  and  $I_{w, max}$ , in the airwake at the different angles of the flow incidence. The maximum values of the turbulence intensity corresponding to the streamwise velocity component ( $I_{u, max}$ ) were higher than those corresponding to the vertical velocity ( $I_{w, max}$ ). This observation is in agreement with the results shown in Fig. 2-8, which is expected, since the turbulence intensity values are closely related to those of the Reynolds stresses. Both  $I_{u, max}$  and  $I_{w, max}$  show the same qualitative trend as functions of  $\alpha$ . Moreover, the maximum value of the turbulence intensity is associated with  $\alpha = 300^\circ$  for both inflow conditions. The ABL inflow resulted in higher values of the turbulent intensity (with the exception of  $I_{w, max}$  at  $\alpha = 0$ ) than the corresponding values for the uniform inflow condition.

It was found that peak values of  $I_{u, max}$  associated with the simulated ABL, were approximately two to three times higher than those corresponding to the uniform inflow. Likewise, the peak values of  $I_{w, max}$  were higher in the case of the simulated ABL. However, the difference in peak values of  $I_{w, max}$  corresponding to the simulated ABL and that corresponding to the uniform inflow, was less prominent than the difference in  $I_{u, max}$  for the two inflow conditions. The higher turbulence intensity in the case of the simulated ABL could be attributed to higher velocity fluctuations in the oncoming flow.

It is instructive to note that the Reynolds stress measurements obtained at  $\alpha = 0^\circ$  (Fig. 2-8) indicate higher turbulence levels in the case of the uniform inflow. While the results shown in Fig. 2-8 were obtained from a single data acquisition plane ( $x$ - $y$  plane at  $y/L = 0$ ), the data shown in Fig. 2-10 contains information about the flow at different incidence angles, obtained at different data acquisition planes. The complex geometry of the ship superstructure results in a highly three-dimensional, unsteady wake. Therefore, it is

important to consider quantitative data from multiple locations in the wake, as well as at various incidence angles, when establishing safety-related thresholds of flow parameters, such as standard deviations of velocity (CAP437, 2008). The lowest values for  $I_{u, max}$  and  $I_{w, max}$  over the helicopter platform corresponded to  $\alpha = 150^\circ$ ,  $\alpha = 180^\circ$  and  $\alpha = 210^\circ$ , when the oncoming flow impinged on the stern of the vessel, instead of the superstructure. This result is intuitive, since the unsteady airwake is the result of the flow interaction with the superstructure.

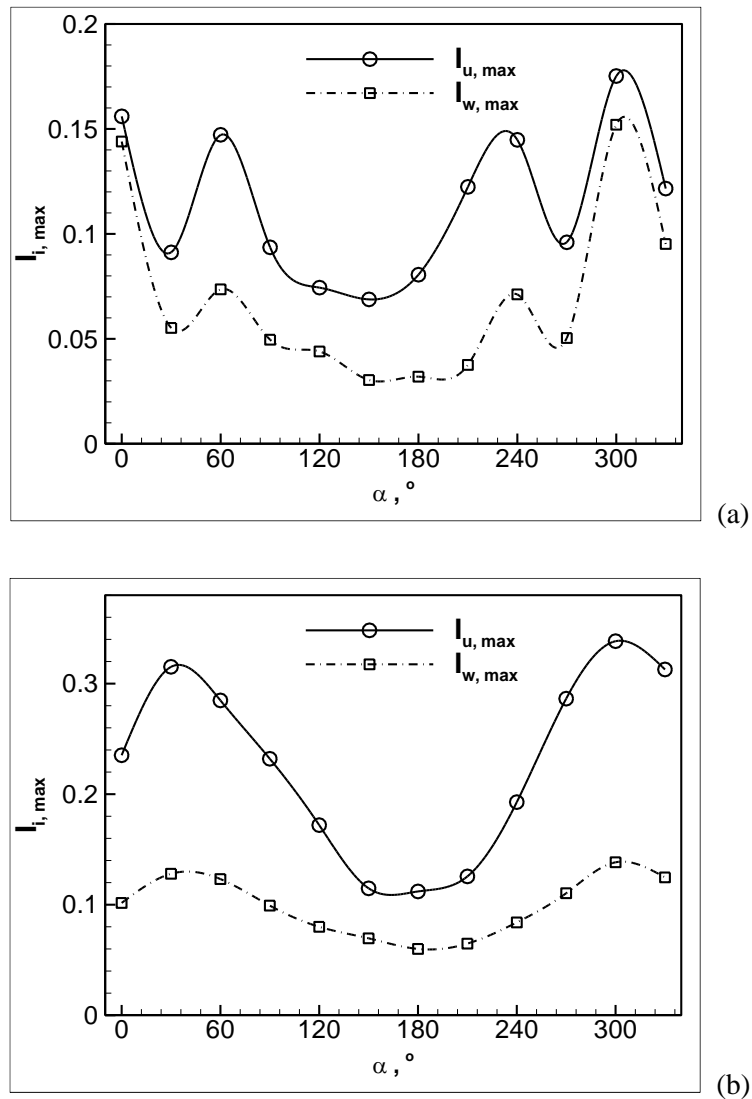
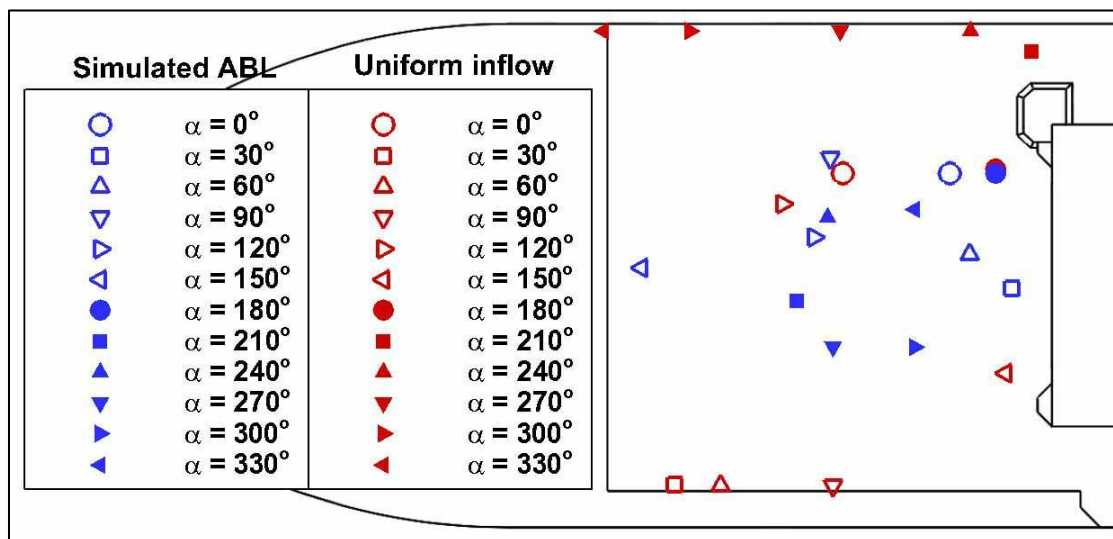
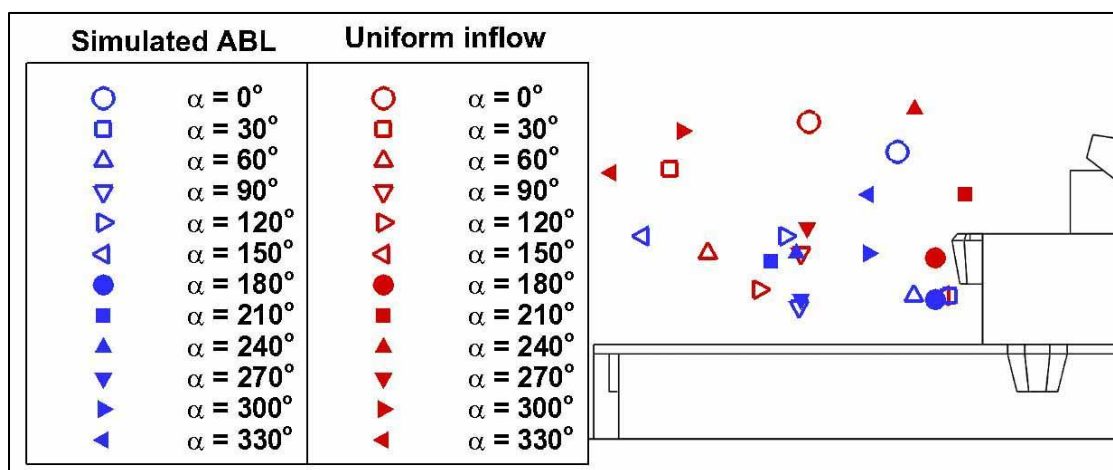


Fig. 2-10. Maximum values of turbulence intensity: (a) - uniform inflow, (b) - simulated ABL.

Locations of the peak values of turbulent intensity,  $I_{u, max}$  and  $I_{w, max}$ , over the helicopter platform is shown in Fig. 2-11 and Fig. 2-12, respectively. It was observed that for the majority of incidence angles, the case of ABL was associated with peak values near the center of the platform. This observation, which is in agreement with the results shown in Fig. 2-5 and Fig. 2-6, could be attributed to the lower incident velocity of the simulated boundary layer and more spatially-confined flow recirculation regions.

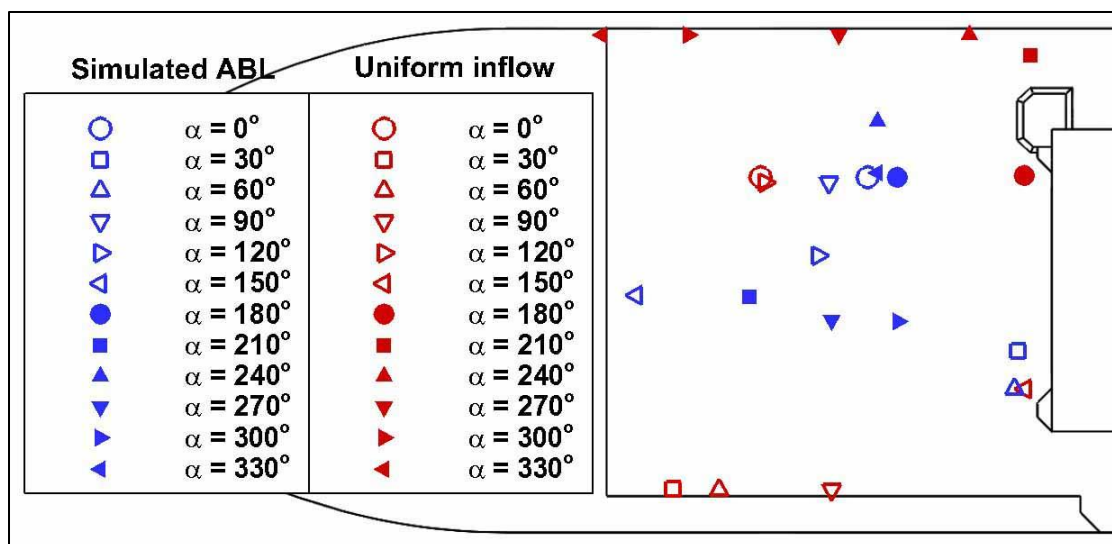


(a)

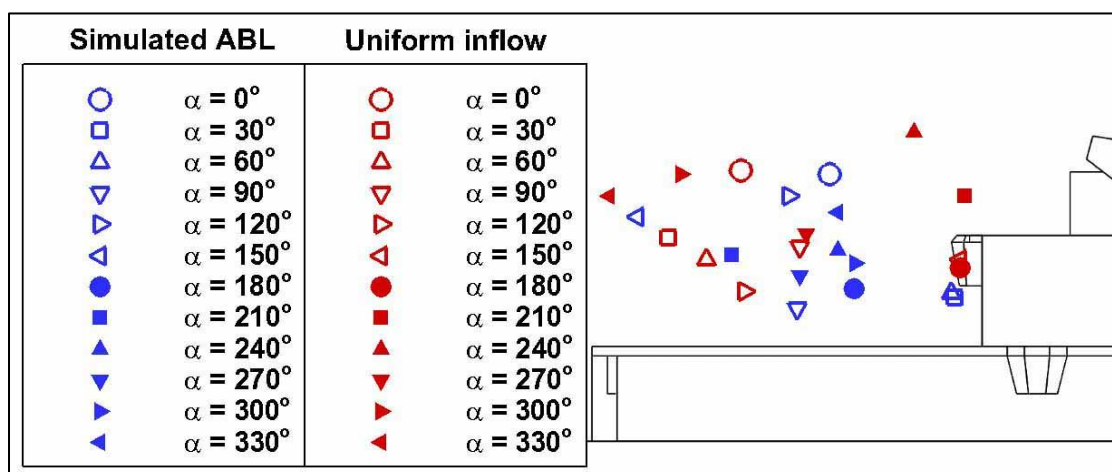


(b)

Fig. 2-11. Location of the peak values of turbulence intensity  $I_{u, max}$ , (a) – x-y plane (b) – x-z plane.



(a)



(b)

Fig. 2-12. Location of the peak values of turbulence intensity  $I_{w, \max}$ , (a) – x-y plane (b) – x-z plane.

It could be concluded that for the case of simulated ABL, the reattachment of the separated boundary layers on the platform surface would lead to high-amplitude velocity fluctuations near in the vicinity of the center of platform. With the exception of the headwind condition ( $\alpha = 0^\circ$ ) and the incidence angles close to tailwind conditions ( $\alpha = 120^\circ$ ,  $\alpha = 150^\circ$  and  $\alpha = 180^\circ$ ), the case of uniform inflow involved the peak values in the periphery of the platform, which indicate that the separated boundary layers did not reattach on the flight deck. It can also be observed that for the majority of the incidence

angles, with the exception of  $\alpha = 120^\circ$  and  $\alpha = 150^\circ$ , the simulated ABL was associated with the peak values located at low elevation from the platform. This observation can also be attributed to spatially-confined recirculation zones in the case of the ABL inflow. The distribution of the peak values was not symmetric with respect to the  $x$ -axis due to the asymmetry of the CCG icebreaker geometry.

For different incidence angles, the variation of the turbulence intensities,  $I_u$  and  $I_w$ , at the center of the flight deck ( $x_{PIV} = y_{PIV} = z_{PIV} = 0$ , see Fig. 2-4) are shown in Fig. 2-13. For the case of the uniform inflow, the maximum turbulence intensity at the center of flight deck was observed at  $\alpha = 0^\circ$ . Moreover, local maxima of both  $I_u$  and  $I_w$  were observed at the incidence angles of  $60^\circ$ ,  $120^\circ$ ,  $240^\circ$  and  $300^\circ$ . In contrast, for the case of the simulated ABL, the maximum  $I_u$  and  $I_w$  were observed at  $\alpha = 0^\circ$  and at  $\alpha = 300^\circ$ , respectively. The local maxima of  $I_u$  and  $I_w$  corresponded to the incidence angles of  $30^\circ$ ,  $90^\circ$  and  $300^\circ$ .

Fig. 2-14 and Fig. 2-15 show time-averaged streamlines and patterns of out-of-plan vorticity in  $x$ - $y$  plane at two elevations above the helicopter platform:  $z/L = 0.25$  (Fig. 2-14) and  $z/L = 0.40$  (Fig. 2-15). Slight asymmetry in the airwake with respect to the centerline of the ship was observed at the incidence angles  $\alpha = 0^\circ$  and  $\alpha = 180^\circ$ . This effect was due to the asymmetric geometry of the superstructure of the vessel. The asymmetry of the flow field increased in case of simulated ABL inflow, as shown in Fig. 2-13(d) and Fig. 2-14(d).

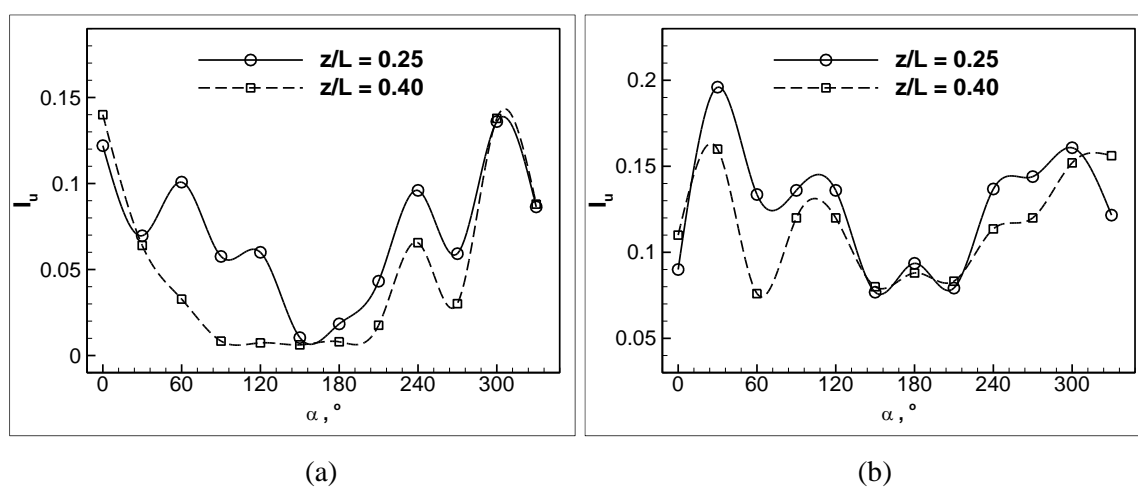


Fig. 2-13. Variation of turbulence intensities,  $I_u$  and  $I_w$ , at the center of the flight deck, with the incidence angle: (a), (c) - uniform inflow; (b), (d) - simulated ABL.

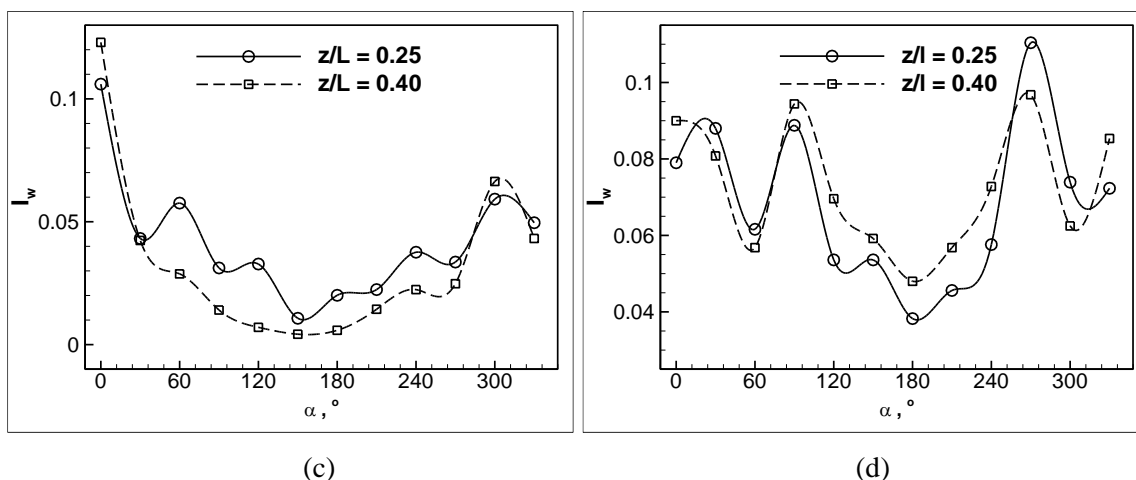


Fig. 2-13. Continued.

Locations of the recirculation zones were significantly affected by the inflow condition at the incidence angles  $\alpha = 0^\circ$  and  $\alpha = 300^\circ$ . In contrast, at  $\alpha = 180^\circ$ , the flow recirculation regions were located at the same positions for uniform inflow and the simulated ABL conditions. It can be concluded that for incidence angles that produced massive flow separation and wider airwake, e.g.  $\alpha = 300^\circ$ , the structure of the wake, in terms of the location of the recirculation zones, was influenced by the inflow condition to the greater extent than at the incidence angles that produced a smaller airwake, e.g.  $\alpha = 180^\circ$ .

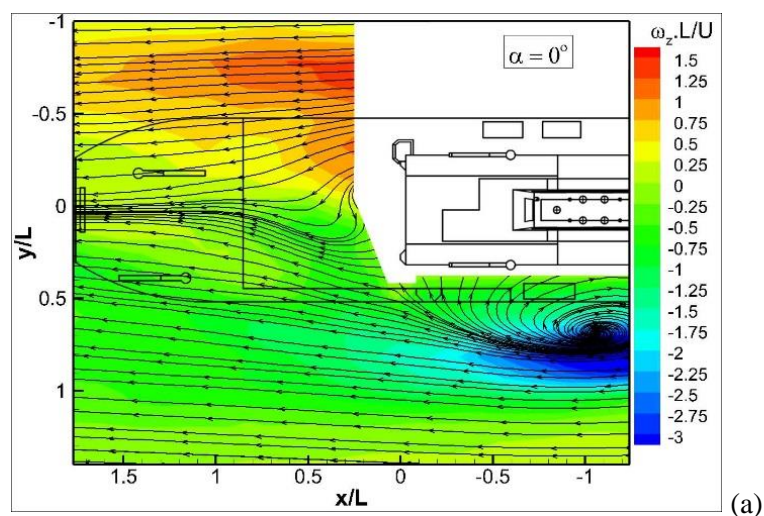


Fig. 2-14. Time-averaged streamlines and contours of the out-of-plane vorticity in the  $x$ - $y$  plane at  $z_{PIV}/L = 0.25$ : (a), (c), (e) - uniform inflow; (b), (d), (f) - simulated ABL.

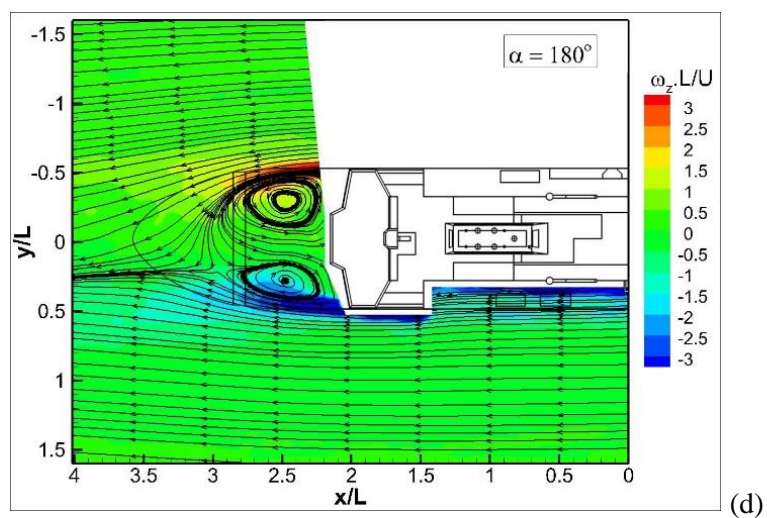
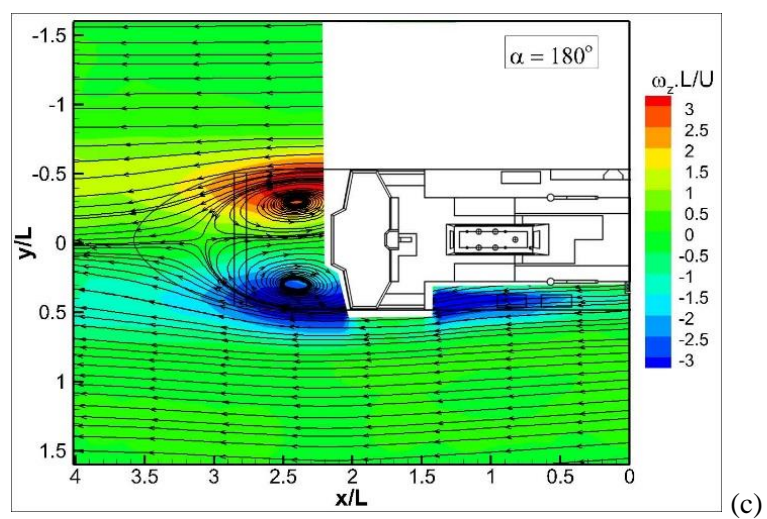
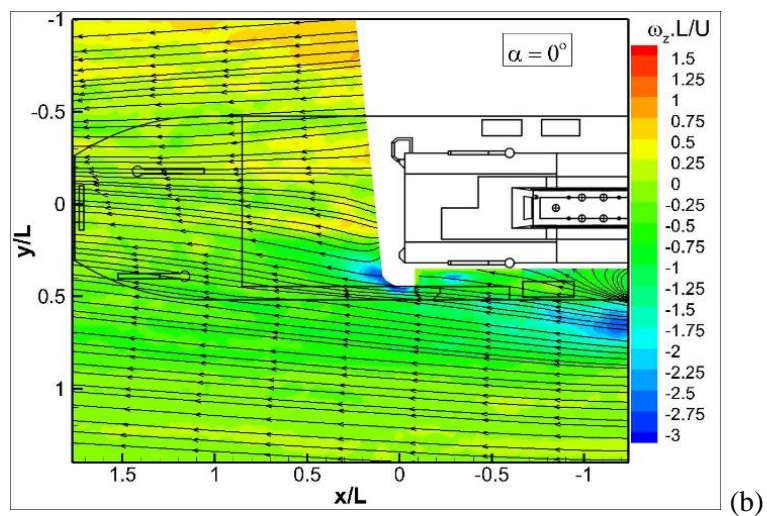


Fig. 2-14. Continued.

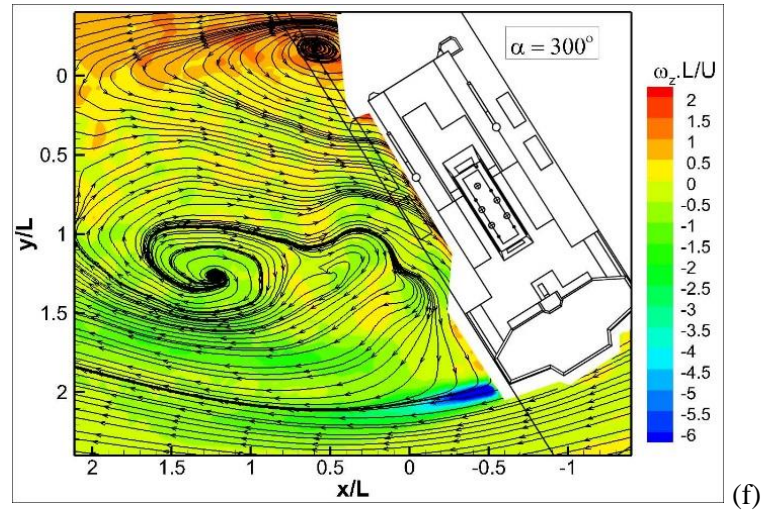
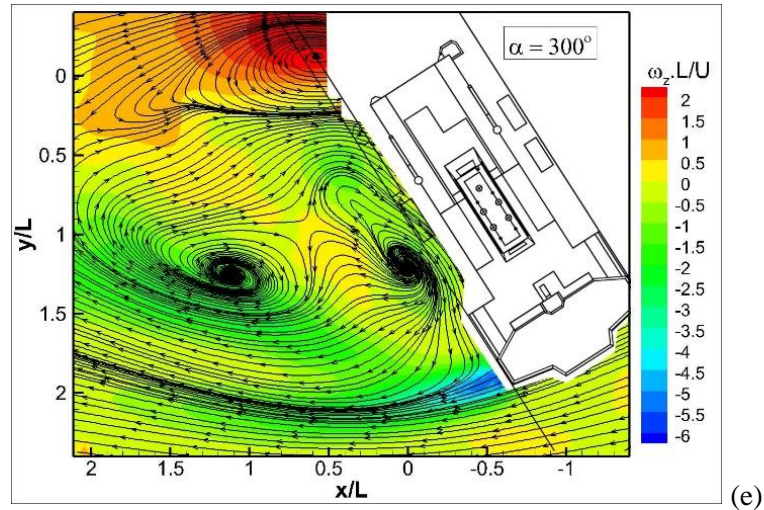


Fig. 2-14. Continued.

Patterns of the out-of-plane vorticity indicate that the airwake was more spatially-confined in the case of simulated ABL, compared to the uniform inflow condition, for the entire range of the incidence angles. This result can be attributed to the lower incident velocity interacting with the superstructure at the lower elevations above the helicopter platform in the case of the simulated ABL. In addition, the velocity gradient in the ABL inflow promoted momentum transfer and development of three-dimensionality of the wake.

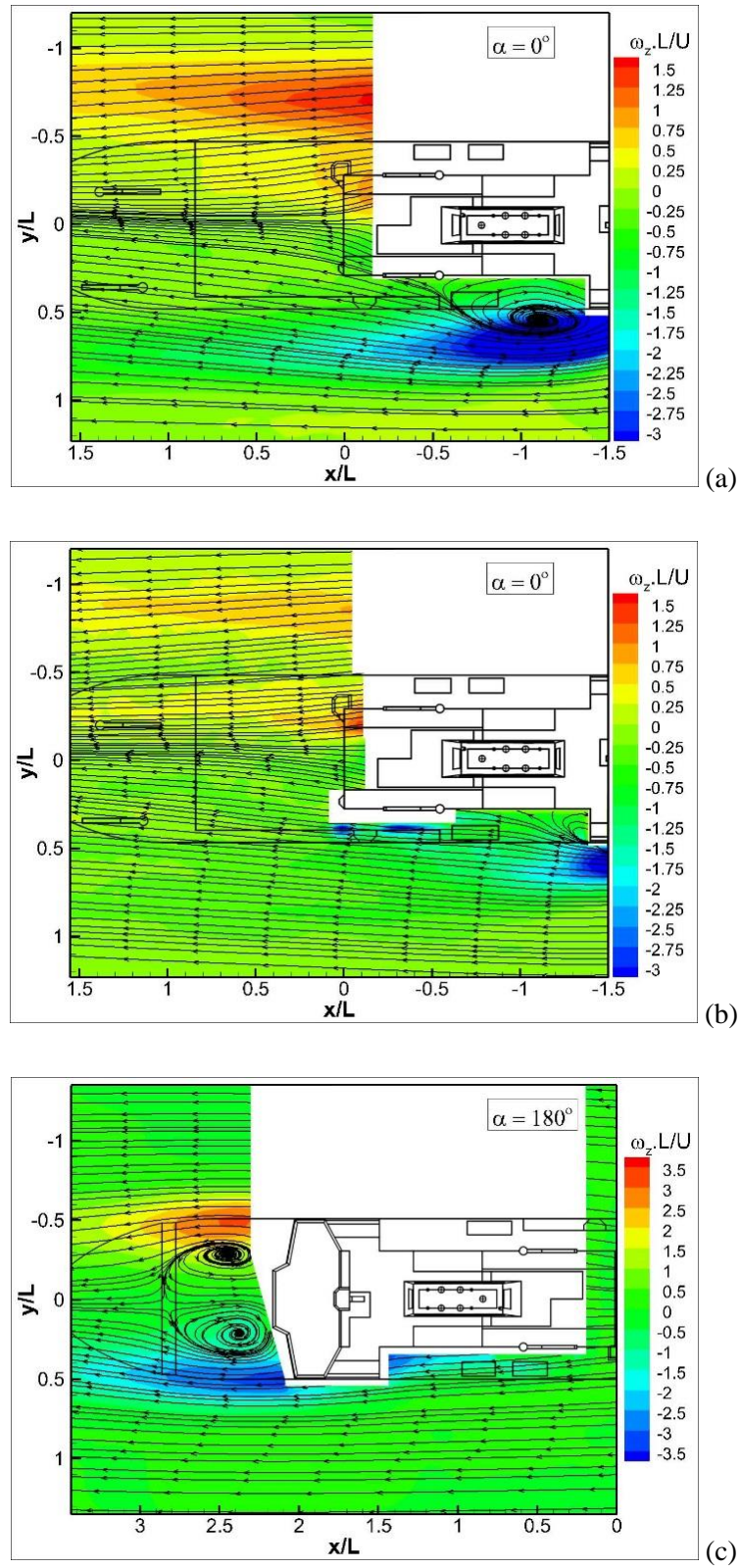


Fig. 2-15. Time-averaged streamlines and contours of the out-of-plane vorticity in the x-y plane at  $z_{PIV}/L = 0.40$ : (a), (c), (e) - uniform inflow; (b), (d), (f) - simulated ABL.

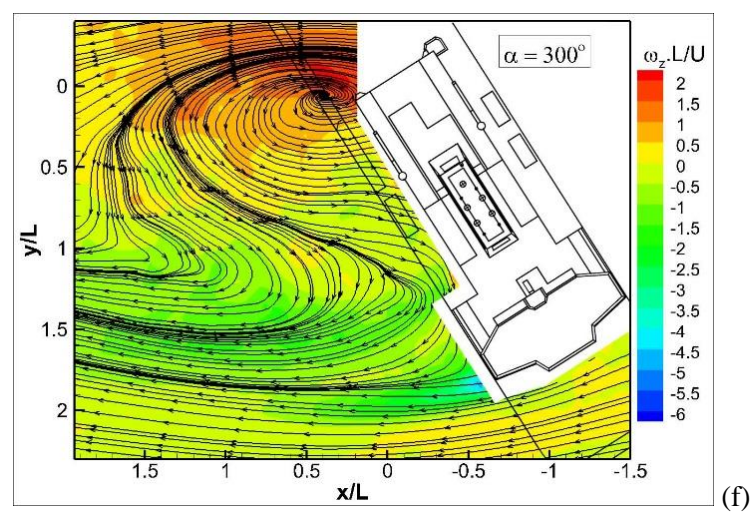
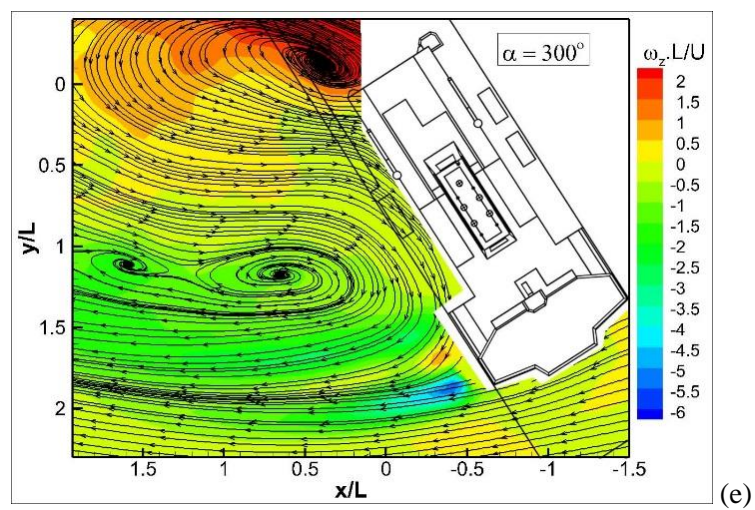
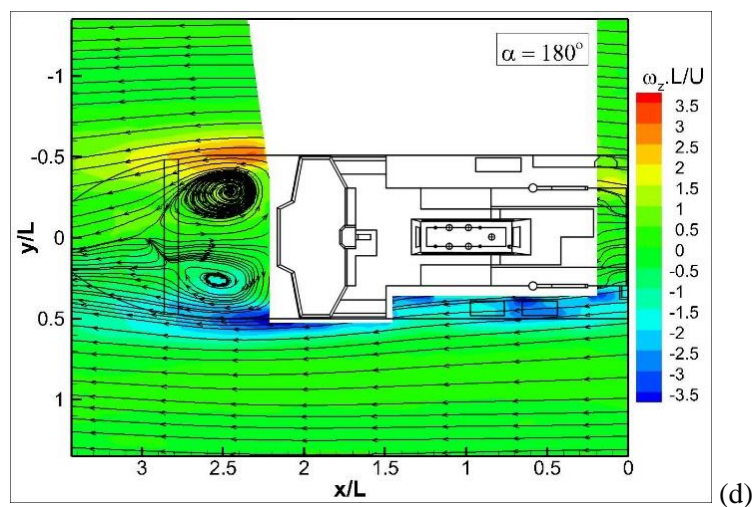


Fig. 2-15. Continued.

## 2.4 Conclusions

The effects of different inflow conditions, namely a uniform inflow and a simulated ABL, on the airwake of an icebreaker vessel were studied experimentally using PIV. The velocity and the vorticity fields were obtained at different angles of incidence in several vertical and horizontal data acquisition planes at both inflow conditions. The simulated ABL promoted development of higher turbulent velocity fluctuations over the helicopter platform, which can lead to an increase in the workload of the pilots. The maximum values of the turbulence intensity were observed at the incidence angle  $\alpha = 300^\circ$ . Moreover, the spatial structure of the airwake substantially depended on the inflow condition, particularly at the incidence angles that resulted in larger-scale flow separation from the superstructure of the vessel.

### **3 The effects of unsteady change in wind direction on the airflow over the helicopter platform of a polar icebreaker**

#### **Preamble**

The body of this chapter has been published as: Mostafa Rahimpour, Peter Oshkai, 2019. The effects of unsteady change in wind direction on the airflow over the helicopter platform of a polar icebreaker, *Ocean Engineering*, 172, 22-30.

DOI: 10.1016/j.oceaneng.2018.11.049.

Explicit permission to reprint the material, as detailed above, in the present dissertation is granted by Elsevier, as the publisher of *Ocean Engineering*.

Contributions: M. Rahimpour designed the study and experimental system, conducted the measurements, collected and post processed the data, performed the analysis and prepared the initial manuscript. P. Oshkai supervised the research, provided insight and contributed to the development of manuscript drafts

## Abstract

The effects of the unsteady change of the wind direction on the airwake over the helicopter platform of a Canadian Coast Guard polar icebreaker were studied experimentally. By application of particle image velocimetry on a scaled model of the icebreaker, quantitative flow field data were obtained for several rates of change in the wind direction. This study was conducted in a water channel that featured a simulated atmospheric boundary layer as inflow condition. The rate of change in the incidence angle,  $\dot{\alpha}$ , varied in the range  $-0.25 \leq \dot{\alpha}L/U \leq 0.25$ , where  $L$  and  $U$  are the characteristic length and velocity, respectively. In addition to the time-averaged velocity fields, the turbulence intensity was evaluated to investigate the unsteadiness of the flow. Increasing the rate of change of the incidence angle of the incoming flow resulted in an increase of the turbulent intensity for all considered nominal incidence angles of the inflow. A notable exception to this trend was observed at  $\alpha = 60^\circ$ , where the direction of the inflow change had a pronounced effect on the structure of the flow over the helicopter deck. Thus, negative values of  $\dot{\alpha}L/U$  resulted in the wake of the superstructure not affecting the flow over the helicopter platform.

**Keywords:** Ship airwake; unsteady wind direction; particle image velocimetry, phase averaging; turbulence metrics.

## 3.1 Introduction

Wind buffeting of the helicopter platforms of ships is an important issue for designers and operators of vessels and helicopters, which promoted early studies on the ship airwake (Rhoades 1983; Healey 1987; Johns and Healey 1989; Healey 1992). When a helicopter experiences unsteady aerodynamic loads in the range of frequencies of  $0.2 \text{ Hz} < f < 2 \text{ Hz}$ , the pilots are subjected to substantially higher workload relative to routine flying conditions due to the need to continually compensate for the effects of the wind (McRuer 1994; Rahimpour and Oshkai 2016). Therefore, a number of studies to date focused on the airflow dynamics in the wake of the ships (Tai and Carico 1995; Polsky 2003; McRuer

1994; Syms 2004; Sezer-Uzol et al. 2005; Woodson and Ghee 2005; Lee and Zan 2005; Syms 2008; Forrest and Owen 2010; Thornber et al. 2010; Snyder et al. 2011; Van Muijden et al. 2013; Bardera-Mora 2014b; Dobrucali and Ergin 2017).

Among these investigations, field studies involving actual ships are particularly valuable because they provide data representative of the realistic scale of the flow phenomena (Snyder et al. 2011; Brownell et al. 2012; Bardera-Mora 2014b). However, the testing conditions during field experiments are not repeatable and are therefore difficult to generalize for design and operation guidelines of other ships operating under slightly different wind conditions.

The issues of repeatability of the conditions are commonly addressed by conducting model-scale experiments in laboratory. In order to establish a common basis for describing the vessel geometry and allow generalization of the results, Standard Frigate Shape (SFS) models have been developed for scaled experimental testing as well as validation of computational models (Wilkinson et al. 1998; Zan et al. 1998; Cheney and Zan 1999; Reddy et al. 2000; Zan 2001; Toffoletto et al. 2003; Polsky 2003; Yesilel and Edis 2007; Tinney and Ukeiley 2009; Bardera-Mora 2014a; Bardera-Mora and Meseguer 2014; Forrest et al. 2016). This model features a simplified superstructure that retains the significant characteristic features of frigate-class vessels, while ignoring ship-specific elements that would add variance to the experimental results.

Several studies examined the effects of the inflow conditions on the resulting airwake of a ship. It has been shown by Polsky (2003), Forrest and Owen (2010), and Rahimpour and Oshkai (2016), among others, that uniform inflow leads to significant differences in the spatial structure of the wake as well as in the peak levels of the turbulent intensity, compared to the case of a simulated atmospheric boundary layer (ABL) as the inflow condition.

In addition to examining the interaction of wind and superstructure and the resulted airwake, several studies investigated the unsteady forces and moments exerted on a helicopter, approaching the vessel and operating in the wake (Kääriä et al. 2012; Kääriä et

al. 2013). It was found that, in addition to the modification of aerodynamic design of superstructure, the incidence angle of the incoming flow could significantly influence the unsteady loading on the helicopter. In particular, it was observed that pilots would experience greater workload levels through the lateral translation phase of the helicopter.

While the previous investigations significantly contributed to the understanding of the fluid mechanics of ship airwakes, several issues remain unresolved. In particular, to the best of our knowledge, none of the prior studies considered the effects of transient changes of the inflow direction on the wake of the superstructure. The transient changes in the inflow can occur both naturally and due to maneuvering of the vessel. While the vessel operation can be controlled, natural wind fluctuations in the azimuthal direction can interfere with helicopter operation. In the present study, we considered the effects of the transient changes of the inflow direction by rotating the scaled model of the ship with respect to the oncoming flow. For several incidence angles, both the rate of rotation and the direction of rotation were varied, and the resulting wake was analyzed. The considered rates of change of the inflow direction corresponded to full-scale azimuthal velocities up to 105.5 deg/hr. This range of velocities is representative of temporal changes in wind direction, which is reported to fluctuate from 1.6 deg/hr (van Doorn et al. 2000) to approximately 100 deg/hr (Ezraty 1990).

## **3.2 Experimental system and techniques**

### **3.2.1 Inflow conditions**

The experiments were conducted in a flow visualization water tunnel that had a test section with 45 cm x 45 cm cross-section and 2.5 m length. The 1:522 model of the Canadian Coast Guard (CCG) polar icebreaker included aerodynamically-relevant features of the full-scale vessel. The model was placed on a turntable, which was rotated with respect to the oncoming flow using a computer-controlled positioning system, as shown in Fig. 3-1. The blockage ratio of the scaled model was evaluated at different angles of incidence and ranged between 1% and 5.5%, and, following West and Apelt (1982), Norberg (1993),

Okajima et al. (1997), ASCE 1996 and Blocken et al. (2013), the blockage effects were neglected.

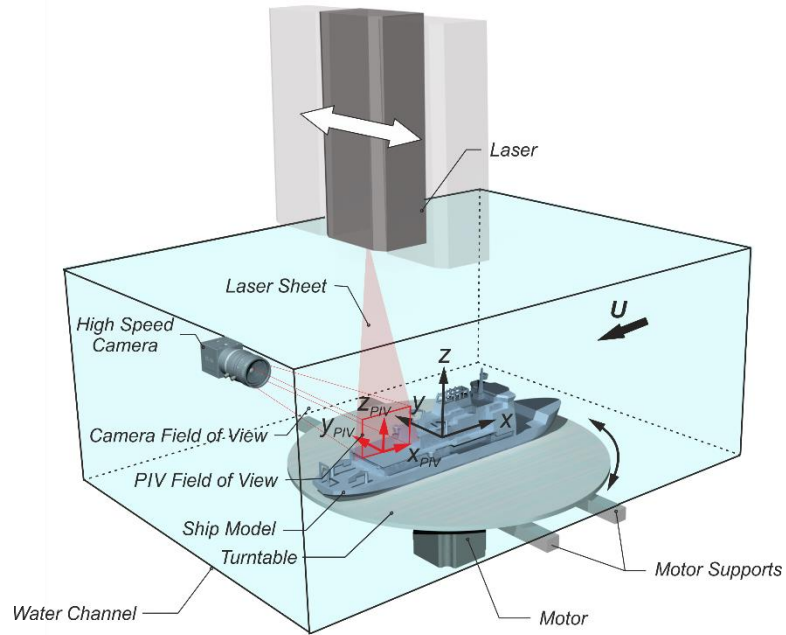


Fig. 3-1. Schematic of the experimental setup.

At the entrance to the test section, the flow passed over a series of vertical spires and surface roughness elements, which resulted in a boundary layer profile with the time-averaged and fluctuating velocity distributions corresponding to those of a typical atmospheric boundary layer (Counihan 1975; Zhou and Kareem 2002). The details of the flow conditioning system are provided in Rahimpour and Oshkai (2016). The desired boundary layer conditions were achieved 125 cm downstream of the entrance of the test section. The distribution of streamwise velocity component and turbulence intensity in the simulated ABL are shown in comparison to the size of the scaled model of the ship in Fig. 3-2. In Fig. 3-2 (a) the velocity distribution is compared with a power law velocity profile associate with open sea conditions (Counihan, 1975):

$$\frac{u}{u_\delta} = \left( \frac{z^*}{\delta} \right)^{0.13} . \quad (3-1)$$

Here,  $z^*$  is the vertical coordinate originating at the wall of the water tunnel,  $\delta$  is the boundary layer thickness,  $u_\delta$  is the horizontal velocity component at the edge of the boundary layer and  $H = 45$  cm is the height of the test section. Furthermore, in Fig. 3-2 (b) the streamwise turbulence intensity ( $I_u$ ) distribution is compared with a modified profile (Zhou and Kareem 2002), which could be written as:

$$\frac{I_u}{I_{u,\delta}} = \left( \frac{z^*}{\delta} \right)^{0.13}, \quad (3-2)$$

where  $I_{u,\delta}$  is the streamwise turbulence intensity at edge of boundary layer.

In the present study, following Rahimpour and Oshkai (2016), the characteristic flow velocity ( $U$ ) corresponds to the freestream velocity value at the entrance of the test section of the water tunnel. Moreover, the characteristic length ( $L$ ) is the beam of the ship.

In our earlier work (Rahimpour and Oshkai 2016), we concluded that the flow patterns in the wake of the superstructure were characterized by massively separated flow regions and were independent of the Reynolds number ( $Re = UL/\nu$ , where  $\nu$  is the kinematic viscosity of the fluid). In the present investigation, the inflow velocity condition resulted in the Reynolds number of  $Re = 61,000$ , which is shown to be sufficiently large to ensure the fluid dynamic similarity between the scaled model and the full-scale vessel (Rahimpour and Oshkai 2016).

### 3.2.2 Scaled model

The schematics of the scaled model are showed in Fig. 3-3. The inset schematic of Fig. 3-3 (d) also shows an arbitrary incidence angle of the inflow ( $\alpha$ ). Here, we define the angle of incidence as the angle between the inflow velocity vector and the centerline of the scaled model. Furthermore, in the present study, the rate of change in the inflow direction with respect the CCG icebreaker,  $\dot{\alpha}$ , is represented by the rotation of the scaled model. Hence, the clockwise and counter-clockwise rotation of the scaled model in the laboratory reference frame corresponded to the positive and the negative rates of change in the inflow

direction, respectively. For an arbitrary incidence angle  $\alpha$ , Fig. 3-3 (d) shows the inflow velocity, the coordinate system as well as  $\alpha$ .

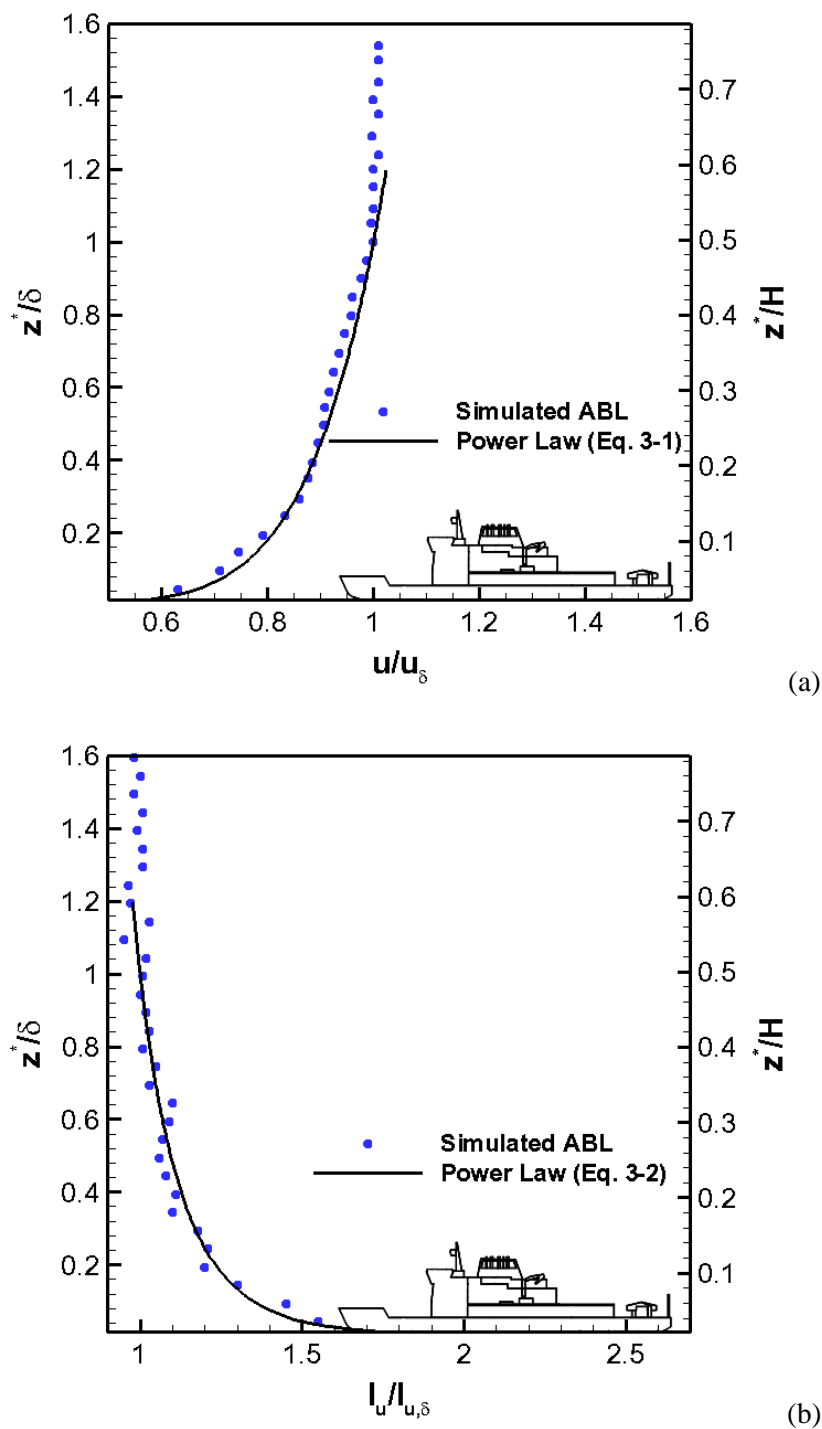
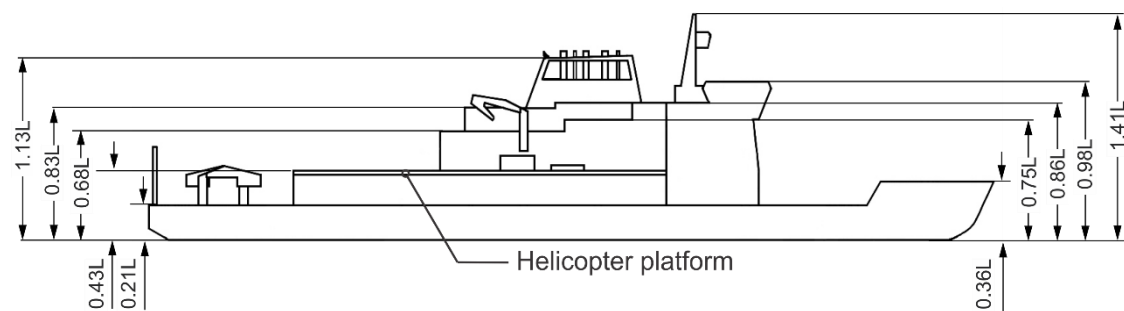
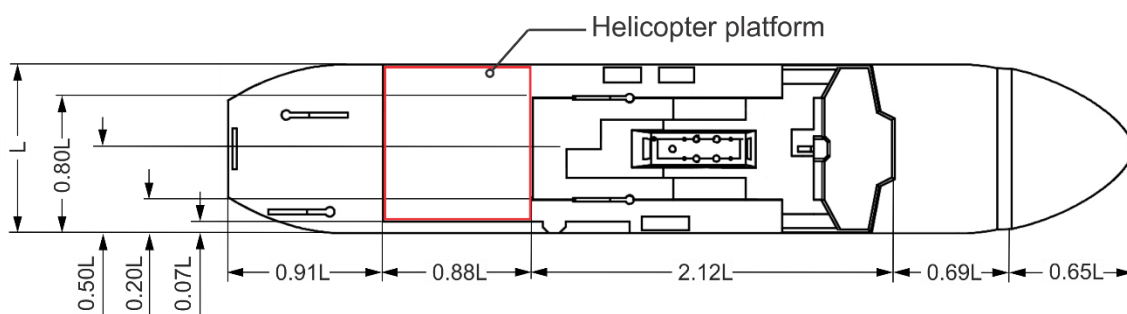


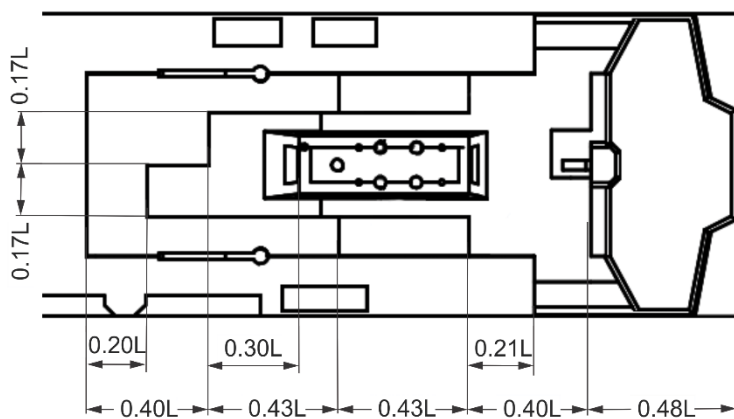
Fig. 3-2. Distribution of (a) time-averaged streamwise velocity component and (b) streamwise turbulence intensity in the simulated ABL.



(a)



(b)



(c)

Fig. 3-3. Schematics of the CCG icebreaker: (a) side view, (b) plan view, (c) closeup of the superstructure (d) definition of reference frame for the inflow incidence angle.

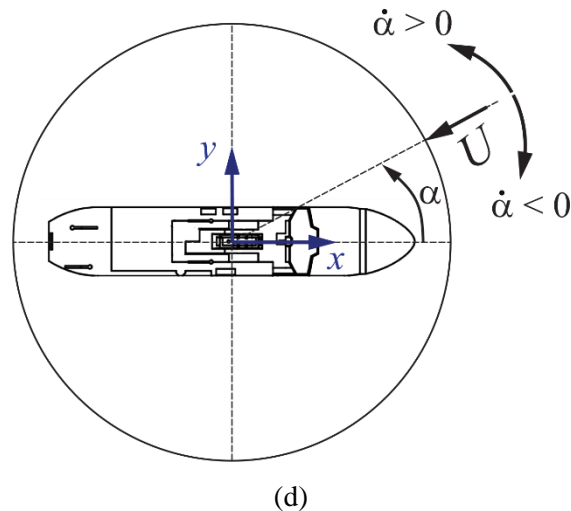


Fig. 3-3. Continued.

### 3.2.3 Quantitative flow imaging and phase-averaging

In the present study, the global, instantaneous velocity fields were obtained in several vertical data acquisition planes using high-speed particle image velocimetry (PIV). The PIV system included a Nd:YLF dual diode pulsed laser, with the power output of 25 mJ/pulse. Using a series of optical lenses, the laser beam was transformed into a planar light sheet, which had the thickness of 1.5 mm at the location of PIV field of view (Fig. 3-1). The flow in the water channel was seeded with the tracer particles (silver-coated hollow spheres) with the average diameter of 13  $\mu\text{m}$  and the density of 1.6 g/cc. The generated laser sheet illuminated the tracer particles, which were then photographed using a digital camera with a complementary metal oxide semiconductor (CMOS) sensor that contained 1024 x 1024 pixels. The camera was equipped with a lens with a focal length of 60 mm and a numerical aperture of f/2.8. The process of laser pulsing and image capture was synchronized using a computer equipped with a software for controlling the data acquisition (LaVision DaVis 7.2). The instantaneous velocity fields were then obtained by processing the PIV images, which included cross-correlating the patterns of tracer particles in consecutive images using LaVision DaVis 8.2 software (Rahimpour and Oshkai 2016; Raffel et al. 2007). The multi-pass algorithm involved interrogation windows with the initial size of 64 x 64 pixels, which were progressively refined to the final size of 16 x 16 pixels with 50% overlap between the adjacent windows in both vertical and horizontal

directions. Ultimately, in the present study, the acquired PIV data had the resolution of 0.604 vector/mm, which corresponded to 30 data points per characteristic length  $L$ . The PIV system is shown in Fig. 3-1, which also shows a PIV data acquisition coordinate system ( $x_{PIV}$ ,  $y_{PIV}$ ,  $z_{PIV}$ ) located at the center of the helicopter platform. The PIV coordinate system was fixed in the laboratory frame and did not rotate with the scaled model.

For different rates of change in the incidence angle, the obtained velocity fields were phase-averaged for incidence angles of  $0^\circ \leq \alpha \leq 330^\circ$  with the increment of  $30^\circ$ . The model of the ship was continuously rotated in the uniform inflow. Instantaneous velocity fields acquired at a specific orientation (phase) of the ship were ensemble-averaged to calculate the phase-averaged flow representations. For each considered incidence angle (phase), a minimum of 200 image pairs were acquired. In the current investigation, following Benedict and Gould (1996), the uncertainty associated with the sampling of a random process was evaluated. The maximum uncertainty for the phase-averaged velocity field and the associated turbulence intensity were less than 3% and 6% respectively, hence, the statistical convergence of the phase-averaged parameters was verified.

### 3.3 Results and discussion

#### 3.3.1 Effect of the rate of change of the incidence angle

Quantitative, time-averaged flow patterns above the helicopter platform were acquired for the range of the inflow incidence angles  $0^\circ \leq \alpha \leq 330^\circ$  at the interval of  $\Delta\alpha = 30^\circ$ . The lowest turbulence levels were found at  $\alpha = 180^\circ$ . This observation is expected, as the helicopter platform was directly exposed to the oncoming flow at that incidence angle, and the influence of the superstructure was minimal. This observation is in agreement with the results of Rahimpour and Oshkai (2016), where the lowest turbulence intensity was observed at  $\alpha = 180^\circ$ . The highest values of the turbulent intensity above the helicopter platform were observed at the inflow incidence angles  $\alpha = 0^\circ$  and  $\alpha = 60^\circ$ , for which the flow patterns are shown in Fig. 3-4 and Fig. 3-5, respectively. Different rates of change of the inflow direction, corresponding to clockwise and counter-clockwise rotation of the

scaled model with respect to the centerline of the ship (when viewed from the top), were considered and compared to the cases presented herein. At the inflow incidence angle  $\alpha = 0^\circ$ , the direction on the changing angle of incidence of the incoming flow did not have a significant effect on the time-averaged flow structure over the helicopter platform, so only the data corresponding to the positive rate of change in the inflow, i.e. clockwise rotation of the scaled model, is presented herein. On the other hand, different rates of change of the incident flow direction had a pronounced effect on the wake of the superstructure. Fig. 3-4 shows patterns of the non-dimensionalized time-averaged out-of-plane vorticity ( $\langle \omega_y \rangle L/U$ ) and time-averaged streamlines at  $\alpha = 0^\circ$  corresponding to four different dimensionless rates of change of the inflow incidence angle  $\dot{\alpha}L/U$ . The mean inflow direction in these plots and throughout the paper is from right to left, unless indicated otherwise.

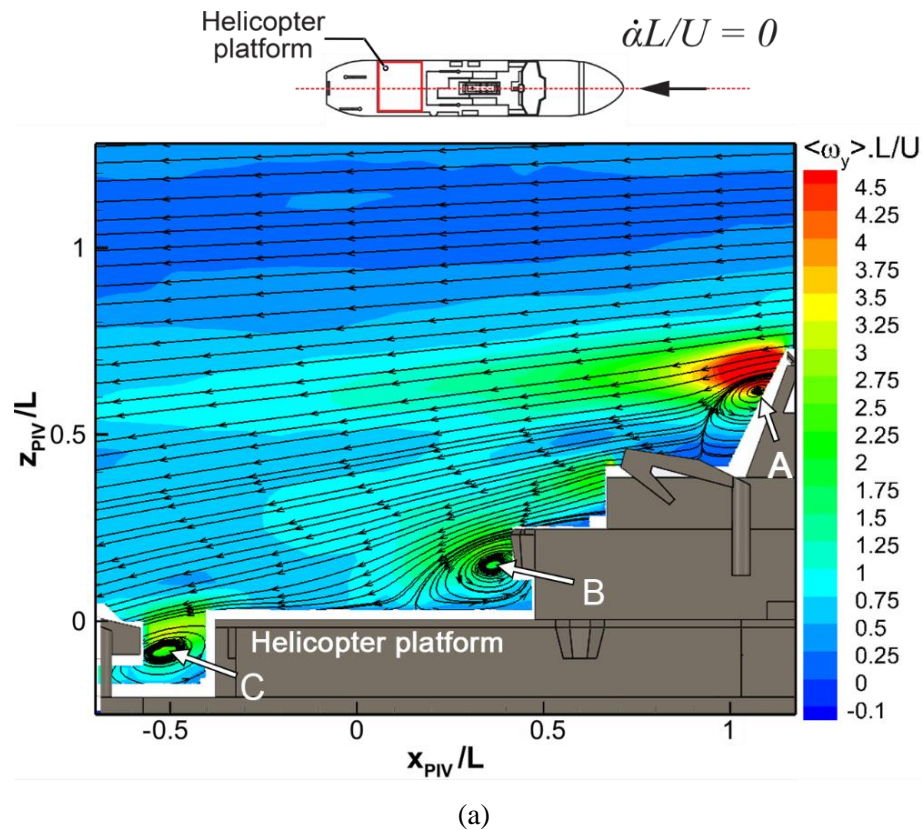
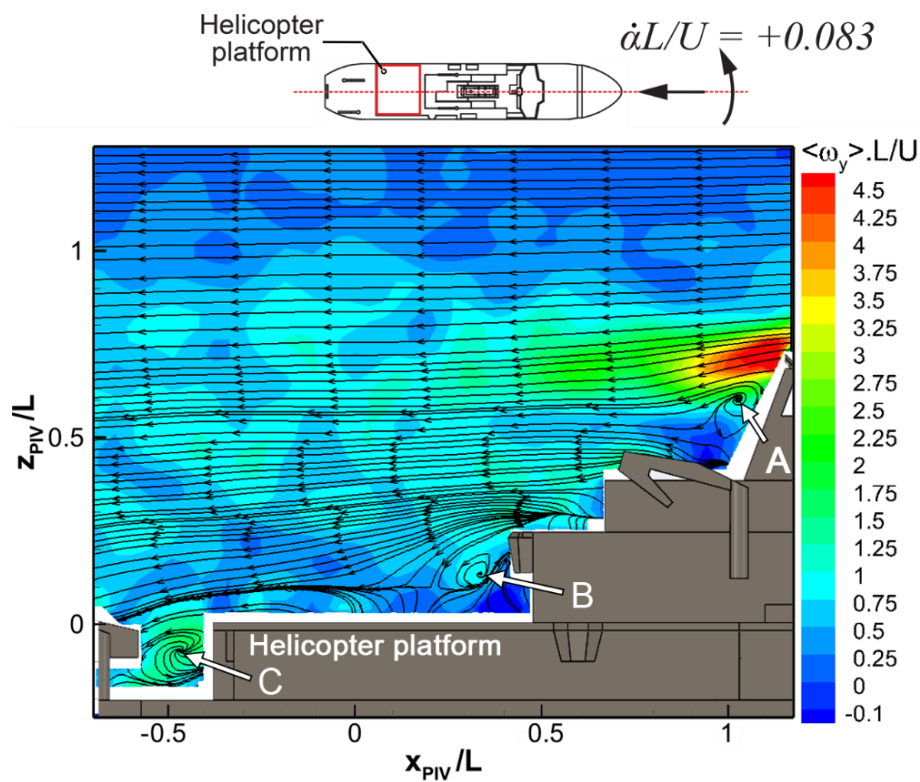
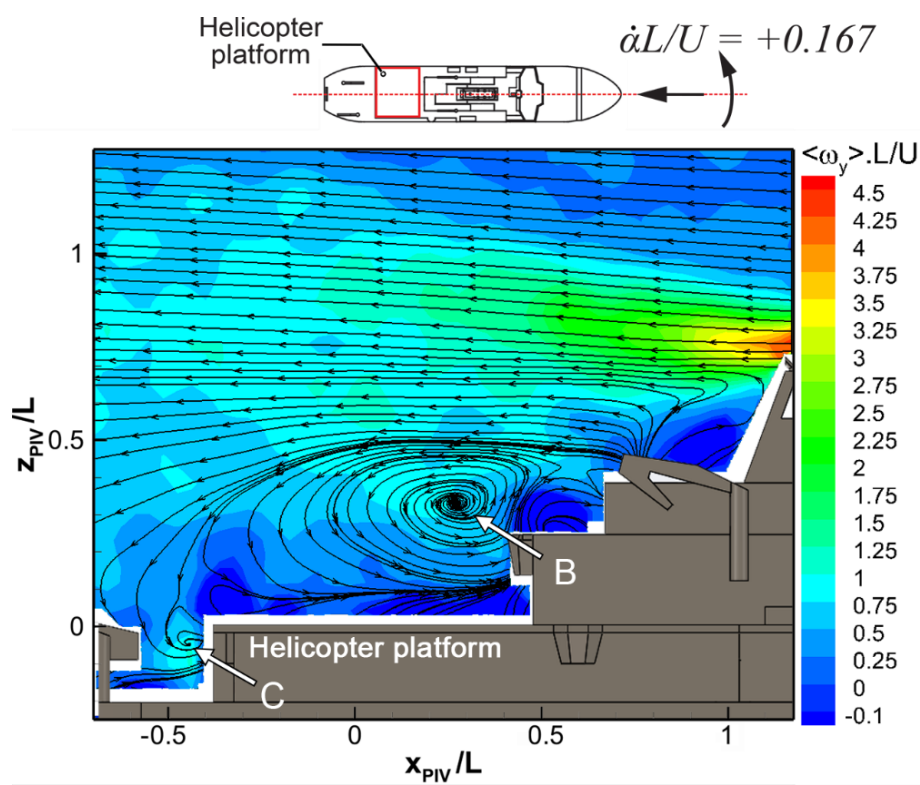


Fig. 3-4. Time-averaged streamlines and contours of out-of-plane vorticity at  $\alpha = 0^\circ$ , at  $y_{PIV} = 0$ :

(a)  $\dot{\alpha}L/U = 0$ , (b)  $\dot{\alpha}L/U = 0.083$ , (c)  $\dot{\alpha}L/U = 0.167$ , (d)  $\dot{\alpha}L/U = 0.25$ .



(b)



(c)

Fig. 3-4. Continued.

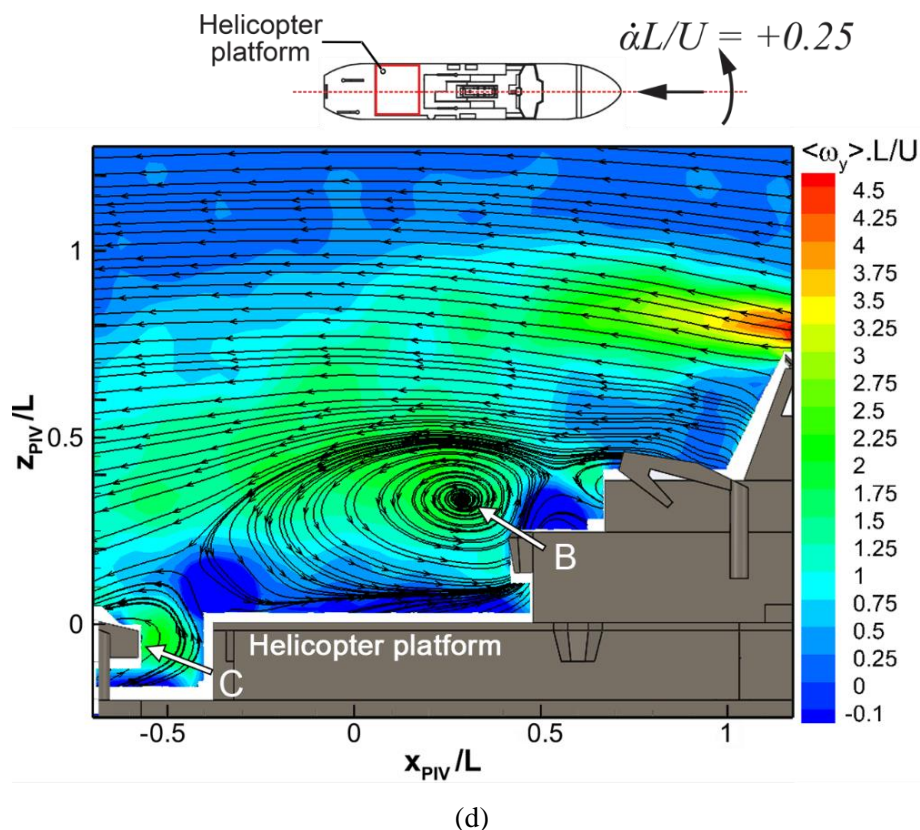


Fig. 3-4. Continued.

The reference case of  $\dot{\alpha}L/U = 0$ , shown in Fig. 3-4 (a), which corresponded to the constant incidence angle, resulted in the airwake structure that was characterized by three recirculation zones corresponding to flow separation from the top of the superstructure, the edge of the superstructure immediately upstream of the helicopter platform, and the downstream edge of the helicopter platform. These recirculation regions are labeled “A”, “B” and “C”, respectively, in Fig. 3-4 (a). These flow separation zones correspond to elevated levels of the out-of-plane vorticity in the shear layers that formed downstream of the points of flow separation. The peak vorticity was observed in the upper shear layer, immediately downstream of the top of the superstructure at  $z/L = 0.7$ . The upper shear layer was inclined downward, as the flow was deflected towards the lower pressure wake downstream of the superstructure. This flow direction is indicated by the pattern of time-averaged streamlines, which were inclined downward. The vortices A, B and C were relatively small-scale, and they were confined to the immediate vicinity of the flow

separation points. The shear layer corresponding to vortex B reattached to the helicopter platform at  $x/L = 0.35$ .

In the case when the inflow direction was changing with the rate of  $\dot{\alpha}L/U = 0.083$ , shown in Fig. 3-4 (b), the flow structure was qualitatively similar to the case of  $\dot{\alpha}L/U = 0$ . The flow separated from the top of the superstructure was still deflected downward, and the vortices A, B and C were still small-scale and confined to the vicinity of the separation points. However, the vorticity pattern shows higher levels of negative vorticity distributed throughout the wake, compared to the reference case of  $\dot{\alpha}L/U = 0$ . This increased unsteadiness of the wake is expected because of the added transient change in the inflow. Also, in the case of the changing inflow, the separated flow region extended over the entire helicopter platform. This change in the flow pattern occurred because the side edge of the helicopter platform was exposed to the oncoming flow as the inflow was undergoing the change in direction.

The increase of the rate of change of the inflow direction to  $\dot{\alpha}L/U = 0.167$  resulted in a significant change in the flow structure, as shown in Fig. 3-4 (c). Vortex A was no longer visible in the vicinity of the top downstream corner of the superstructure. The wake was dominated by a large-scale flow recirculation zone B located over the helicopter platform. The streamline pattern shown in Fig. 3-4 (c) shows that the flow, which separated from the superstructure at  $z/L = 0.40$ , did not reattach to the helicopter platform. Instead, the flow reattached to the vertical surface downstream of the platform. This massive flow recirculation zone resulted in the local flow in the negative  $x$ -direction in the immediate vicinity of the surface of the helicopter platform. The presence of the massive flow recirculation zone B also resulted in an upward injection of the fluid into the freestream downstream of the separation point ( $x/L = 0.35$ ), which caused an upward deflection of the flow that separated from the top of the superstructure. Moreover, the peak positive vorticity was located farther upstream, at  $x/L = -0.75$ , and directly over the top of the superstructure.

As the rate of change of the inflow direction increased to  $\dot{\alpha}L/U = 0.25$ , the strength of the vortex B increased, as indicated by the higher levels of positive out-of-plane vorticity

distributed over the helicopter platform in Fig. 3-4 (d). The recirculation zone C located immediately downstream of the helicopter platform also increased both in the spatial extent and in the levels of the associated positive vorticity. Vortex A was not visible, but the shear layer that separated from the top of the superstructure exhibited higher levels of vorticity, which extended farther downstream, compared to the case of  $\dot{\alpha}L/U = 0.167$ .

Fig. 3-5 shows patterns of the non-dimensionalized time-averaged out-of-plane vorticity ( $\langle \omega_y \rangle L/U$ ) and the time-averaged streamlines at the inflow incidence angle  $\alpha = 60^\circ$  corresponding to different dimensionless rates of change of the inflow incidence angle  $\dot{\alpha}L/U$ . In addition to the reference case of  $\dot{\alpha}L/U = 0$ , three different rates of change were considered in both clockwise and counter-clockwise directions:  $\dot{\alpha}L/U = \pm 0.083$ ,  $\dot{\alpha}L/U = \pm 0.167$  and  $\dot{\alpha}L/U = \pm 0.25$ .

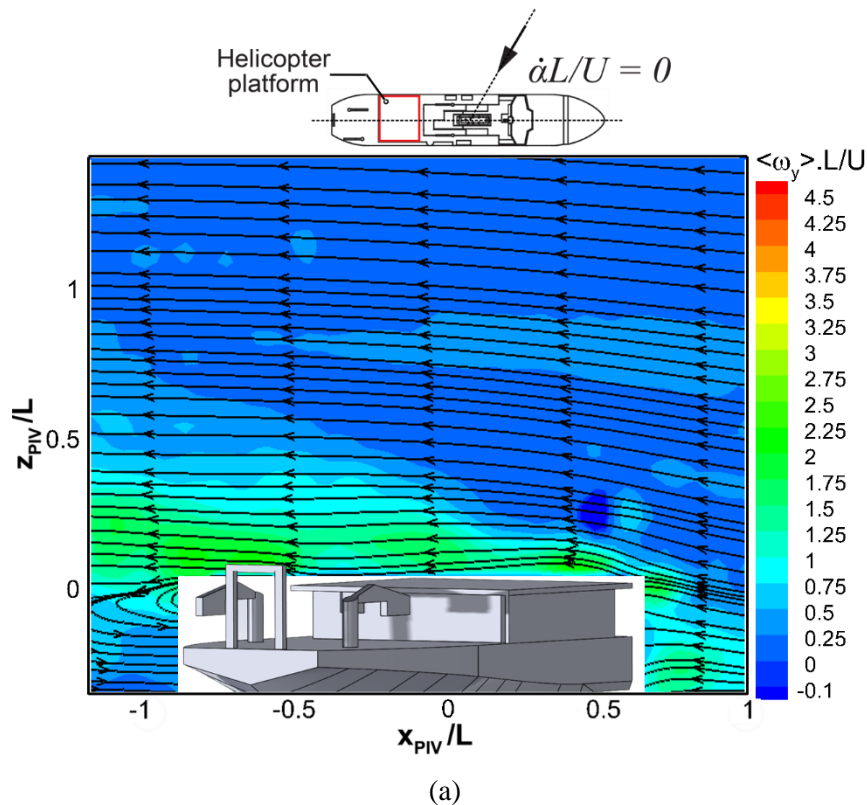
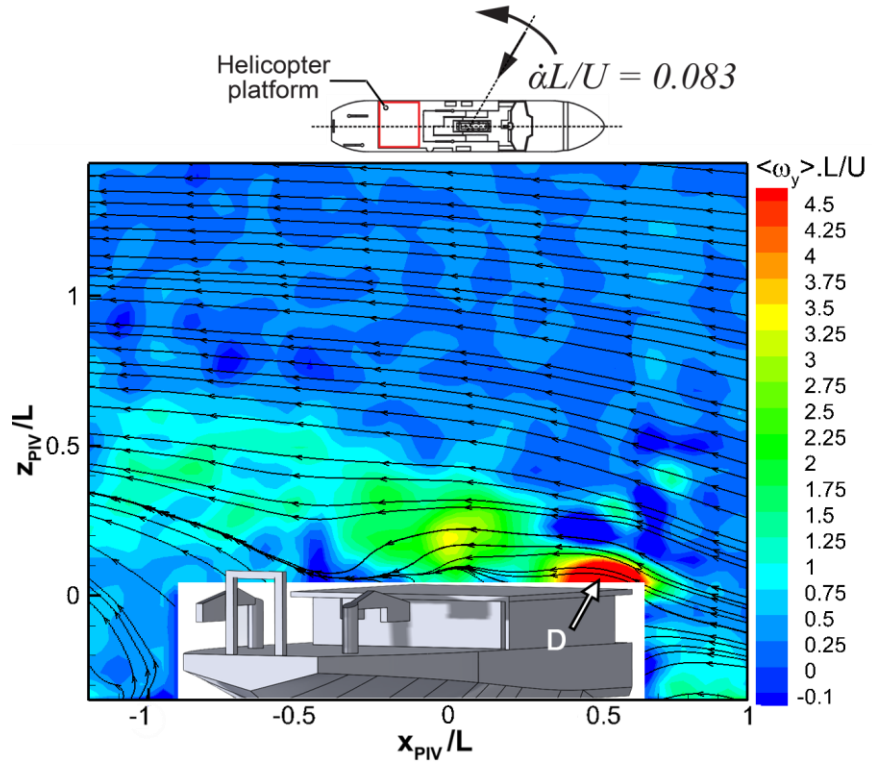


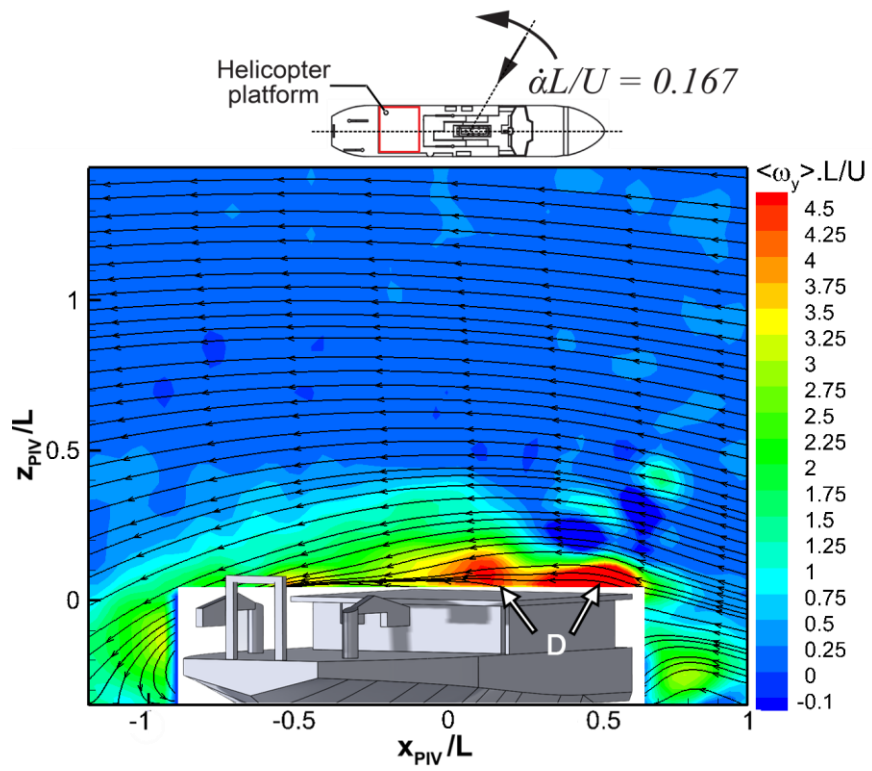
Fig. 3-5. Time-averaged streamlines and contours of out-of-plane vorticity at  $\alpha = 60^\circ$ , at  $y_{PIV} = 0$ :

(a)  $\dot{\alpha}L/U = 0$ , (b)  $\dot{\alpha}L/U = 0.083$ , (c)  $\dot{\alpha}L/U = 0.167$ , (d)  $\dot{\alpha}L/U = 0.25$ , (e)  $\dot{\alpha}L/U = -0.167$ , (f)

$\dot{\alpha}L/U = -0.25$ .



(b)



(c)

Fig. 3-5. Continued.

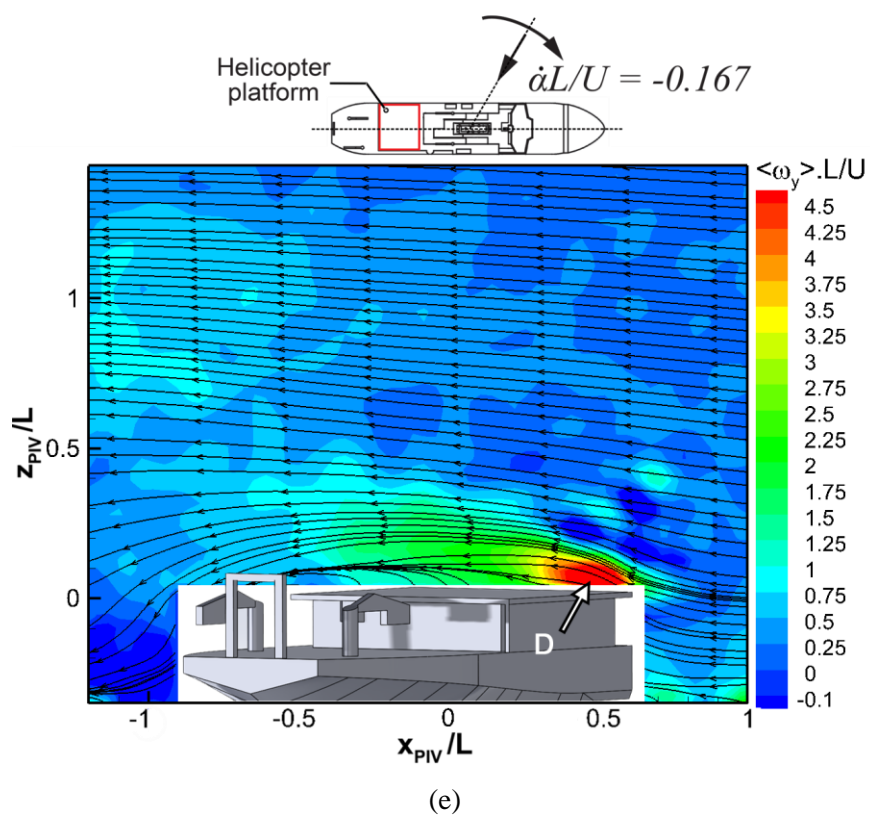
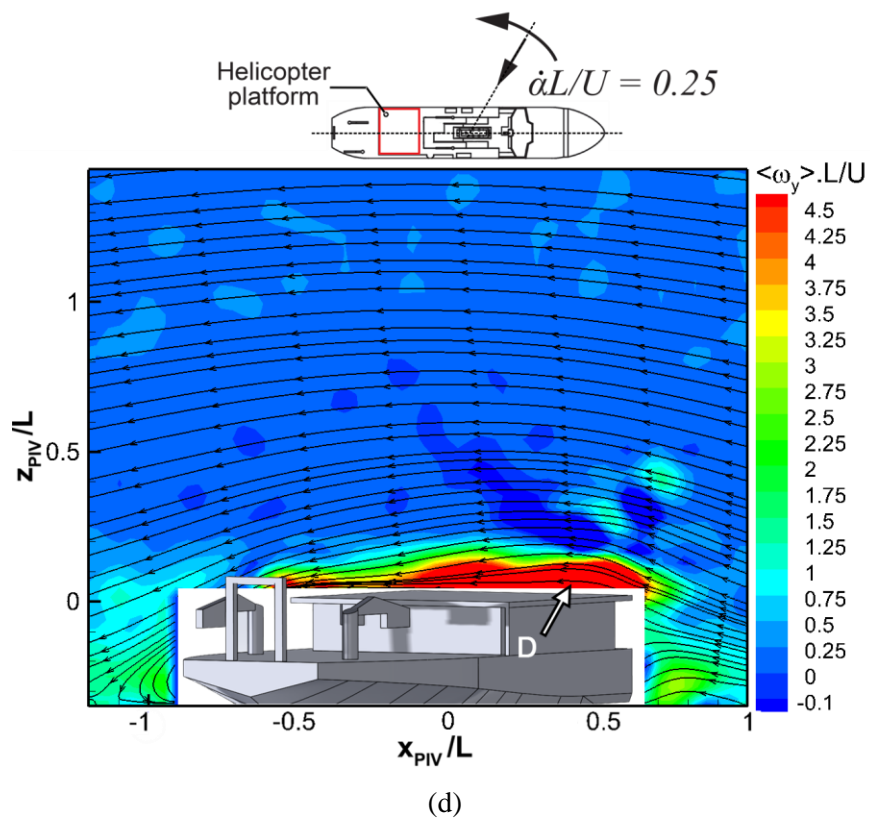


Fig. 3-5. Continued.

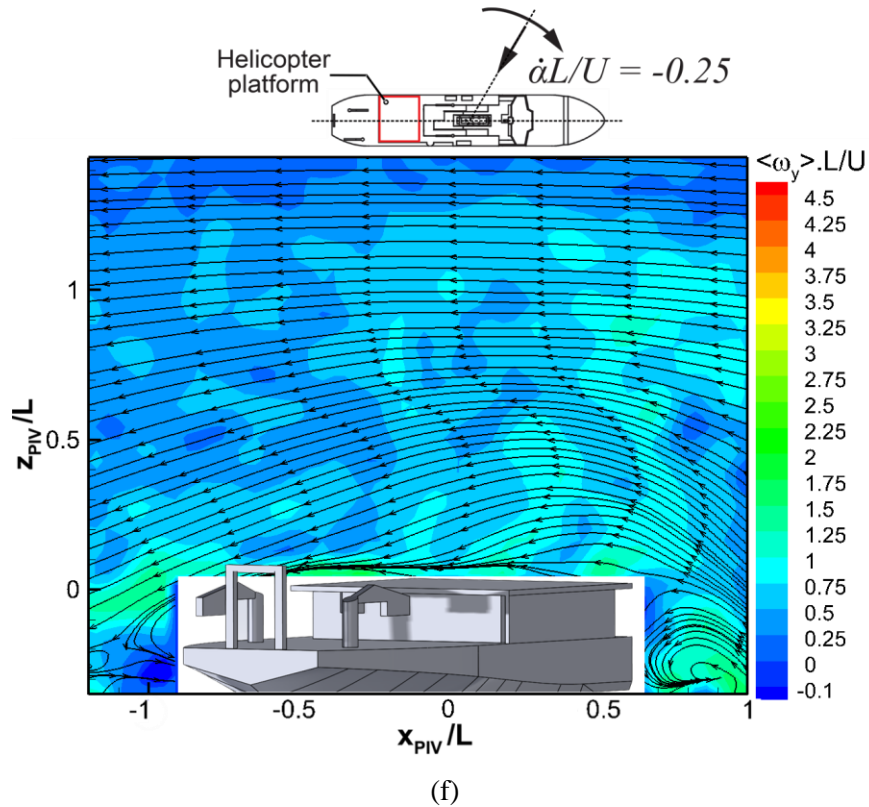


Fig. 3-5. Continued.

The sequence of the plots in Fig. 3-5 (a) – 5(d) illustrates the effect of the increased rate of change of the inflow direction (from  $\dot{\alpha}L/U = 0$  to  $\dot{\alpha}L/U = 0.25$ ), when the ship rotated in the clockwise direction relative to the inflow, when viewed from above. The flow patterns corresponding to  $\dot{\alpha}L/U = -0.083$  were substantially similar to those corresponding to  $\dot{\alpha}L/U = 0.083$ , therefore only the latter case is presented herein. In contrast, for the higher rates of change,  $\dot{\alpha}L/U = \pm 0.167$  and  $\dot{\alpha}L/U = \pm 0.25$ , the direction of change had a pronounced effect on the flow structure above the helicopter platform. In particular, comparison of the vorticity plots of Fig. 3-5 (c) ( $\dot{\alpha}L/U = 0.167$ ) and Fig. 3-5 (e) ( $\dot{\alpha}L/U = -0.167$ ) reveals that in the former case, corresponding to the clockwise rotation of the ship, the elevated levels of vorticity were observed over larger area in  $y = 0$  plane. Moreover, two distinct concentrations of positive vorticity were located immediately above the helicopter platform. In the case of the counter-clockwise ship rotation, shown in Fig. 3-5 (e), a single positive vortex was confined to the right-hand side of the flow field above the

platform. This trend was even more pronounced as the rate of change was increased to  $\dot{\alpha}L/U = \pm 0.25$  (Fig. 3-5 (d) and Fig. 3-5 (e)).

This pronounced difference in the flow patterns was due to the asymmetry of the ship superstructure encountered by the oncoming flow. Specifically, as the ship was rotated clockwise with respect to the inflow (coming nominally at  $\alpha = 60^\circ$ ), the helicopter platform became progressively enclosed in the wake of the superstructure. In contrast, when the ship model was rotated in the counter-clockwise direction (negative  $\dot{\alpha}L/U$ ), the helicopter platform was directly exposed to the oncoming flow and relatively unaffected by the superstructure.

In addition to considering the streamline patterns and the distributions of vorticity, we calculated the turbulence intensity of the flow by dividing the standard deviation of the velocity components ( $\sigma_u$  and  $\sigma_w$ , respectively, for the streamwise and the vertical components of velocity) by the characteristic velocity:  $I_u = \sigma_u/U$ ,  $I_w = \sigma_w/U$ . The standard deviation of velocity was defined as follows:

$$\sigma_i = \sqrt{\frac{\sum_1^N (u_i - \langle u_i \rangle)^2}{N-1}}, \quad (3-3)$$

where  $N$  is the total number of acquired PIV image pairs for each incidence angle (i.e. phase).

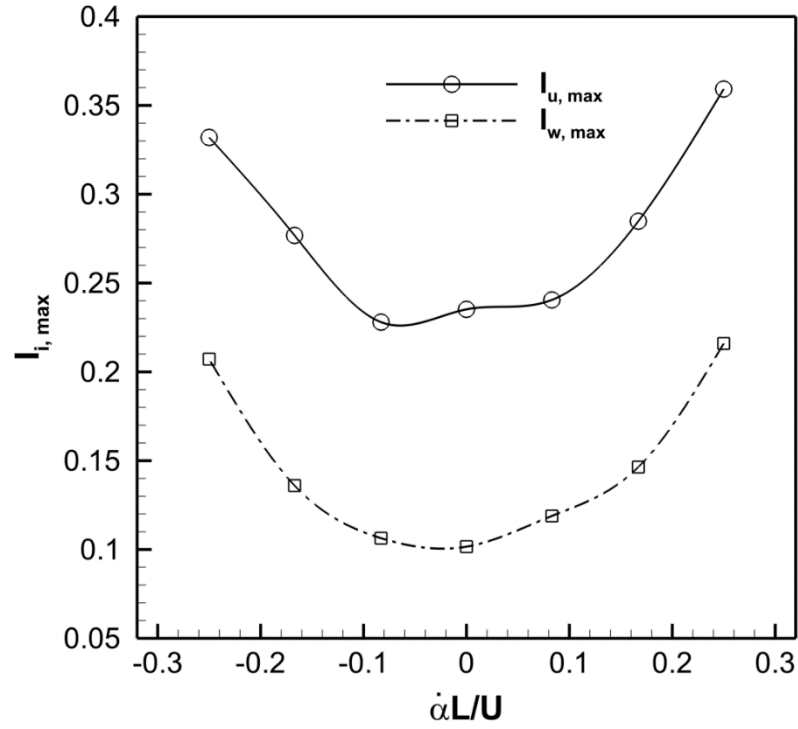
Increasing the magnitude of rates of change of the inflow direction  $|\dot{\alpha}L/U|$  at  $\alpha = 0^\circ$  resulted in an increase of the maximum values of the turbulent intensity over the helicopter platform, as shown in Fig. 3-6 (a). Both the clockwise and the counterclockwise change in the inflow direction produced an increase of the maximum turbulent intensity values. For all values of  $\dot{\alpha}L/U$ , the maximum turbulent intensities associated with the x-component of the velocity field,  $I_{u, max}$ , were higher than the corresponding values associated with the vertical (z-direction) component of the velocity,  $I_{w, max}$ . This trend is expected, as the contributions to  $I_{u, max}$  included the turbulence associated with the transient change of the

inflow, which was imposed in the horizontal plane. Moreover, the horizontal rotation of the ship relative to the inflow at the nominal incidence angle of  $\alpha = 0^\circ$  exposed the sides of the superstructure to oblique inflow, which in turn resulted in vortex shedding from the sides of the superstructure. These additional vortices in the wake contributed primarily to the velocity fluctuations in the horizontal plane (parallel to the helicopter platform).

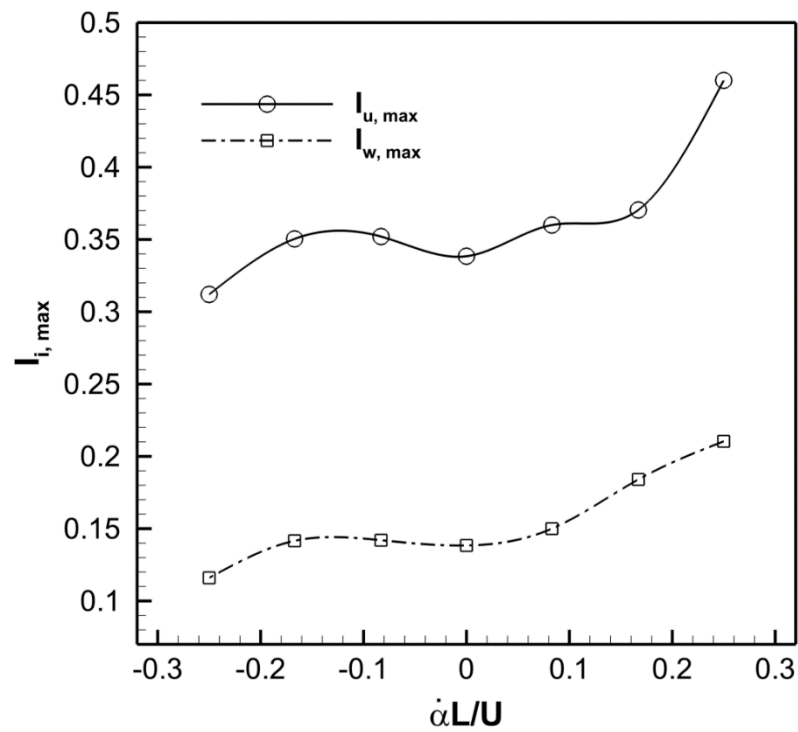
Variation of the maximum values of the turbulent intensity as the inflow direction was dynamically changed from the nominal value of  $\alpha = 60^\circ$  is shown in Fig. 3-6 (b). Similar to the case of  $\alpha = 0^\circ$  (Fig. 3-6 (a)), the maximum turbulent intensity values  $I_{u, max}$  and  $I_{w, max}$  exhibited a similar trend, while the values of  $I_{u, max}$  were substantially higher than those of  $I_{w, max}$  for all considered rates of change of the inflow direction.

In contrast to the case of  $\alpha = 0^\circ$ , in the case of  $\alpha = 60^\circ$  (Fig. 3-6 (b)), the values of the maximum turbulent intensity showed strong dependence on the direction of the ship rotation relative to the inflow. This observation is consistent with the change in the flow patterns as the function of the rate of change of the inflow direction that is illustrated in Fig. 3-5. Specifically, due to the asymmetry of the ship's superstructure, at negative values of  $\dot{\alpha}L/U$ , corresponding to clockwise rotation of the ship model, the area above the helicopter platform was less affected by wake of the superstructure.

The plots of Fig. 3-7 show variation of the turbulent intensity at the center of the helicopter platform as the function of the rate of change of the inflow direction from  $\alpha = 0^\circ$  at two elevations above the platform,  $z/L = 0.25$  and  $z/L = 0.40$ . The turbulent intensity  $I_u$  increased for both directions of the ship rotation with respect to the inflow, as shown in Fig. 3-7 (a). The turbulent fluctuations in the z-direction,  $I_w$ , initially decreased and then grew more rapidly at the ship model was rotated clockwise with respect to the inflow, which corresponds to positive values of  $\dot{\alpha}L/U$  in Fig. 3-7 (b). Moreover, the turbulent intensities at the higher elevation above the platform were generally higher than those at the lower elevations, because the point  $z/L = 0.40$  was located close to the centroid of the dominant vortical structure B shown in Fig. 3-4.

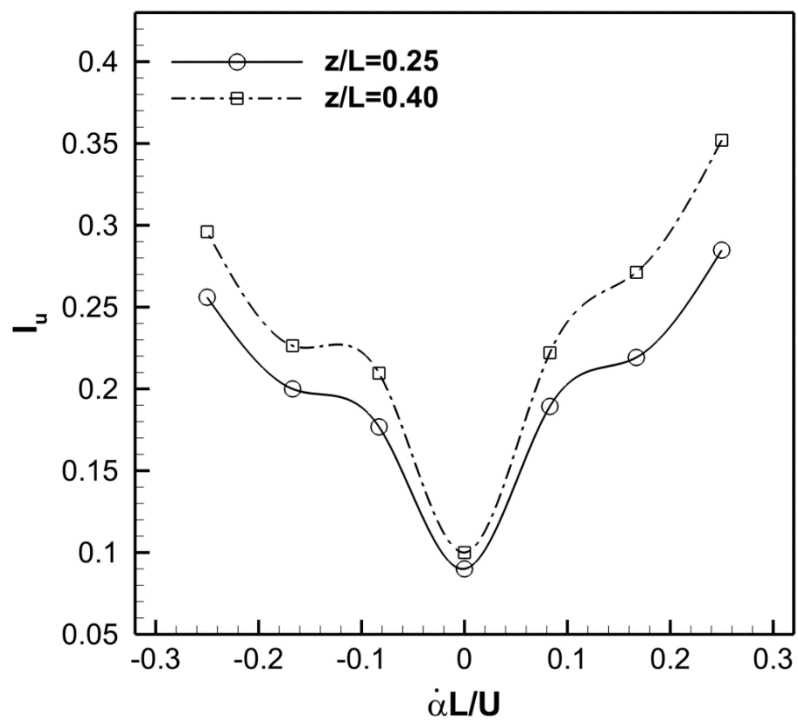


(a)

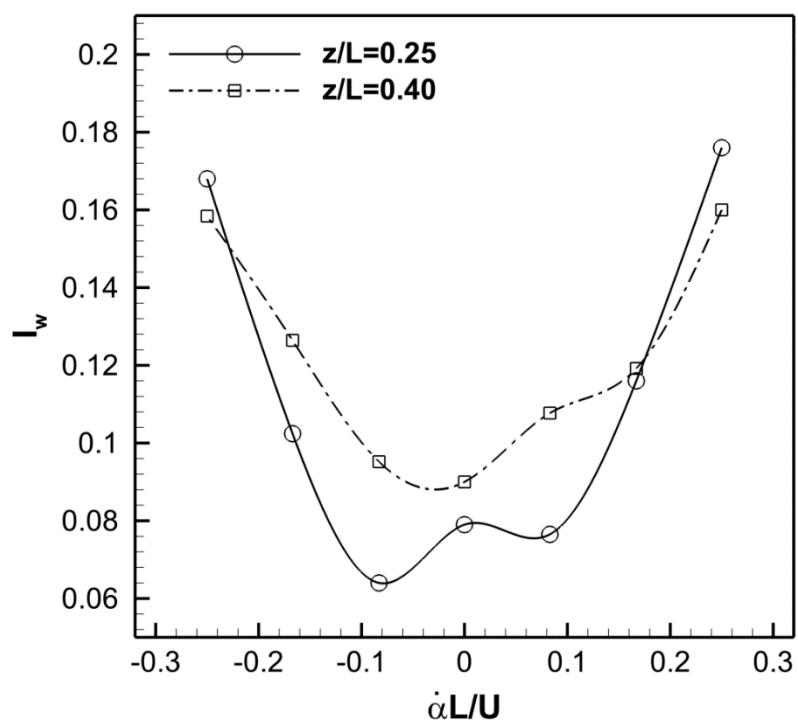


(b)

Fig. 3-6. Maximum values of turbulence intensity  $I_u$  and  $I_w$ , as a function of the rate of change of the incident flow direction at: (a)  $\alpha = 0^\circ$  and (b)  $\alpha = 60^\circ$ .

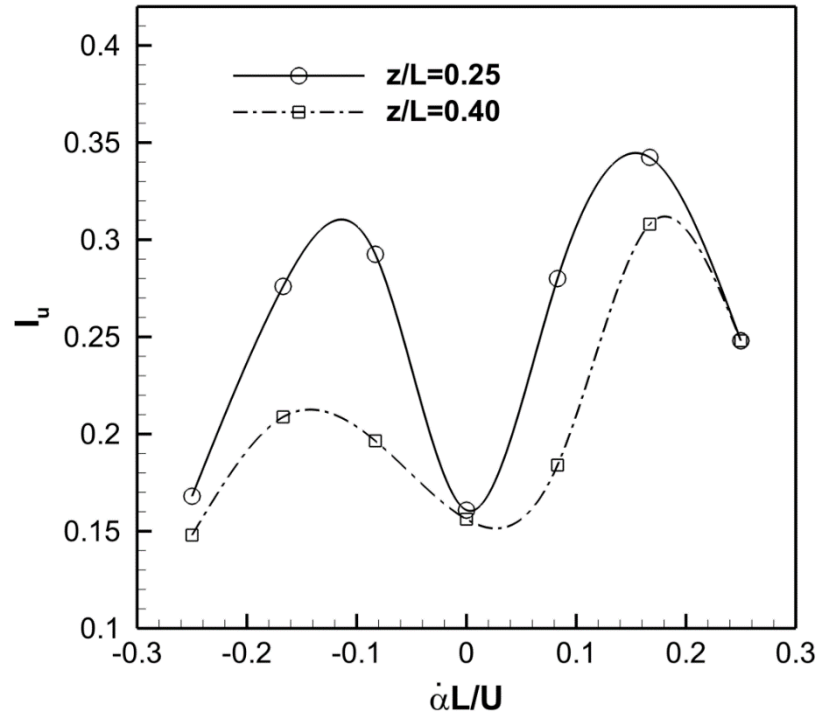


(a)

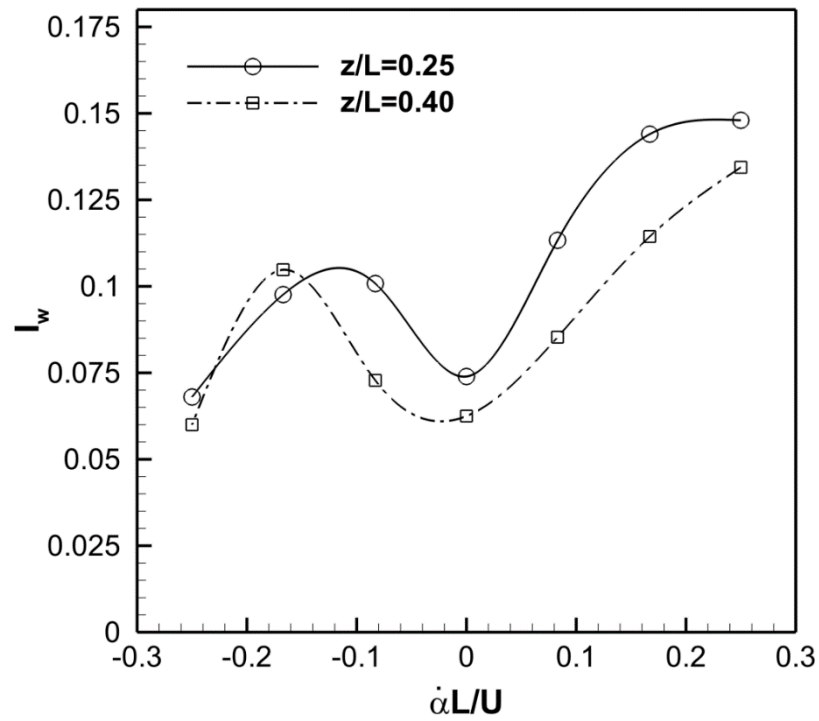


(b)

Fig. 3-7. Variation of turbulence intensities:  $I_u$  (a) and  $I_w$  (b) at the center of the helicopter platform, as a function of the rate of change of the incident flow direction at  $\alpha = 0^\circ$ .



(a)



(b)

Fig. 3-8. Variation of turbulence intensities:  $I_u$  (a) and  $I_w$  (b) at the center of the helicopter platform, as a function of the rate of change of the incident flow direction at  $\alpha = 60^\circ$ .

When the inflow was approaching from  $\alpha = 60^\circ$ , the measured turbulent intensities depended on the direction of the ship rotation, as shown in Fig. 3-8. The trends of the turbulent intensities at the center of the helicopter platform were qualitatively similar to those of the maximum turbulent intensities over the entire platform, which are shown in Fig. 3-6. The exception to this trend was observed at the highest considered positive rate of rotation,  $\dot{\alpha}L/U = 0.25$ , which resulted in the shift of the dominant recirculation cell away from the center of the helicopter platform. The turbulent velocity fluctuations in the case of  $\alpha = 60^\circ$  were primarily associated with the vorticity concentration  $D$ , which is shown in Fig. 3-5, which was located immediately above the surface of the platform. Thus, the measured turbulent intensities plotted in Fig. 3-8 decreased with the elevation above the platform.

### 3.4 Conclusions

We applied PIV in scaled model experiments to investigate the effects of transient changes in the inflow direction on the structure of the unsteady flow over the helicopter landing platform of a polar icebreaker. The flow above the landing platform contained recirculating vortical cells that resulted from flow separation from the top and the sides of the superstructure. The spatial extent of the separated flow regions and the associated vorticity levels increased as the rates of transient change in direction increased. It should be noted that the flow in the wake of the superstructure was highly three-dimensional, as detailed in our earlier study (Rahimpour and Oshkai 2016). Therefore, the present data, acquired in a 2D plane, needs to be interpreted with taking the 3D effects into account.

In general, increasing the rate of change of the inflow direction resulted in an increase of the turbulent intensity. However, as the flow over the helicopter landing platform was dominated by the wake of the asymmetric superstructure, the effect depended on the nominal direction of the inflow. In particular, when the inflow was coming from  $\alpha = 60^\circ$ , clockwise rotation of the ship model with respect to the inflow exposed the helicopter

platform to increased turbulent velocity fluctuations, while counterclockwise rotation diminished the flow unsteadiness over the helicopter platform.

## **4 Flow-induced loading on and unsteady flow structure in the wake of bluff perforated plates at zero incidence**

### **Preamble**

The body of this chapter has been published as: Mostafa Rahimpour, Filippo Carlo Bossi, Oleksandr Barannyk, Stefano Malavasi, Peter Oshkai, 2018. Flow-induced loading on and unsteady flow structure in the wake of bluff perforated plates at zero incidence, *Journal of Fluids and Structures*, 81, 712-727.

DOI: /10.1016/j.jfluidstructs.2018.06.007.

Explicit permission to reprint the material, as detailed above, in the present dissertation is granted by Elsevier, as the publisher of *Journal of Fluids and Structures*.

Contributions: M. Rahimpour post-processed the data, performed the analysis, prepared the initial manuscript and contributed to the design of the experimental system, conducting the measurements and collecting the data. F.C. Bossi designed the experimental system and collected the data and contributed to the development of the manuscripts. O. Barannyk contributed to the design of experimental system, conducting the measurements and development of the manuscripts. S. Malavasi and P. Oshkai supervised the research, provided insight and contributed to the development of manuscript drafts.

## Abstract

Flow over rectangular plates positioned at zero incidence can result in high-amplitude forces on the plates. In this study, we apply particle image velocimetry (PIV) and direct force measurements to investigate the effect of transverse perforations on the flow-induced loading on and the flow structure in the near-wake of the plates. We compare plates with different characteristic diameter of the perforations, as well as a reference configuration without perforations, in terms of the spectra of the flow-induced forces, frequencies of the trailing-edge vortex shedding and boundary layer profiles at the trailing edge at different planes across the perforation patterns for a range of inflow velocities. The three-dimensionality of the near-wake of the perforated plate is related to the proximity of the individual perforations to the trailing edge of the plate. In the vicinity of the perforations, transverse oscillations of the flow velocity in the wake become suppressed as the diameter of the perforations increases.

**Keywords:** Perforated plate; flow-induced loading; near-wake structure; PIV.

## 4.1 Introduction

Rectangular plates aligned with the incoming fluid flow are common in various engineering systems. Despite the substantial amount of literature that exists on this topic, some important fluid-dynamic aspects remain unresolved. The reason for this situation is the fact that in many applications the effects of fluid-dynamic loading, vibrations and noise are often considered separately.

On one hand, the fundamental studies on the fluid-structure interactions (FSI) of stationary, solid plates at zero incidence provided framework for understanding of the sources of the flow-induced excitations. These studies, including those by Parker (1966), Nakamura and Nakashima (1986), Naudascher and Rockwell (1994) and Nakamura et al. (1996) characterized the FSI by the predominant frequencies of the flow and/or structure oscillations  $f$ , which is often presented as the Strouhal number  $St = fL/U$ , where  $L$  is the characteristic length and  $U$  is the characteristic flow velocity. Many studies to date

examined the effects of the Reynolds number (Okajima, 1982), chord-to-thickness ratio of the plate (Nakamura et al., 1991), array configurations (Guillaume and LaRue, 2001; Parker, 1966) and wall confinement (Guillaume and LaRue, 2005; Malavasi and Guadagnini, 2007; Malavasi and Zappa, 2009; Negri et al., 2011; Arslan et al., 2013) on the force coefficients and the Strouhal number. It has been established that the flow structure around bluff rectangular plates can be broadly classified based on the flow separation from the leading edge of the plate and subsequent reattachment, or lack thereof, to the surface of the plate or to the trailing edge. These flow regimes depend on the chord-to-thickness ratio of the plate (Nakamura et al., 1991). In the present case, the long plate configurations were considered, which resulted in the flow reattachment well upstream of the trailing edge.

On the other hand, effects of elasticity and porosity of a semi-infinite plate interacting with a turbulent eddy on radiated acoustic noise were investigated theoretically, using the Weiner-Hopf technique, by Jaworski and Peake (2013), and the related experimental measurements of the fluctuating pressure due to flow over a porous surface with flexible bristles were performed by Clark et al. (2014). Moreover, flow-acoustic resonance received significant attention over the years (Parker, 1966; Parker and Welsh, 1983; Welsh et al., 1984, Howe, 1986; Howe, 1997a; Howe, 1997b; Oshkai and Velikorodny, 2013; Bossi and Malavasi, 2014) as the dominant mechanism for generating unsteady pressure and velocity pulsations in engineering applications, such as splitter plates in pipelines.

In the present work, we have considered dynamic and kinematics measurements to provide answers to some of the open questions about the effects of transverse perforations on the fluid structure and the fluid loading on a long rectangular plate at zero incident. The work builds upon the results presented in recent papers (Bossi et al. 2017a; Bossi et al. 2017b) where, through force measurements, we describe the dynamic effects of perforation in terms of loading and its frequencies. Here, we complement the previous experiments by coupling the force measurements with flow velocity measurements using PIV to better understand the effects of the perforations on the boundary layer and to relate the local effect of the individual perforations on the frequency and the magnitude of the velocity fluctuations in the near-wake. To do this, we consider an experimental system, in which

the vortex shedding frequencies were clearly separated from those of the available acoustic modes. Thus, the unsteady loading on the plate was due to purely hydrodynamic effects. The dynamic and kinematic observations allow us to provide insight into the physical origin of the flow-induced loading on perforated plates. Moreover, we describe the relationship between the staggered perforation patterns and the structure of the resulting wake.

## 4.2 Experimental systems and techniques

### 4.2.1 Flow facility

The experiments were conducted in a flow visualization water channel at the University of Victoria. The flow was conditioned using five fine mesh screens and a polycarbonate honeycomb section with round cells with the diameter of 4 mm. A converging section with a contraction area ratio of 6:1 was located upstream of the test section. This configuration resulted in the inflow velocity  $U$  ranging from 0.20 m/s to 0.55 m/s, with the turbulence intensities less than 1%. The test section had a square cross-section of 45 cm x 45 cm and a length of 250 cm.

The flat plate was positioned parallel to the flow, in the middle of the test section to avoid interference between the wake of the plate and the walls. The plate was cantilevered at the top edge and attached to the frame of the water channel by a support structure that incorporated a load cell for direct force measurements, as shown in Fig. 4-1. The free end of the plate was located 2.5 mm away from the bottom of the test section to minimize the effects of flow separation from the free edge. In the present study, the end effects were neglected, since the plate did not undergo significant motion, with the exception of a single case, in which the amplitude of the oscillations of the free end did not exceed 1 mm. For all the cases considered herein, the water depth  $W$  was equal to 41.5 cm, so that the free-surface level coincided with the edge of the clamp, as shown in Fig. 4-2.

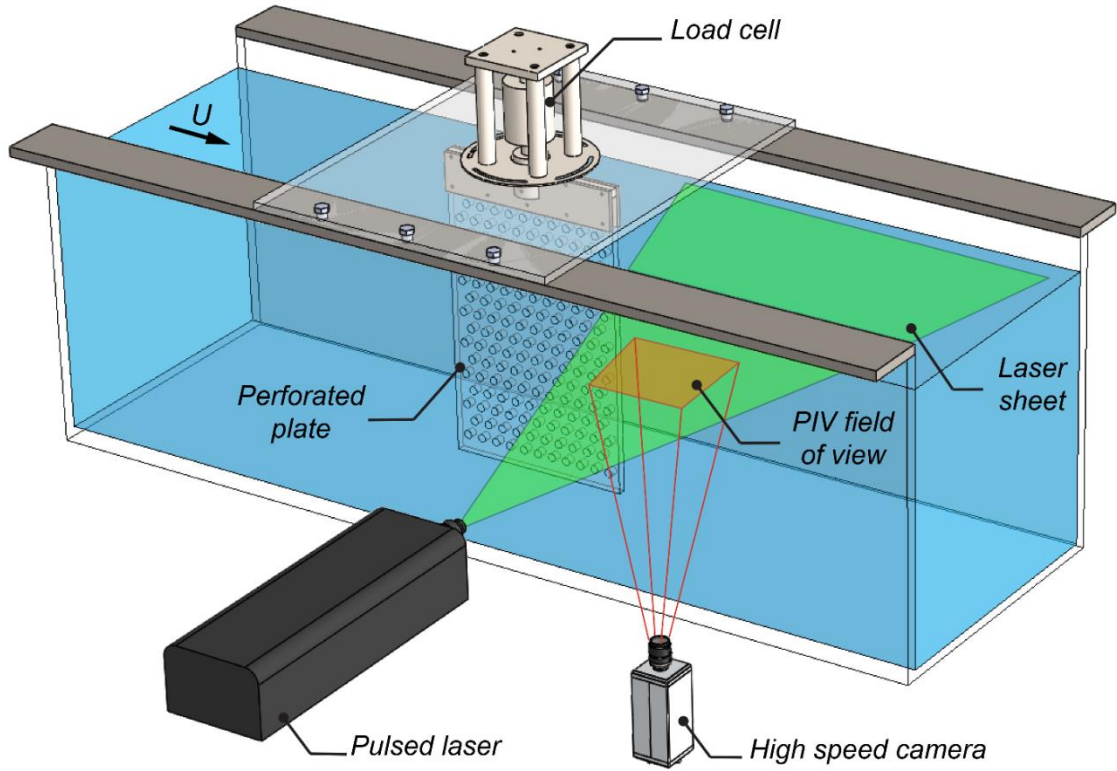


Fig. 4-1. Schematic of the experimental system.

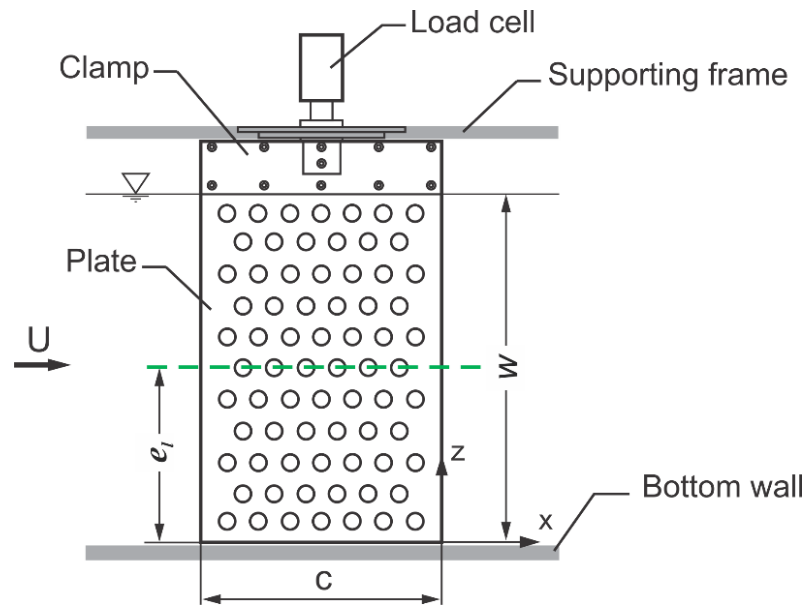


Fig. 4-2. Schematic of the perforated plate.

### 4.2.2 Perforated plates

Three plates with transverse perforations were considered, in addition to a reference plate with no perforations, which is referred to as pattern P0. The three perforation patterns had the same staggered arrangement, as shown in Fig. 4-3 , but had different perforation diameters  $\delta_h = 9.4$  mm, 12.7 mm, 19.5 mm, referred to as patterns P1, P2 and P3, respectively. The spacing between the perforations was also equal to  $\delta_h$ , so that all three plates had the same equivalent area ratio,  $\beta = (nA_p/A_t)^{0.5} = 0.4$ , where  $n$  is the number of perforations,  $A_p$  is the area of a single perforation,  $A_t$  is the total wetted area of the plate. The thickness of the plates P0, P1 and P2 was  $t = 12.5$  mm and P3 had a thickness of  $t = 12.3$  mm. All plates had a chord length  $c = 292.1$  mm. The plates were made of clear polycarbonate plastic sheet, with the density and the moduli of elasticity and rigidity of  $\rho = 1245.6$  kg/m<sup>3</sup>,  $E = 2.6$  GPa and  $G = 2.3$  GPa, respectively. The natural vibrational frequency ( $f_0$ ) of the plates was measured by conducting damping tests in still water, which yielded natural frequencies of  $f_0 = 5.1$  Hz and  $f_0 = 7.8$  Hz for the solid and the perforated plates, respectively.

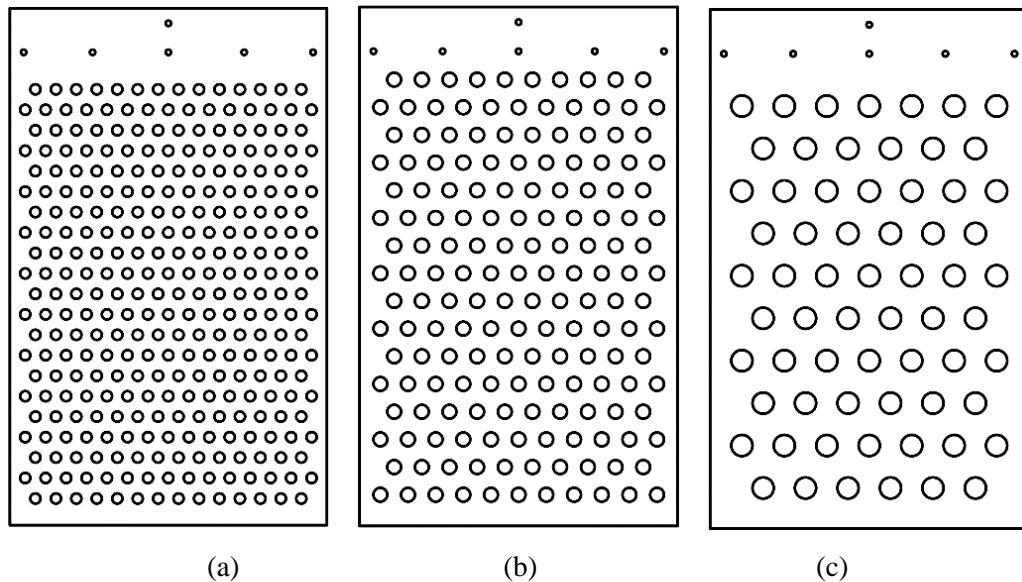


Fig. 4-3. Perforated patterns P1 (a), P2 (b) and P3 (c).

### 4.2.3 Force measurements

Unsteady flow-induced forces on the plate were measured using a three-axis load cell that was incorporated into the support system that held the plate in the test section, as shown in Fig. 4-1. The load cell was capable of measuring drag (the streamwise force), lift (the transverse force) and torque (the rotating force around the vertical axis) exerted on the plate. The estimated uncertainty of the measurements was equal to  $\pm 0.7\%$  of the rated value for all the three perpendicular axes. The details of the force measurement system are provided in Bossi et al. (2017a).

In the results presented herein, the torque signal was used as a representative of flow-induced loading. Ten-minute-long force signals were acquired at a sampling frequency of 200 Hz. The frequency domain analysis involved calculation of Fourier transform of the torque signals, multiplied by ten non-overlapped Hamming windows to reduce leakage error.

### 4.2.4 Flow velocity measurements

Global measurements of the flow velocity in the vicinity of the leading and trailing edges of the plates were performed using high-speed PIV. The PIV system, shown in Fig. 4-1, included a high-repetition pulsed laser that produced a planar laser light sheet, which illuminated the tracer particles. The light scattered by the tracers was captured by a high-speed digital camera. A total of 6000 images were recorded during each data acquisition at the sampling rate of 600 Hz. The instantaneous velocity fields, calculated by cross-correlating the patterns of tracer particles in consecutive images (Raffel et al., 2007), had the spatial resolution of 1.05 vector/mm and 0.54 vector/mm using the camera lenses with the focal lengths of 50 mm and 28 mm, respectively.

As illustrated in Fig. 4-4, three PIV data acquisition planes (DAPs) were considered to characterize the effect of proximity of the perforations to the trailing edge of the plate on three-dimensionality of the near-wake. The vertical elevation of the laser sheet above the bottom edge of the plate,  $e_l$ , is indicated in Fig. 4-2. The DAPs were located in the

vicinity of the mid-span of the plate. Specifically, the DAP3 was located at  $e_l = W/2$ . For the case of the solid plate (P0), the data acquisition was performed only at  $e_l = W/2$ .

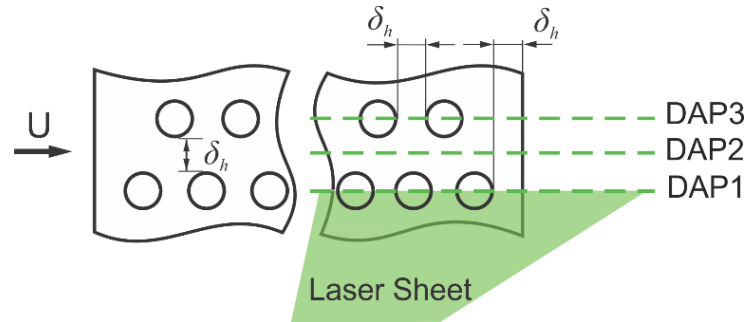


Fig. 4-4. Schematic of the perforation patterns and location of the PIV data acquisition planes (DAPs).

#### 4.2.5 Time-averaging of PIV images

Considering that the nominal frequency of the vortex shedding in the wake was between 5 Hz and 10 Hz, the time interval, during which the 6000 PIV images were acquired, corresponded to 50 to 100 cycles of the wake oscillations. Therefore, this sequence of PIV velocity measurements is suitable for calculation of averaged turbulence parameters. The following time-averaged statistics were calculated (here,  $N = 6000$  is the total number of PIV images):

time-averaged components of velocity:

$$\langle u(x, y) \rangle = \frac{1}{N} \sum_{n=1}^N u_n(x, y), \quad \langle v(x, y) \rangle = \frac{1}{N} \sum_{n=1}^N v_n(x, y); \quad (4-1)$$

root-mean-square (rms) of the transverse velocity fluctuation:

$$v_{rms}(x, y) = \left\{ \frac{1}{N-1} \sum_{n=1}^N [v_n(x, y) - \langle v(x, y) \rangle]^2 \right\}^{1/2}. \quad (4-2)$$

Here,  $u_n(x, y)$  and  $v_n(x, y)$  are the instantaneous streamwise and transverse component of velocity obtained from  $n^{\text{th}}$  PIV image and  $\langle \rangle$  denotes ensemble-averaging.

In order to study the vortex shedding frequencies, the power spectral density (PSD) was calculated by applying Fourier transform to the discrete-time signals of the transverse velocity fluctuations  $v'_n(x, y) = v_n(x, y) - \langle v(x, y) \rangle$  that were extracted at the location of the maximum  $v_{rms}$  value in the near-wake.

## 4.3 Results and discussion

### 4.3.1 Flow-induced loading on plates

The effect of the perforation diameter on the magnitude of the forces induced on the plates is discussed in detail in Bossi et al. (2017a). The most significant trends are summarized herein.

#### 4.3.1.1 Magnitude of flow-induced loading

Values of the mean drag coefficient  $\overline{C}_D$ , defined according to Eqn. (3), are shown in Fig. 4-5 as functions of the Reynolds number  $Re_t = \rho_0 U t / \mu$  for the plates with different perforation diameters.

$$\overline{C}_D = \frac{\overline{D}}{\frac{1}{2} \rho_0 U^2 t W}. \quad (4-3)$$

Here,  $\overline{D}$ ,  $\rho_0$  and  $\mu$  are the mean drag force, the density and the dynamic viscosity of water, respectively. The characteristic area  $tW$  is the projected area on a plane perpendicular to the flow direction. The drag coefficient did not vary substantially with  $Re_t$ , but it significantly changed with the perforation diameter. As the perforation diameter increased from  $\delta_h/t = 0$  to  $\delta_h/t = 1.59$ , the mean drag coefficient  $\overline{C}_D$  monotonically increased by approximately 14%. This trend is consistent with the analytical results for the case of a

bluff body that relate the increase of the mean drag coefficient to the increase of the wake width (Roshko, 1954; Roshko 1955)<sup>1</sup>.

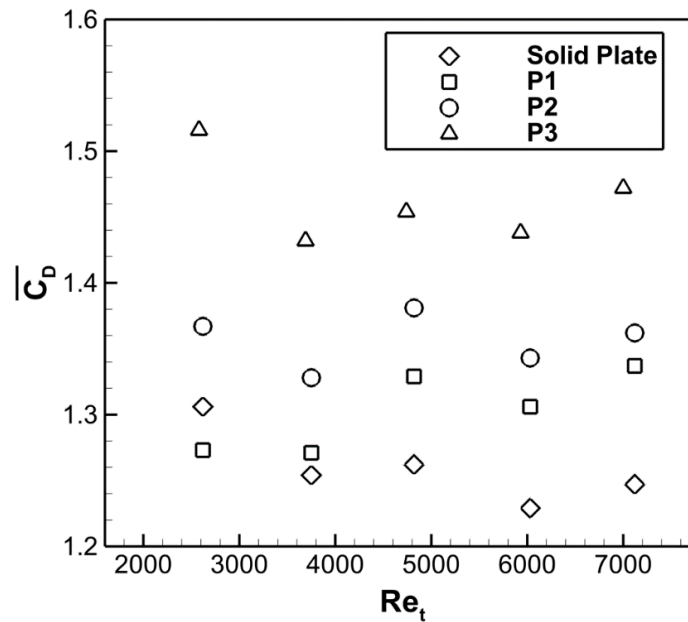


Fig. 4-5. Variation of the mean drag coefficient as a function of the Reynolds number (Bossi et al., 2017a).

The magnitude of the transverse structural vibrations of the plates was related to the values of the fluctuating lift coefficient  $C_L'$ , defined in Eq. (4-4).

$$C_L' = \frac{L'}{\frac{1}{2}\rho_0 U^2 t W}, \quad (4-4)$$

where  $L'$  is the root-mean-square (rms) value of the lift force  $L$ . As shown in Fig. 4-6, in the cases of the solid plate P0 and the perforated plates P1 and P2, the  $C_L'$  values decreased with the increasing  $Re_t$ , reaching asymptotic values in the range  $0.10 < C_L' < 0.29$  for  $Re_t \geq 4800$ . In the case of the plate P3, which had the largest perforations, the fluctuating

<sup>1</sup> A note on Fig. 4-5: Although the mean drag did not vary significantly with the Reynolds number, Fig. 4-5 shows a slight decrease at  $Re_t = 3800$ , followed by an increase at  $Re_t = 4800$ . This observation can be attributed to the transition from laminar to turbulent reattachment at the leading-edge separation bubble (see section 1.1.1).

lift coefficient exhibited a different trend – a monotonic increase for  $Re_t \geq 3800$ . We attributed this increase to a combination of two factors: (a) the onset of lock-on between the structural vibrations and the trailing-edge vortex shedding due to the decreased stiffness of the plate P3, and (b) the enhanced velocity fluctuations within the individual perforations, which is consistent with the fluctuating lift trend and the flow patterns reported for the case of the row of square cylinders (Bao et al., 2012).

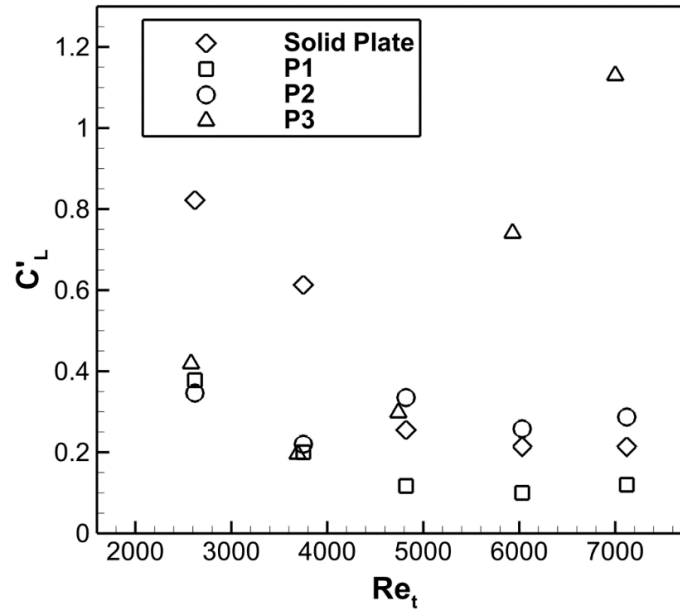


Fig. 4-6. Variation of the fluctuating lift coefficient as a function of the Reynolds number (Bossi et al., 2017a).

#### 4.3.1.2 Unsteady fluctuations of flow-induced loading

The PSD of the flow-induced torque obtained by direct measurements as a function of the frequency and the inflow velocity is shown in Fig. 4-7. In the cases of the solid plate P0 and the perforated plates P1 and P2, shown in Fig. 4-7(a)-(c), the predominant spectral peaks, which corresponded to the frequencies of the trailing-edge vortex shedding, as shown in Section 3.2.2, varied linearly with the inflow velocity. The peaks coinciding with the natural vibrational frequency ( $f_0 = 5.1$  Hz for the solid plate and  $f_0 = 7.8$  Hz for the perforated plates), indicated by blue symbols in Fig. 4-7, were more pronounced, but the linear trend of the increase in the predominant frequencies with the increase of inflow velocity remained consistent. This result indicated the absence of lock-on between the

velocity fluctuations and the structural vibrations for plates P0, P1 and P2. In contrast, in the case of the plate P3, which had the largest perforation diameter  $\delta_h/t = 1.59$ , as the inflow velocity increased above  $U = 0.46$  m/s, the predominant spectral peak with PSD value of  $4.66 \cdot 10^{-3}$  (Nm)<sup>2</sup>/Hz remained locked to the natural vibrational frequency of the plate  $f_0 = 7.8$  Hz (Fig. 4-7(d)). This locked-on condition corresponded to the highest amplitude of the plate vibration, across all considered cases, of  $A_v = 1$  mm (Bossi et al., 2017a). Moreover, the locked-on peak frequencies for  $U = 0.46$  m/s and  $U = 0.55$  m/s corresponded to those of trailing vortex shedding, as shown in Section 4.3.2.2.

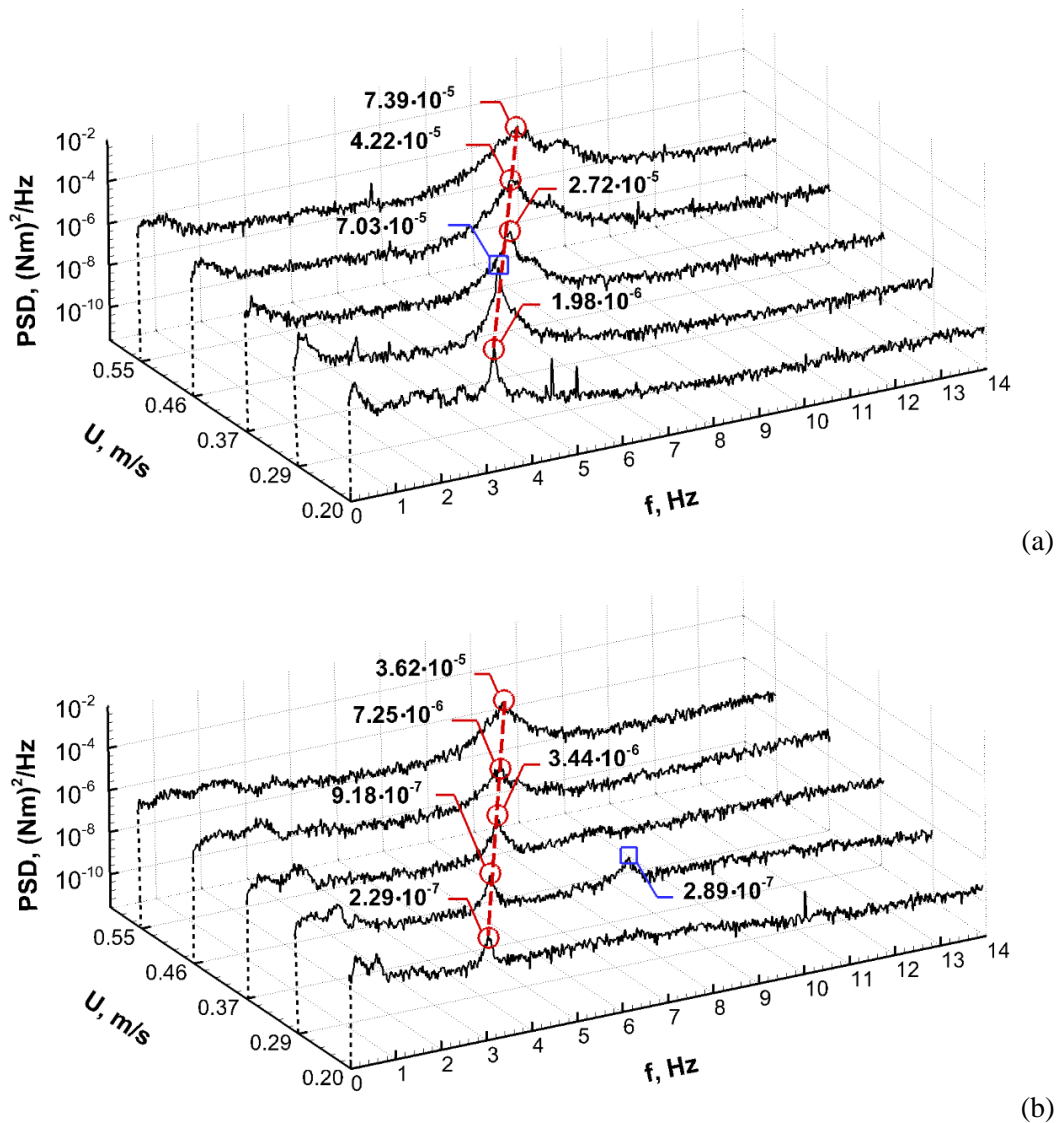
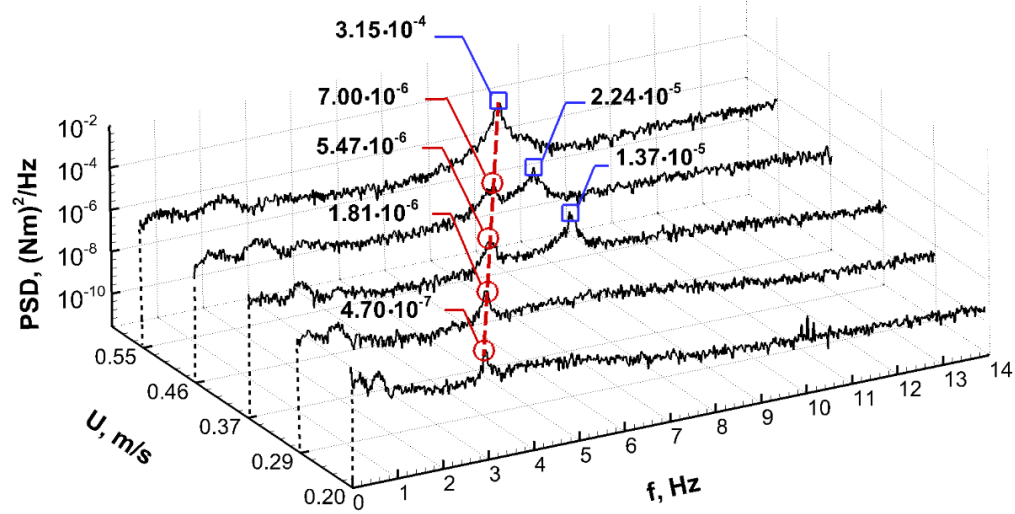
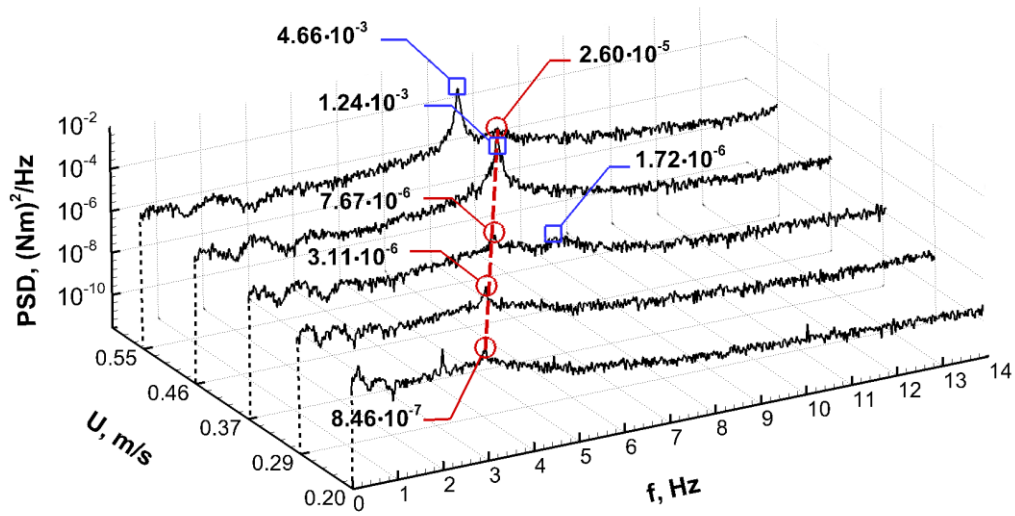


Fig. 4-7. Power spectral density of the flow-induced loading on the plates as a function of the inflow velocity and frequency: (a) P0, (b) P1, (c) P2 and (d) P3.



(c)



(d)

Fig. 4-7. Continued.

The variation of the dimensionless predominant frequencies of the spectra of the flow-induced loading are shown in Fig. 4-8, in the form of Strouhal number based on the thickness of the plate  $St_{t,LC} = f_{LC}t/U$ , as a function of Reynolds number. It was found that  $St_{t,LC}$  was weakly dependent on the Reynolds number, but, as shown in Fig. 4-8, an exception was observed in the case of the plate P3 at the highest investigated  $Re_t$ , where  $St_{t,LC}$  decreased significantly. This result can be attributed to the lock-on between the velocity fluctuations and the structural vibrations that were observed at  $U = 0.55$  m/s. The range of the observed values of  $f$  and their trend with respect of  $Re_t$  were consistent with

previously-reported results by Parker and Welsh (1983), Knisely (1990) and Naudascher and Rockwell (1994).

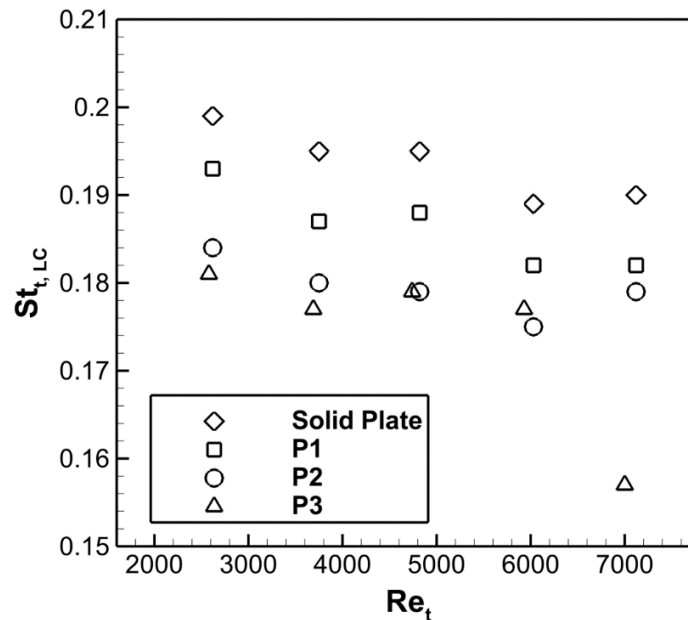


Fig. 4-8. Strouhal number of the unsteady loading as a function of Reynolds number.

### 4.3.2 Separated flow structure

For each perforation pattern  $P_n$  ( $n = 0, 1, 2, 3$ ) and each  $DAP_n$  ( $n = 1, 2, 3$ ), we acquired a series of  $N = 6000$  instantaneous PIV images of the region in the vicinity of the leading edge of the plate as well as the near-wake at five different values of inflow velocity ranging from 0.20 m/s to 0.55 m/s. Using these data, we investigated the effects of the perforations on the spatial extent of the leading-edge separation bubble and the effects of the Reynolds number, the proximity of the perforations to the trailing edge and the perforation diameter on the frequency of the vortex shedding,  $f_{PIV}$ , and the patterns of transverse velocity fluctuations in the near-wake of the plate.

#### 4.3.2.1 Leading-edge separation

The plates considered in the present study had relatively high chord-to-thickness ratio  $c/t = 23.4$  ( $c/t = 23.7$  for plate P3), which resulted in reattachment of the flow that separated from the sharp corners of the leading edge well upstream of the trailing edge (Nakamura et al., 1991).

The leading-edge separation bubble was affected by the perforations through the plate, as shown in Fig. 4-9 in terms of time-averaged streamlines in the laboratory reference frame for the solid plate P0 and for the plate with the largest perforation diameter P3. In the latter case, shown in Fig. 4-9(b), the streamline pattern corresponds to the data acquisition plane located between the rows of perforations – DAP2, which is defined in Fig. 4-4. Part of the flow field close to the plate was obscured by the shadow and the reflected laser light, which prevented correct calculation of the velocity vectors in this area. The optically-inaccessible region is shown by a white area surrounding the plate.

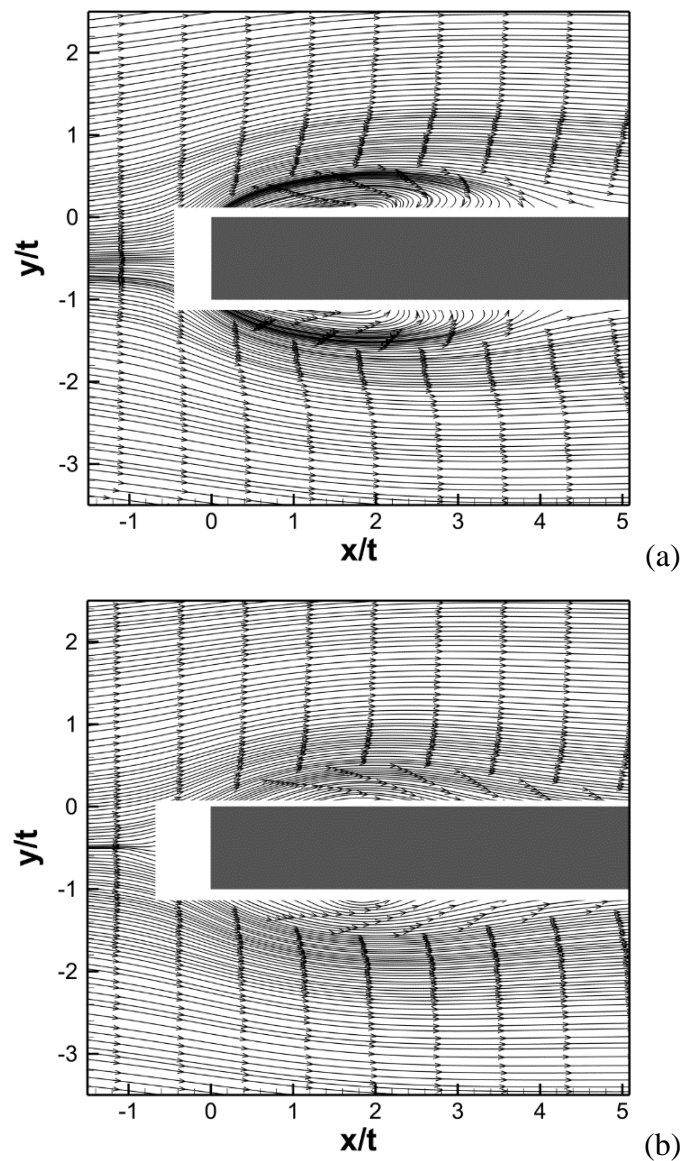


Fig. 4-9. Leading-edge separation bubble,  $U = 0.55$  m/s: (a) P0 and (b) P3, DAP2.

The separated flow region contained a recirculating flow cell, which extended approximately one plate-width in the y-direction (normal to the plate). The thickness of the separation bubble in the normal direction was not significantly affected by the presence of the perforations. For the purpose of comparison between the different perforated plates, we defined the reattachment length  $L_r$  as the distance, in the x-direction, between the leading edge and the location where a time-averaged streamline, extrapolated through the optically-inaccessible region, would intersect the surface of the plate at the steepest angle. For example, the dimensionless reattachment lengths in the cases shown in Fig. 4-9 were estimated as  $L_r/t = 4.1$  and  $L_r/t = 2.6$  for P0 and P3, respectively.

The dimensionless reattachment length  $L_r/t$  increased with the increase of the Reynolds number  $Re_t$  for all considered plates, as shown in Fig. 4-10. The presence of perforations resulted in a substantial decrease of  $L_r/t$  and the rate of its increase with  $Re_t$ . Increasing the perforation diameter did not significantly affect the reattachment length.

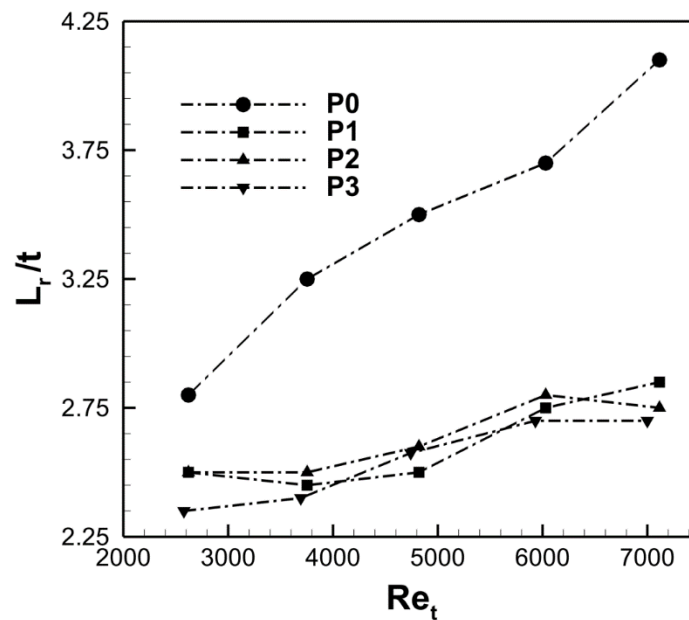


Fig. 4-10. Dimensionless reattachment length as a function of Reynolds number.

Suppression of the leading-edge separation bubble can be attributed to the equalizing effect of the perforations on the local pressure difference across the plate, which is discussed in Section 3.2.3 in the context of the wake dynamics. In all considered cases, the

flow reattached well upstream of the trailing edge, which allowed us to consider the wake structure independently from the dynamics of the leading-edge separation bubble.

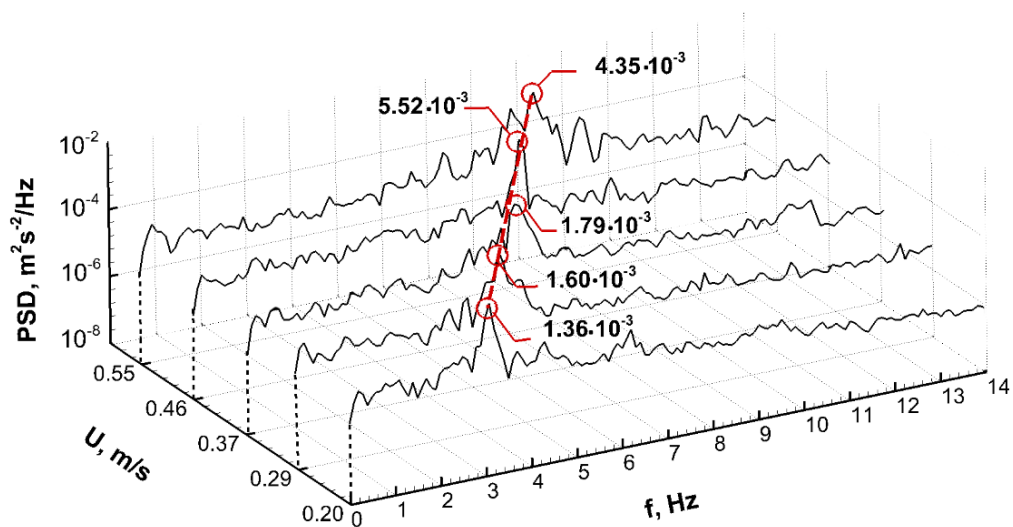
#### 4.3.2.2 Effect of the perforation diameter on the wake structure

##### (a) Trailing-edge vortex shedding frequencies.

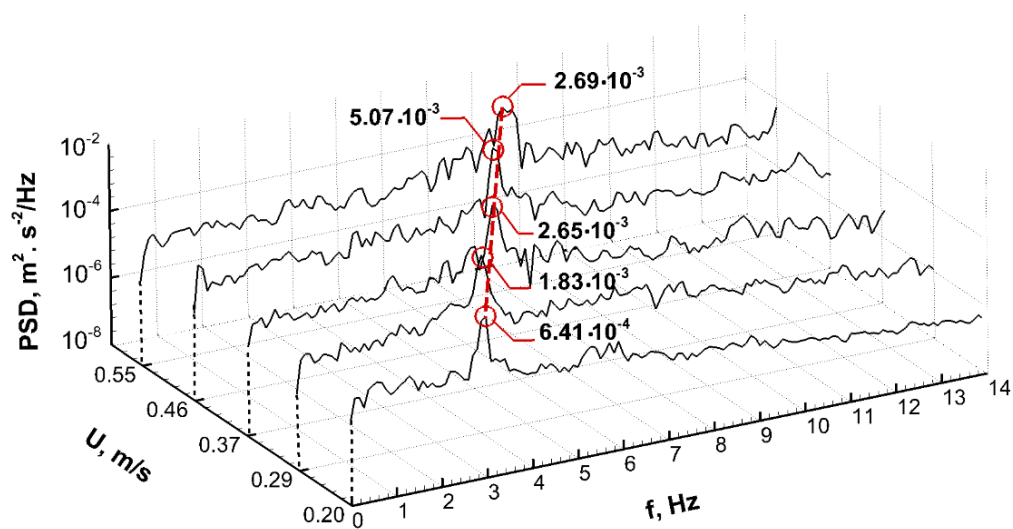
The PSD of the transverse velocity fluctuations in the wake obtained by PIV measurements is shown in Fig. 4-11. For all considered plates and values of the inflow velocity, the frequencies of the peak velocity fluctuations, i.e. of the trailing-edge vortex shedding,  $f_{PIV}$ , corresponded to those of the peaks of the PSD obtained by the force measurements,  $f_{LC}$  (Fig. 4-7). Similarity of the trends of the spectra of measured forces and those of the transverse velocity fluctuations in the wake indicates that the trailing-edge vortex shedding was the governing mechanism of the generation of flow-induced loading on the plate. The frequencies increased with the increase of the inflow velocity. The peak amplitudes of the velocity fluctuations did not vary significantly in the considered range of the inflow velocities.

At  $U = 0.55$  m/s,  $f_{PIV}$  remained locked-on to the natural vibrational frequency of the plate, as shown in Fig. 4-11(d). This trend is consistent with the lock-on of the flow-induced loading frequencies  $f_{LC}$  observed in Fig. 4-7(d).

The PSD spectra of the velocity fluctuations in the three DAPs were qualitatively similar. Thus, only the data corresponding to DAP2 is presented in Fig. 4-11. However, the peak values of the velocity fluctuations in DAP1 were lower than those in the other two DAPs. This reduction of the amplitude of the transverse velocity fluctuations was due to the proximity of the last (downstream-most) perforation to the trailing edge. Transverse flow within the perforation diminished the local pressure difference between the upper and the lower surfaces of the plate, leading to suppression of the trailing-edge vortex shedding, as discussed in Section 4.3.2.3.

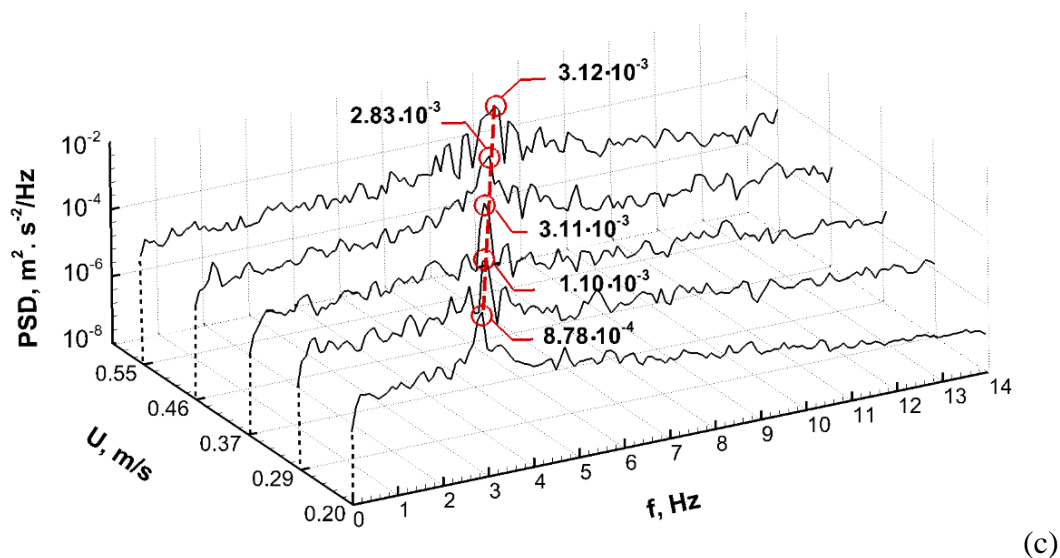


(a)

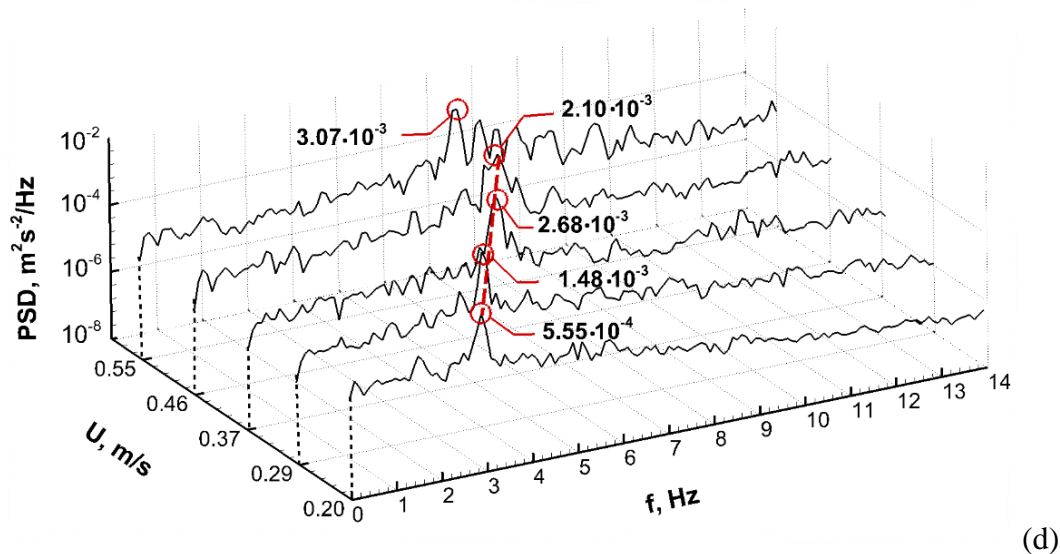


(b)

Fig. 4-11. Power spectral density for transverse flow velocity fluctuations as a function of the inflow velocity and frequency for (a) P0, (b) P1, (c) P2, (d) P3. The data for the plates P1, P2, P3 correspond to DAP2.



(c)



(d)

Fig. 4-11. Continued.

Fig. 4-12 shows the variation of the non-dimensional frequencies of the transverse velocity fluctuations in DAP1, in the form of the Strouhal number based on the thickness of the plates  $St_{t,PIV} = f_{PIV}t/U$ , as a function of the Reynolds number. The modified Kirchhoff's theory (Roshko (1955)) predicts that the bluffness of a cylindrical body increases with the decrease of the vortex shedding frequency. In the present case of bluff perforated plates, we observed that increasing the Reynolds number had similar effect on the vortex shedding frequency and the scale of the shed vortices only in the case of the largest perforation diameter (plate P3), where the vortex shedding frequencies locked on

to natural vibrational frequency of the plate at higher inflow velocities in the considered range. At the highest investigated value of  $Re_t$ , in the case of the plate P3, the  $St_{t,PIV}$  decreased particularly significantly, which can be attributed to the coupling between the trailing-edge vortex shedding and the transverse oscillations of the plate, confirmed by the lock-on of the loading frequencies and the vortex-shedding frequencies observed in Fig. 4-7 and Fig. 4-11, respectively. For the reference case of the solid plate and the plates P1 and P2, the Strouhal number did not vary significantly in the considered range of Reynolds numbers.

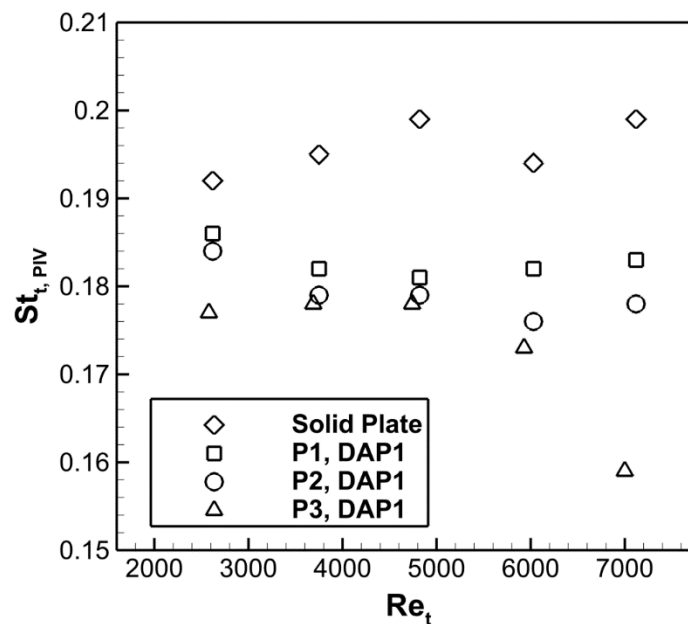


Fig. 4-12. Strouhal number of the unsteady loading as a function of Reynolds number.

*(b) Velocity fluctuations*

At the highest considered value of the inflow velocity, corresponding to  $Re_t = 7116$ , increasing the perforation diameter from  $\delta_h = 9.4$  mm (P1) to  $\delta_h = 12.7$  mm (P2) resulted in a moderate increase of the peak value of the dimensionless transverse velocity fluctuations  $(v_{rms})_{max}/U$  and the spatial extent of the region, where significant velocity fluctuations occurred, as shown in the plots of Fig. 4-13 (a, b) for the case of DAP1. We attribute this effect to the increased bluntness of the plate, caused by the perforations, as discussed in Section 4.3.2.3.

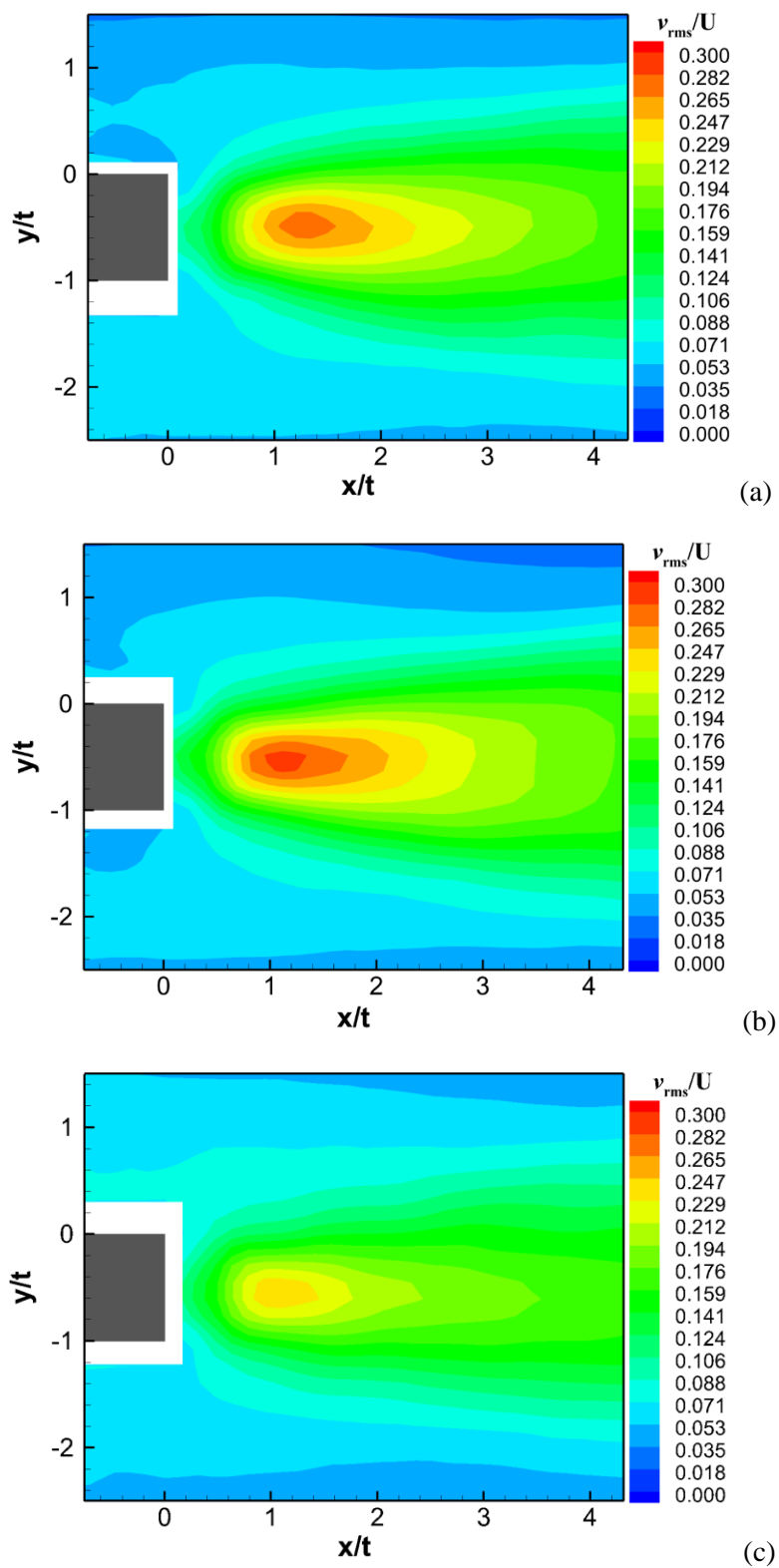


Fig. 4-13. Dimensionless distribution of the rms of the transverse velocity fluctuations in the wake of the perforated plates,  $U = 0.55$  m/s, in DAP1: P1 (a), P2 (b) and P3 (c).

When the perforation diameter increased further to  $\delta_h = 19.5$  mm (P3), the periodic vortex formation in the wake was more effectively interrupted, as the local pressures on the upper and the lower surfaces of the plate were equalized in the vicinity of the individual perforations. As a result, both the spatial extent and the magnitude of the velocity fluctuations in the wake significantly decreased, as shown in Fig. 4-13(c).

A similar trend is observed in Fig. 4-14, which shows variation of the peak values of the dimensionless rms velocity fluctuations,  $(v_{rms})_{max}/U$ , as a function of the perforation diameter in DAP1 for five different inflow velocities corresponding to  $2578 \leq Re_t \leq 7116$ . The plot indicates that the wakes of all perforated plates had substantially lower velocity fluctuations, compared to the solid plate. In other words, periodic vortex formation in the wake was effectively suppressed by the transverse perforations, which can be represented by a Rayleigh conductivity boundary condition.

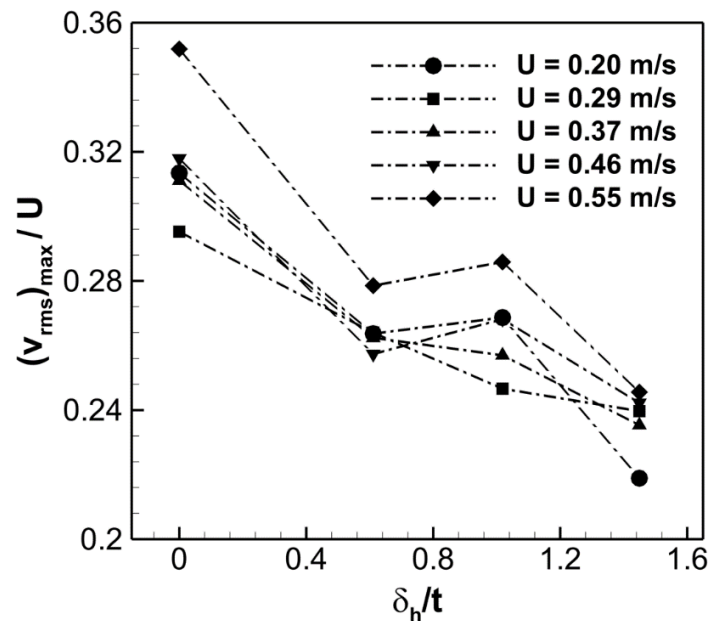


Fig. 4-14. Variation of the maximum of the rms of the transverse dimensionless velocity fluctuation as a function of the perforation diameter at DAP1.

Comparing the different perforated plates, we observed that increasing the perforation diameter from  $\delta_h = 9.4$  mm (P1) to  $\delta_h = 12.7$  mm (P2) corresponded to increasing the bluffness of the plate in a way similar to increasing the surface roughness.

As a result, vortex formation in the near-wake was enhanced, as shown in the dimensionless  $v_{rms}$  plots of Fig. 4-13 and Fig. 4-14.

Further increasing the perforation diameter to  $\delta_h = 19.5$  mm (P3) led to a substantial decrease of the peak dimensionless velocity fluctuations in the wake due to the diminished pressure difference across the plate. Therefore, for the case of the largest considered perforations, the increased Rayleigh conductivity counteracted and overcame the effect of the increased surface roughness.

#### 4.3.2.3 *Effect of proximity of the perforations to the trailing edge on the wake structure*

##### *(a) Wake width*

We related the flow oscillations in the wake, to the bluffness of the plate, defined after Roshko (1955) as  $d'/t$ . Here,  $d'$  is wake width, which is equal to the distance between the separating streamlines at the downstream location corresponding to the trailing edge of the plate. In the present study, the  $d'$  values were calculated based on time-averaged values of the out-of-plane vorticity  $\langle \omega_z \rangle$  downstream of the plate. Specifically, we calculated the slope  $\partial \langle \omega_z \rangle / \partial y$  of the vorticity profiles at  $x = t$  using a second-order central finite difference scheme. The wake width was taken to be equal to the vertical distance between the points above and below the plate where  $\partial \langle \omega_z \rangle / \partial y$  reached the minimum value.

The bluffness increased with the increase of the Reynolds number, as shown in Fig. 4-15 for the case of the perforated plate P3. The increase of the bluffness was particularly rapid in the DAP2, which corresponded to the line across a solid section of the plate (Fig. 4-4). In DAP1 and DAP3, which crossed the rows of perforations, the fluid oscillations inside the perforations inhibited the increase in bluffness by interfering with the development of the boundary layers along the plate.

In order to understand the effect of proximity of the perforations to the trailing edge of the plate, which is different in each DAP, we considered the local effect of the individual perforations on the flow around the plate. The effect of the perforations can be described

using the concept of Rayleigh conductivity, which relates the volume flux  $Q$  in the transverse direction inside a perforation to the local pressure difference  $\Delta p$  across the plate. Assuming the time dependence of the fluctuating fluid properties of the form  $e^{i\omega t}$ , where  $t$  is time and  $\omega$  is the frequency, Rayleigh conductivity  $K_R$  of the perforation is defined in Eqn. (3) by analogy with the Ohm's law, which defines electrical conductivity as the ratio of the current to the potential difference (Howe, 1998).

$$K_R = \frac{i\omega\rho_0 Q}{\Delta p}, \quad (4-5)$$

where  $\rho_0$  is the fluid density. For perforated plates of finite thickness in grazing uniform flow and in the absence of vortex shedding from the leading edge of the perforation, it can be shown analytically that  $K_R$  is proportional to the perforation radius  $R$  (Howe, 1998). Thus, as the perforation diameter was increased in the current experiments, the increased Rayleigh conductivity resulted in the decreased local pressure difference across the plate. In turn, the diminished pressure difference,  $\Delta p$ , in the vicinity of the trailing edge in DAP1 and DAP3 led to the suppression of the periodic formation of large-scale vortical structures in the near-wake and smaller wake width  $d'$ , compared to DAP2.

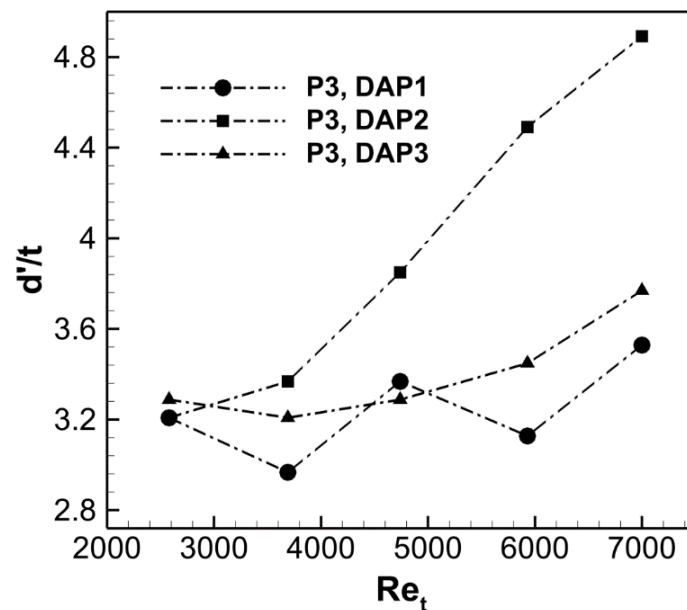


Fig. 4-15. Variation of the wake width as a function of the Reynolds number for the perforated plate P3.

*(b) Boundary layer profiles*

Fig. 4-16 shows the time-averaged boundary layer profiles at the trailing edge of the plate with the largest perforations (P3) for five different inflow velocities, corresponding to the Reynolds numbers  $Re_t = 2578, 3693, 4742, 5932$  and  $7000$ . In order to provide a reference, velocity profiles for the solid plate are shown in all plots.

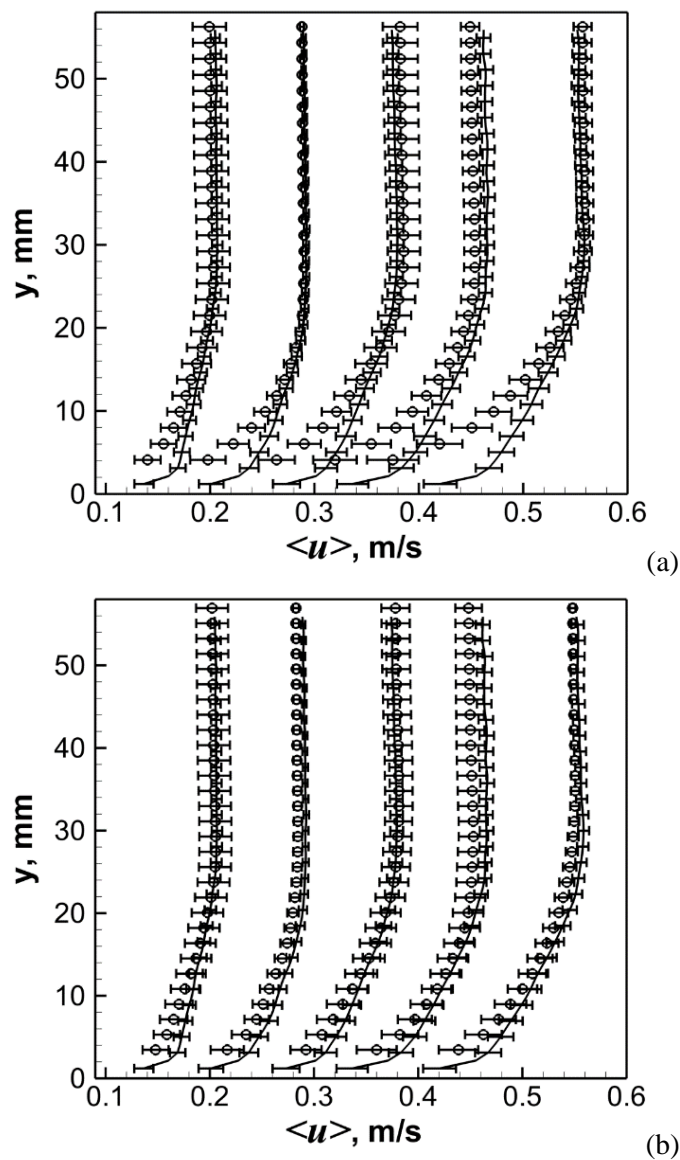


Fig. 4-16. Boundary layer at different upstream velocities: — solid plate,  $\circ$  perforated plate P3 ( $\delta_h = 19.5$  mm) at DAP1 (a), DAP2 (b) and DAP3 (c).

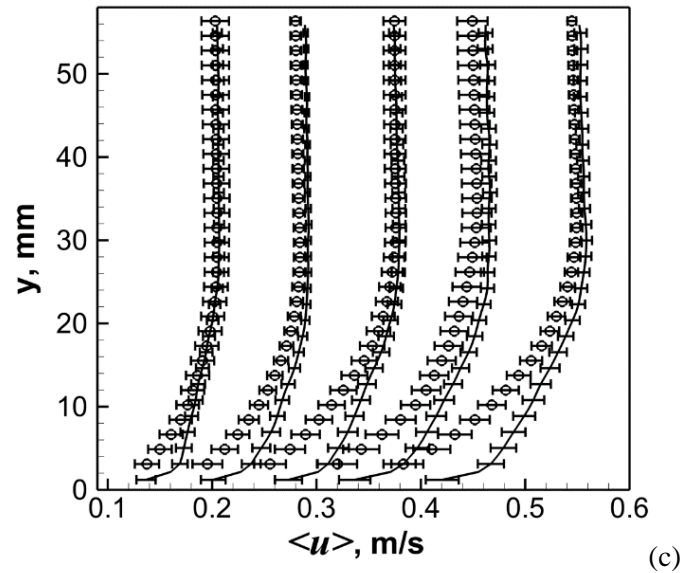


Fig. 4-16. Continued.

The corresponding boundary layer profiles for the plates with smaller perforation diameters (P1 and P2) matched those of the solid plate for all values of the inflow velocity, considering the inherent uncertainty of the PIV measurements, and are not presented here. The uncertainty of measurements was quantified based on the statistical analysis of the correlation process considering differences in the intensity pattern in consecutive PIV images (Wieneke, 2015) using software LaVision DaVis 8.2.

As the perforation diameter increased to  $\delta_h = 19.5$  mm (plate P3), the boundary layer profiles deviated from those corresponding to the solid plate for all considered values of the inflow velocity. This deviation was particularly pronounced close to the surface of the plate, and it increased with the increase of the inflow velocity. Moreover, larger difference between the boundary layer profiles of the perforated plate and that of the solid plate was observed at DAP1, shown in Fig. 4-16(a), compared to DAP3. The separating boundary layer corresponding to DAP1 was influenced by the proximity of the last (downstream-most) perforation, which was located closer to the trailing edge of the plate in DAP1 than it was in DAP3. Fig. 4-16 indicates that as the distance from the last perforation to the trailing edge decreases, which corresponds to transition from DAP2 to DAP 3 to DAP1, the deviation of the boundary layer profile from that of the case of the reference (solid) plate increased.

*(c) Velocity fluctuations*

Proximity of the perforations to the trailing edge of the plate (represented by different DAPs) significantly affected formation of the large-scale vortices in the near-wake. As shown in Fig. 4-17, the peak value and the spatial extent of the region corresponding to elevated values of  $v_{rms}$  decreased as the distance between the last (downstream-most) perforation and the trailing edge decreased.

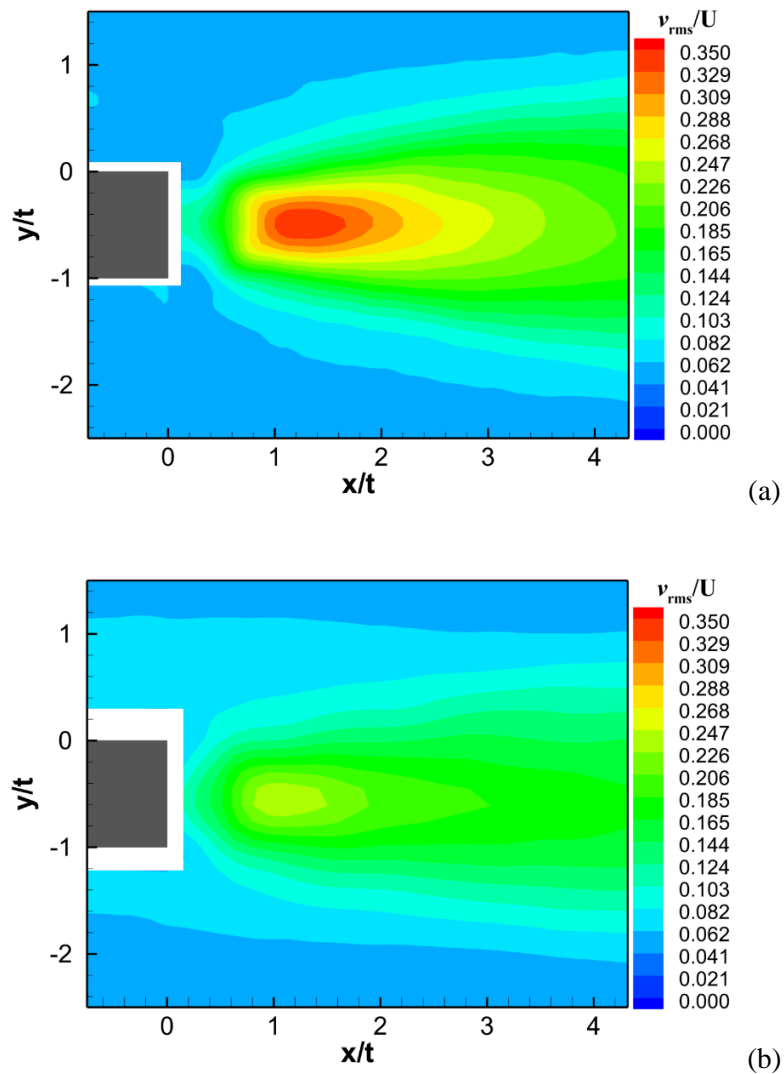


Fig. 4-17. Distribution of the rms of the transverse dimensionless velocity fluctuations in the wake of the plate,  $U = 0.55$  m/s: Solid plate (a); Perforated plate P3: DAP1 (b), DAP2 (c) and DAP3 (d).

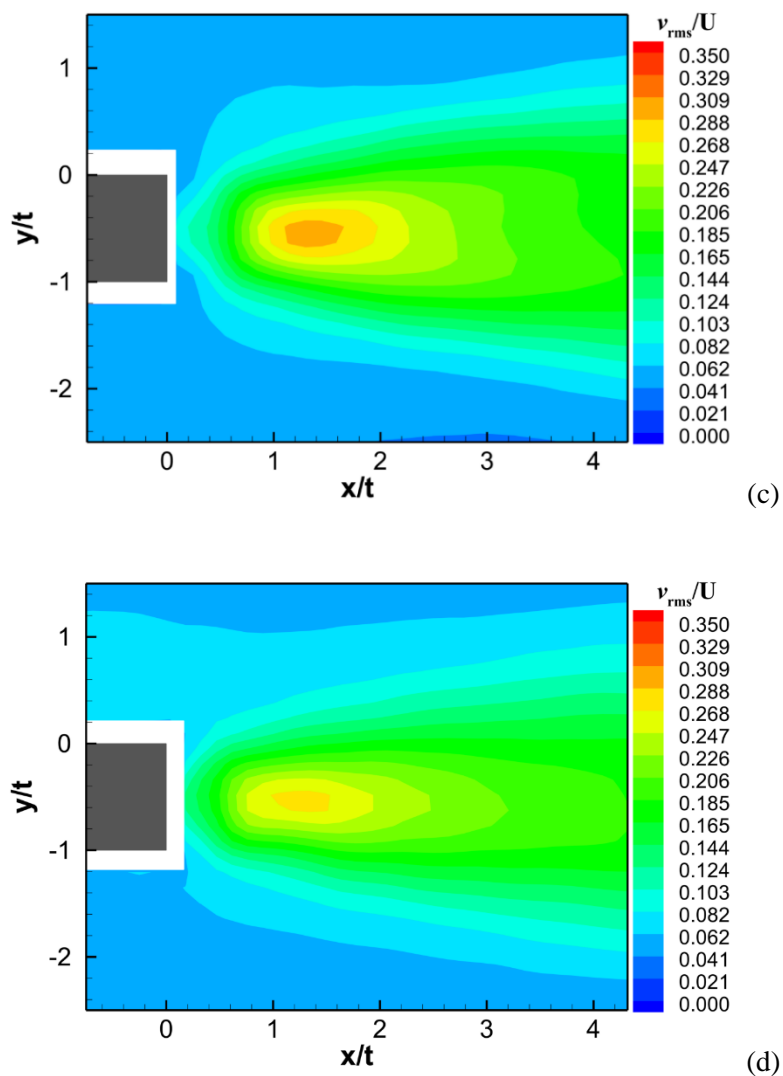


Fig. 4-17. Continued.

The highest peak value of the dimensionless rms velocity fluctuations  $(v_{rms})_{max}/U = 0.349$ , was observed in the reference case of the solid plate, shown in Fig. 4-17(a) for the case of  $U = 0.55$  m/s ( $Re_t = 7116$ ). The region of significant transverse fluctuations extended from  $x/t = 0.8$  to  $x/t = 3.2$ . In this region, the shear layer that separated from the upper and the lower surfaces of the plate interacted, which led to the periodic formation of clockwise and counter-clockwise vortices. The mechanism of this periodic vortex formation was recently investigated by Negri et al. (2011) using PIV for the case of a rectangular cylinder (a short bluff plate). The authors linked the formation of the vortices

of particular sign to the pressure difference on the top and the bottom surfaces of the plate at that particular phase of the flow oscillation cycle.

In the case of the perforated plate P3, which is representative of all considered perforated plates and is shown in Fig. 4-17(b)-(d), the local instantaneous pressure difference between the upper and the lower surfaces of the plate was alleviated through the perforations, which inhibited the formation of large-scale vortices downstream of the trailing edge. The degree of the interference with the periodic vortex formation depended on the proximity of the last perforation to the downstream edge. The transition from DAP2 to DAP 3 to DAP1 corresponded to a decrease of the amplitude of transverse velocity fluctuations, which in turn represented the decrease in the scale of the shed vortices.

In DAP2, which passed between the rows of perforations as shown in Fig. 4-4, the local communication between the upper and the lower surfaces of the plate was limited. As a result, the periodic vortex formation was only moderately disrupted by the adjacent rows of perforations. The pattern of the  $v_{rms}$  contours shown in Fig. 4-17(c) is qualitatively similar to that of the reference case of the solid plate (Fig. 4-17(a)). However, three-dimensionality of the flow induced by the adjacent perforations (in DAP1 and DAP3) resulted in a decrease in the peak value of the dimensionless rms velocity fluctuations in DAP2 of the plate P3 ( $(v_{rms})_{max}/U = 0.300$ ), compared to that of the solid plate. The spatial region, where significant amplitudes of velocity fluctuations were observed also decreased. In the downstream direction, the fluctuations increased at the same distance from the trailing edge ( $x/t = 0.8$ ) as in the case of the solid plate, which corresponded to the formation length of the large-scale vortices. However, no significant amplitudes were observed for  $x/t > 2.4$ .

In DAP3, the last (downstream-most) perforation was located relatively far (at the distance of  $2\delta_h$ ) from the trailing edge, as shown in Fig. 4-4. The pressure on the upper and the lower surfaces of the plate was equalized at the location of the perforation, and this effect was felt at the trailing edge, where the shear layers separated and formed flow recirculation cells (Malavasi and Guadagnini, 2007). The unsteady vortex formation still took place, as evidenced by a well-defined local maximum of  $v_{rms}$  that can be observed in

Fig. 4-17(d). Significant values of  $v_{rms}$  were still observed between  $x/t = 0.8$  to  $x/t = 2.4$  in the streamwise direction. However, in the transverse direction, the extent of the region of significant velocity fluctuations decreased, compared to the case of DAP2. The peak value of the dimensionless rms of velocity fluctuations decreased to  $(v_{rms})_{max}/U = 0.275$ , indicating a disrupted process of the periodic trailing-edge vortex shedding in the wake due to the pressure-equalizing effect of the last perforation on the separating shear layers.

Comparing the DAP1 to the DAP3, the former had a perforation located closer to the trailing edge of the plate, which reduced the pressure difference at the upper and the lower surfaces of the plate in the immediate vicinity of the trailing edge. As a result, the periodic vortex shedding in DAP1 was inhibited, as illustrated by the  $v_{rms}$  plot of Fig. 4-17(b). Among all considered data acquisition planes, the DAP1 exhibited the lowest value of the peak of the dimensionless rms velocity fluctuations  $(v_{rms})_{max}/U = 0.244$ . There were occasional deviations from this trend at the lower values of the inflow velocity, where DAP2 and DAP3 exhibited similar peak values of  $v_{rms}$ . Moreover, the values of elevated  $v_{rms}$  above the background level typical of the turbulent wake were localized to a small area between  $x/t = 0.8$  and  $x/t = 1.1$ , which indicated less consistent process of trailing-edge vortex shedding that was observed in the other data acquisition planes.

#### 4.4 Conclusions

The effect of transverse perforations and inflow velocity on the unsteady loading on bluff rectangular plates was investigated using direct force measurements and quantitative flow imaging in the near-wake using PIV.

The vortex shedding frequencies were in good agreement with the frequencies of the measured flow-induced forces for all considered perforation patterns. Thus, it was determined that the trailing-edge vortex shedding was the main mechanism of generating the unsteady loading on the plates and the resulting flow-induced vibrations.

In the cases of relatively small perforations, the velocity fluctuations in the near-wake were enhanced, and the perforations had a similar effect on the bluffness of the plate to that

of the increase of the surface roughness. However, further increasing the perforation diameter diminished the pressure difference across the plate (between the upper and the lower surfaces), which led to suppression of the velocity fluctuations.

The frequency of the vortex shedding and of the loading on the plates decreased with the increase of the perforation diameter and of the Reynolds number. Therefore, the decrease of the frequency of velocity oscillations in the wake can be attributed to the increased bluffness of the plate that resulted from the transverse flow oscillations in the individual perforations. This effect, which can be modeled by the Rayleigh conductivity boundary condition, resulted in the localized decrease of pressure difference across the plate in the vicinity of the individual perforations. Thus, larger-diameter perforations effectively suppressed periodic formation of the large-scale vortical structures in the near-wake.

The considered pattern of the staggered perforations resulted in a three-dimensional boundary layer, whose thickness and the deviation of the velocity profile from that corresponding to the case of the solid plate increased with the decrease of the distance of the last (downstream-most) perforation from the trailing edge of the plate.

Moreover, the proximity of the perforations to the trailing edge governed the three-dimensional structure of the near-wake. In the cross-sectional planes corresponding to the close proximity of the perforations to the downstream edge, the pressure difference across the plate and, consequently, periodic trailing-edge vortex shedding were suppressed.

The largest considered perforation diameter resulted in coupling between the trailing-edge vortex shedding and transverse oscillations of the plate. This resonance manifested itself as the lock-on of the vortex shedding frequency to the natural vibrational frequency of the plate and an increased magnitude of the flow-induced loading.

## 5 Conclusions and future works

### 5.1 Ship airwake

The operation, launch and recovery of helicopters from and to vessels involve significant risks and can be crucially challenging for pilots. The interaction of the vessel with the impinging wind as well as the effects of forward motion of the vessel can create a highly disturbed region over the helicopter platform, which is associated with spatially and temporally varying velocity field and high turbulence over the helicopter platform. In the present research, this interaction and the resulting airwake were studied for a Canadian Coast Guard Icebreaker, using flow measurement technique of particle image velocimetry. The experiments were conducted in a flow visualization water channel on a scaled model of the icebreaker. This research provided insight into the complex structure of the ship airwake, and aimed to identify the operation conditions associated with minimum turbulence. For the ship geometry, characterized by sharp edges and associated with massively separated flow regions, the effects of Reynolds number on the resulted airwake were investigated. Furthermore, the effects of inflow condition, representing the forward motion of the ship and the impinging wind were quantified. As well, the effects of the unsteady changes in wind direction were studied and the results were compared with those of constant wind.

#### 5.1.1 Key findings

- The independence of the flow patterns in the wake of a bluff body, associated with sharp edges was verified. It was observed that, for sufficiently large Reynolds numbers, the flow patterns in the wake, characterized by massively-separated flow regions, are independent of the Reynolds number.
- The simulated atmospheric boundary layer promoted the development of higher turbulent velocity fluctuations over the helicopter platform, which can lead to an increase in the workload of the pilots.

- The spatial structure of the airwake substantially depended on the inflow condition. In specific, the effects of the inflow condition was pronounced for the incidence angles that resulted in larger-scale flow separation from the superstructure.
- The incidence angles associated with highest turbulence were identified. For a constant inflow direction, the incidence angles of  $300^\circ$ , and for a transient inflow direction, the incidence angles of  $60^\circ$  were associated with the maximum values of the turbulence intensity over the helicopter platform.
- The transient changes in the inflow direction contributed to the formation of the recirculating vortical cells over the helicopter platform, which were the results of the flow separation from the top and the sides of the superstructure.
- Generally, the turbulent intensity over the helicopter platform increased by the increase of the rate of change of the inflow direction. However, it was observed that this trend also depended on the nominal direction of the inflow. For the incidence angles of  $60^\circ$ , associated with highest turbulent levels, the clockwise change in the inflow direction increased turbulent velocity fluctuations, while counterclockwise change in the inflow direction diminished the flow unsteadiness over the helicopter platform.
- The escalated velocity fluctuations and turbulence level in the ship airwake over the helicopter platform, known to increase pilots' workload, were directly dependent on the incidence angle of the CCG icebreaker with the impinging flow, therefore, for the current design of the CCG icebreaker it is recommended that the operation of helicopter is minimized or avoided for incidence angles between  $0^\circ$  to  $90^\circ$  as well as  $270^\circ$  to  $330^\circ$ . It should be noted that the enhanced velocity fluctuations in the airwake pose more significant risk for the helicopter operation when the wake is mainly due to the impinging wind, rather than the ship forward motion. This range of incidence angles were also associated with the highest

velocity fluctuations when the wake was affected by an unsteady change in wind direction.

### **5.1.2 Future work**

The present study creates basis for better understating of the ship airwake and the turbulent velocity fluctuations resulted from interaction between the impinging wind and a vessel. This study can be further expanded by considering the effects of the helicopter fuselage and rotor on the airwake. To this end, this experimental investigation can encompass a scaled model of the rotor and fuselage of the helicopter, and capture the effects of the various launch and recovery schemes on the generated wake. Additionally, the direct force measurement techniques can be used to obtain the unsteady loading on the rotor as well as the fuselage. In specific, the effects of spatial gradients of the velocity field on the rotor can be of significance, since depending on the launch and recovery scheme, the rotor can be exposed to different levels of turbulence, exerting spatially varying loading on the rotor.

Furthermore, it has been shown that the modification of the geometry of the superstructure and the hangar can reduce the velocity fluctuations in the ship airwake over the helicopter platform (see chapter 1), therefore, the effects of geometry modifications, e.g. rounding of the edge of the hangar, can be considered as a future step in this research.

## **5.2 Wake of perforated plates**

Bluff elongated plates at zero incidence angle have many engineering applications, where the impinging flow exerts unsteady loading on the plate and alters the flow around and in the downstream on the plates. Historically, many studies focused on such phenomena, but the effects of the transverse perforations on the unsteady wake structure and the exerted forces have received little attention. Using particle image velocimetry and the direct force measurement, the present work considered high aspect ratio rectangular plates with staggered transvers perforations, and aimed to provide insight into the origins of the exerted unsteady loading.

### 5.2.1 Key findings

- For the plates with high chord-to-thickness ratio with transverse perforations, the vortex shedding frequencies were in good agreement with the frequencies of the measured flow-induced forces for all considered perforation patterns. Therefore, the trailing-edge vortex shedding was identified as the main mechanism of generating the unsteady loading on the plates and the resulting flow-induced vibrations.
- In the cases of relatively small perforations, the velocity fluctuations in the near-wake were enhanced. However, further increasing the perforation diameter resulted in the diminished pressure difference across the plate, which in turn suppressed the velocity fluctuations.
- The frequency of the vortex shedding and of the loading on the plates decreased with the increase of the perforation diameter and of the Reynolds number. Moreover, larger-diameter perforations effectively suppressed periodic formation of the large-scale vortical structures in the near-wake.
- The staggered pattern of perforations resulted in varying proximity of the perforations to the trailing edge, which in turn created a three-dimensional structure in the near-wake. In the cross-sectional planes corresponding to the close proximity of the perforations to the downstream edge, the pressure difference across the plate and, consequently, periodic trailing-edge vortex shedding were suppressed. Furthermore, various proximity to the trailing edge created a three-dimensional boundary layer.
- The largest considered perforation diameter exhibited a lock-on of the vortex shedding frequency to the natural vibrational frequency of the plate, which in turn led to an increased magnitude of the flow-induced loading.

- Although the increase of the perforation diameter resulted in a decrease in the frequency of the unsteady loading exerted on the plates, the magnitude of vibrations increased significantly for the plate with the highest perforation diameter due to the lock-on between the trailing-edge vortex shedding and structural vibrations. Therefore, in order to reduce the risk of excessive vibrations, it is recommended to use perforated plates with material properties yielding natural vibrational frequencies which are not in the range of the trailing-edge vortex shedding frequencies. In this research, for the Reynolds numbers investigated, this range was  $2.9 \text{ Hz} < f < 8 \text{ Hz}$ .

### 5.2.2 Future work

The present experimental study quantified the effects of the transverse perforations on the wake structure and the flow-induced loading on the plates. The main mechanism of such unsteady loading was identified and the role of perforations on the velocity fluctuations on the wake was observed. As future extensions of this study, various equivalent area ratio ( $\beta$ ) can be considered. Additionally, the 3-dimensionality of the near-wake can be investigated for uniform perforation patterns. Since the trailing-edge vortex shedding was identified as the main mechanism for generating the unsteady loading on the plates, the effects of different geometries of the trailing edge, e.g. tapered or rounded, can be of interest. Furthermore, in many engineering applications, e.g. flowrate control, the perforated plates are used side by side, where the flow is bounded on one or both sides, or in tandem, which may increase the turbulence level or create large scale vortices experienced by the downstream plate.

Perhaps more interestingly, the pressure-equalizing effects of the perforations can be further studied by blocking perforations by a relatively thin membrane, which effectively separates two sides of the plate.

## Bibliography

Aider, J.-L., Danet, A., Lesieur, M., 2007. Large-eddy simulation applied to study the influence of upstream conditions on the time-dependant and averaged characteristics of a backward-facing step flow. *Journal of Turbulence* 8, N51.

Al-Garni, A.M., Bernal, L.P., 2010. Experimental study of a pickup truck near wake. *Journal of Wind Engineering and Industrial Aerodynamics* 98 (2), 100-112.

Arslan, T., Malavasi, S., Pettersen, B., Andersson, H.I., 2013. Turbulent Flow Around a Semi-Submerged Rectangular Cylinder. *Journal of Offshore Mechanics and Arctic Engineering* 135 (4).

ASCE, 1996. Wind-Tunnel Studies of Buildings and Structures. *Journal of Aerospace Engineering* 9 (1), 19-36.

Bao, Y., Wu, Q., Zhou, D., 2012. Numerical investigation of flow around an inline square cylinder array with different spacing ratios. *Computers & Fluids* 55, 118-131.

Bardera-Mora, R., 2014a. Experimental Investigation of the Flow on a Simple Frigate Shape (SFS). *The Scientific World Journal* 2014, 8.

Bardera-Mora, R., 2014b. Flow field velocity on the flight deck of a frigate. *Proceedings of the Institution of Mechanical Engineers, Part G: Journal of Aerospace Engineering* 228 (14), 2674-2680.

Bardera-Mora, R., Meseguer, J., 2014. Flow in the near air wake of a modified frigate. *Proceedings of the Institution of Mechanical Engineers, Part G: Journal of Aerospace Engineering* 229 (6), 1003-1012.

Bearman, P.W., 1980. Review—Bluff Body Flows Applicable to Vehicle Aerodynamics. *Journal of Fluids Engineering* 102 (3), 265-274.

Bearman, P.W., 1997. Near wake flows behind two- and three-dimensional bluff bodies. *Journal of Wind Engineering and Industrial Aerodynamics* 69-71, 33-54.

Benedict, L.H., Gould, R.D., 1996. Towards better uncertainty estimates for turbulence statistics. *Experiments in Fluids* 22 (2), 129-136.

Blocken, B., Defraeye, T., Koninckx, E., Carmeliet, J., Hespel, P., 2013. CFD simulations of the aerodynamic drag of two drafting cyclists. *Computers & Fluids* 71, 435-445.

Bossi, F.C., 2016. Fluid-dynamic noise in control devices. Polytechnic University of Milan.

Bossi, F.C., Barannyk, O., Rahimpour, M., Malavasi, S., Oshkai, P., 2017a. Effect of transverse perforations on fluid loading on a long, slender plate at zero incidence. *Journal of Hydrology and Hydromechanics* 65 (4), 378-384.

Bossi, F.C., Barannyk, O., Rahimpour, M., Malavasi, S., Oshkai, P., 2017b. Experimental Analysis of Wake Structure of Flat Plates with Transverse Perforations at Zero Incidence, in: Zhou, Y., Kimura, M., Peng, G., Lucey, A.D., Huang, L. (Ed.), 4th Symposium on Fluid-Structure-Sound Interactions and Control (FSSIC). Springer Singapore, Tokyo, Japan.

Bossi, F.C., Malavasi, S., 2014. Acoustic Analysis of a Rotary Control Valve, ASME 2014 Pressure Vessels and Piping Conference, Anaheim, California, USA.

Brownell, C.J., Luznik, L., Snyder, M.R., Kang, H.S., Wilkinson, C.H., 2012. In Situ Velocity Measurements in the Near-Wake of a Ship Superstructure. *Journal of Aircraft* 49 (5), 1440-1450.

CAP437, 2008. Offshore Helicopter Landing Areas: Guidance on Standards, 6th ed.

Charonko, J.J., Vlachos, P.P., 2013. Estimation of uncertainty bounds for individual particle image velocimetry measurements from cross-correlation peak ratio. *Measurement Science and Technology* 24 (6), 065301.

Cheney, B.T., Zan, S.J., 1999. CFD Code Validation Data and Flow Topology for the Technical Co-operation Program AER-TP2 Simple Frigate Shape. National Research Council Canada, Institute for Aerospace Research.

Cherry, N.J., Hillier, R., Latour, M.E.M.P., 1984. Unsteady measurements in a separated and reattaching flow. *Journal of Fluid Mechanics* 144, 13-46.

Clark, I., Devenport, W.J., Jaworski, J., Daly, C., Peake, N., Glegg, S.A., 2014. The Noise Generating and Suppressing Characteristics of Bio-Inspired Rough Surfaces, 20th AIAA/CEAS Aeroacoustics Conference. American Institute of Aeronautics and Astronautics.

Counihan, J., 1975. Adiabatic atmospheric boundary layers: A review and analysis of data from the period 1880–1972. *Atmospheric Environment* (1967) 9 (10), 871-905.

Derakhshandeh, J.F., Alam, M.M., 2019. A review of bluff body wakes. *Ocean Engineering* 182, 475-488.

Diana, G., Fiammenghi, G., Belloli, M., Rocchi, D., 2013. Wind tunnel tests and numerical approach for long span bridges: The Messina bridge. *Journal of Wind Engineering and Industrial Aerodynamics* 122, 38-49.

Djilali, N., Gartshore, I.S., 1991. Turbulent Flow Around a Bluff Rectangular Plate. Part I: Experimental Investigation. *Journal of Fluids Engineering* 113 (1), 51-59.

Dobrucali, E., Ergin, S., 2017. An investigation of exhaust smoke dispersion for a generic frigate by numerical analysis and experiment. *Proceedings of the Institution of Mechanical Engineers, Part M: Journal of Engineering for the Maritime Environment*, 1475090217742240.

Dooley, G., Ezequiel Martin, J., Buchholz, J.H.J., Carrica, P.M., 2020. Ship Airwakes in Waves and Motions and Effects on Helicopter Operation. *Computers & Fluids* 208, 104627.

Eaton, J.K., Johnston, J.P., 1982. Low Frequency Unsteadyness of a Reattaching Turbulent Shear Layer, in: Bradbury, L.J.S., Durst, F., Launder, B.E., Schmidt, F.W., Whitelaw, J.H. (Eds.), *Turbulent Shear Flows 3*. Springer Berlin Heidelberg, Berlin, Heidelberg, pp. 162-170.

Ezraty, R., 1990. Marine wind variability: Illustration and comments. *Johns Hopkins Apl Technical Digest* 11 (3-4), 392-396.

Forrest, J.S., Kaaria, C.H., Owen, I., 2016. Evaluating ship superstructure aerodynamics for maritime helicopter operations through CFD and flight simulation. *The Aeronautical Journal* 120 (1232), 1578-1603.

Forrest, J.S., Owen, I., 2010. An investigation of ship airwakes using Detached-Eddy Simulation. *Computers & Fluids* 39 (4), 656-673.

Greenwell, D., Barrett, R., 2006. Inclined Screens for Control of Ship Air Wakes, 3rd AIAA Flow Control Conference. American Institute of Aeronautics and Astronautics.

Guillaume, D.W., LaRue, J.C., 2001. Comparison of the vortex shedding behavior of a single plate and a plate array. *Experiments in Fluids* 30 (1), 22-26.

Guillaume, D.W., LaRue, J.C., 2005. Comparing the flow on the bounded and unbounded sides of a plate. *International Journal of Heat and Mass Transfer* 48 (7), 1384-1387.

Healey, J.V., 1987. THE PROSPECTS FOR SIMULATING THE HELICOPTER/SHIP INTERFACE. *Naval Engineers Journal* 99 (2), 45-63.

Healey, J.V., 1992. Establishing a database for flight in the wakes of structures. *Journal of Aircraft* 29 (4), 559-564.

Hertwig, D., Gough, H.L., Grimmond, S., Barlow, J.F., Kent, C.W., Lin, W.E., Robins, A.G., Hayden, P., 2019. Wake Characteristics of Tall Buildings in a Realistic Urban Canopy. *Boundary-Layer Meteorology* 172 (2), 239-270.

Holman, J.P., 2012. *Experimental Methods for Engineers*. McGraw-Hill/Connect Learn Succeed.

Howe, M.S., 1986. Attenuation of sound due to vortex shedding from a splitter plate in a mean flow duct. *Journal of Sound and Vibration* 105 (3), 385-396.

Howe, M.S., 1997a. Edge, cavity and aperture tones at very low Mach numbers. *Journal of Fluid Mechanics* 330, 61-84.

Howe, M.S., 1997b. Influence of cross-sectional shape on the conductivity of a wall aperture in mean flow. *Journal of Sound and Vibration* 207 (5), 601-616.

Howe, M.S., 1998. *Acoustics of fluid-structure interactions*. Cambridge University Press.

Hu, H., Yang, Z., Sarkar, P., 2012. Dynamic wind loads and wake characteristics of a wind turbine model in an atmospheric boundary layer wind. *Experiments in Fluids* 52 (5), 1277-1294.

Irwin, H.P.A.H., 1981. The design of spires for wind simulation. *Journal of Wind Engineering and Industrial Aerodynamics* 7 (3), 361-366.

Jaworski, J.W., Peake, N., 2013. Aerodynamic noise from a poroelastic edge with implications for the silent flight of owls. *Journal of Fluid Mechanics* 723, 456-479.

Johns, M.K., Healey, J.V., 1989. The Airwake of a DD-963 Class Destroyer. *Naval Engineers Journal* 101 (3), 36-42.

Kääriä, C.H., Wang, Y., Padfield, G.D., Forrest, J.S., Owen, I., 2012. Aerodynamic Loading Characteristics of a Model-Scale Helicopter in a Ship's Airwake. *Journal of Aircraft* 49 (5), 1271-1278.

Kääriä, C.H., Wang, Y., White, M.D., Owen, I., 2013. An experimental technique for evaluating the aerodynamic impact of ship superstructures on helicopter operations. *Ocean Engineering* 61, 97-108.

- Kim, J., Kline, S.J., Johnston, J.P., 1980. Investigation of a Reattaching Turbulent Shear Layer: Flow Over a Backward-Facing Step. *Journal of Fluids Engineering* 102 (3), 302-308.
- Kiya, M., Sasaki, K., 1983. Structure of a turbulent separation bubble. *Journal of Fluid Mechanics* 137, 83-113.
- Knisely, C.W., 1990. Strouhal numbers of rectangular cylinders at incidence: A review and new data. *Journal of Fluids and Structures* 4 (4), 371-393.
- Lee, D., Horn, J., 2004. Analysis of Pilot Workload in the Helicopter/Ship Dynamic Interface using Time-Accurate and Stochastic Ship Airwake Models, AIAA Atmospheric Flight Mechanics Conference and Exhibit. American Institute of Aeronautics and Astronautics.
- Lee, D., Horn, J.F., 2005. Simulation of Pilot Workload for a Helicopter Operating in a Turbulent Ship Airwake. *Proceedings of the Institution of Mechanical Engineers, Part G: Journal of Aerospace Engineering* 219 (5), 445-458.
- Lee, R.G., Zan, S.J., 2005. Wind Tunnel Testing of a Helicopter Fuselage and Rotor in a Ship Airwake. *Journal of the American Helicopter Society* 50 (4), 326-337.
- Malavasi, S., Guadagnini, A., 2007. Interactions between a rectangular cylinder and a free-surface flow. *Journal of Fluids and Structures* 23 (8), 1137-1148.
- Malavasi, S., Zappa, E., 2009. Fluid-dynamic forces and wake frequencies on a tilted rectangular cylinder near a solid wall. *Meccanica* 44 (1), 91-101.
- McRuer, D.T., 1994. Interdisciplinary interactions and dynamic systems integration. *International Journal of Control* 59 (1), 3-12.
- Mills, R., Sheridan, J., Hourigan, K., 2003. Particle image velocimetry and visualization of natural and forced flow around rectangular cylinders. *Journal of Fluid Mechanics* 478, 299-323.
- Nakamura, Y., Nakashima, M., 1986. Vortex excitation of prisms with elongated rectangular, H and [vdash ] cross-sections. *Journal of Fluid Mechanics* 163, 149-169.
- Nakamura, Y., Ohya, Y., Ozono, S., Nakayama, R., 1996. Experimental and numerical analysis of vortex shedding from elongated rectangular cylinders at low Reynolds numbers 200-103. *Journal of Wind Engineering and Industrial Aerodynamics* 65 (1), 301-308.

- Nakamura, Y., Ohya, Y., Tsuruta, H., 1991. Experiments on vortex shedding from flat plates with square leading and trailing edges. *Journal of Fluid Mechanics* 222, 437-447.
- Naudascher, E., Rockwell, D., 1994. *Flow-Induced Vibrations: an Engineering Guide*. A.A. Balkema Publishers, Rotterdam, the Netherlands.
- Negri, M., Cozzi, F., Malavasi, S., 2011. Self-synchronized phase averaging of PIV measurements in the base region of a rectangular cylinder. *Meccanica* 46 (2), 423-435.
- Nie, J.H., Armaly, B.F., 2004. Reverse flow regions in three-dimensional backward-facing step flow. *International Journal of Heat and Mass Transfer* 47 (22), 4713-4720.
- Norberg, C., 1993. Flow around rectangular cylinders: Pressure forces and wake frequencies. *Journal of Wind Engineering and Industrial Aerodynamics* 49 (1), 187-196.
- Okajima, A., 1982. Strouhal numbers of rectangular cylinders. *Journal of Fluid Mechanics* 123, 379-398.
- Okajima, A., Yi, D., Sakuda, A., Nakano, T., 1997. Numerical study of blockage effects on aerodynamic characteristics of an oscillating rectangular cylinder. *Journal of Wind Engineering and Industrial Aerodynamics* 67-68, 91-102.
- Oshkai, P., Velikorodny, A., 2013. Flow-acoustic coupling in coaxial side branch resonators with rectangular splitter plates. *Journal of Fluids and Structures* 38, 22-39.
- Ota, T., Asano, Y., Okawa, J.-i., 1981. Reattachment Length and Transition of the Separated Flow over Blunt Flat Plates. *Bulletin of JSME* 24 (192), 941-947.
- Parker, R., 1966. Resonance effects in wake shedding from parallel plates: Some experimental observations. *Journal of Sound and Vibration* 4 (1), 62-72.
- Parker, R., Welsh, M.C., 1983. Effects of sound on flow separation from blunt flat plates. *International Journal of Heat and Fluid Flow* 4 (2), 113-127.
- Polsky, S., 2003. CFD Prediction of Airwake Flowfields for Ships Experiencing Beam Winds, 21st AIAA Applied Aerodynamics Conference. American Institute of Aeronautics and Astronautics.
- Pope, S.B., 2000. *Turbulent Flows*. Cambridge University Press, Cambridge.
- Raffel, M., Willert, C.E., Kompenhans, J., 2007. *Particle image velocimetry: a practical guide*. Springer Science & Business Media.

Rahimpour, M., Bossi, F.C., Barannyk, O., Malavasi, S., Oshkai, P., 2018. Flow-induced loading on and unsteady flow structure in the wake of bluff perforated plates at zero incidence. *Journal of Fluids and Structures* 81, 712-727.

Rahimpour, M., Oshkai, P., 2016. Experimental investigation of airflow over the helicopter platform of a polar icebreaker. *Ocean Engineering* 121, 98-111.

Rahimpour, M., Oshkai, P., 2019. The effects of unsteady change in wind direction on the airflow over the helicopter platform of a polar icebreaker. *Ocean Engineering* 172, 22-30.

Reddy, K.R., Toffoletto, R., Jones, K.R.W., 2000. Numerical simulation of ship airwake. *Computers & Fluids* 29 (4), 451-465.

Rhoades, M.M., 1983. A study of the airwake aerodynamics over the flight deck of an AOR model ship. Monterey, California. Naval Postgraduate School.

Rhoades, M.M., 1991. A study of the airwake aerodynamics over the flight deck of an AOR model ship. Monterey, California. Naval Postgraduate School.

Roshko, A., 1954. On the drag and shedding frequency of two-dimensional bluff bodies, NACA-TN-3169. National Advisory Committee for Aeronautics, Washington, DC, United States.

Roshko, A., 1955. On the Wake and Drag of Bluff Bodies. *Journal of the Aeronautical Sciences* 22 (2), 124-132.

Roshko, A., 1993. Perspectives on bluff body aerodynamics. *Journal of Wind Engineering and Industrial Aerodynamics* 49 (1), 79-100.

Sciacchitano, A., Wieneke, B., 2016. PIV uncertainty propagation. *Measurement Science and Technology* 27 (8), 084006.

Sezer-Uzol, N., Sharma, A., Long, L.N., 2005. Computational Fluid Dynamics Simulations of Ship Airwake. *Proceedings of the Institution of Mechanical Engineers, Part G: Journal of Aerospace Engineering* 219 (5), 369-392.

Shukla, S., Sinha, S.S., Singh, S.N., 2019. Ship-helo coupled airwake aerodynamics: A comprehensive review. *Progress in Aerospace Sciences* 106, 71-107.

Snyder, M., Kang, H., Brownell, C., Luznik, L., Miklosovic, D., Burks, J., Wilkinson, C., 2011. USNA Ship Air Wake Program Overview, 29th AIAA Applied Aerodynamics Conference. American Institute of Aeronautics and Astronautics.

Stokes, A.N., Welsh, M.C., 1986. Flow-resonant sound interaction in a duct containing a plate, II: Square leading edge. *Journal of Sound and Vibration* 104 (1), 55-73.

Suksangpanomrung, A., Djilali, N., Moinat, P., 2000. Large-eddy simulation of separated flow over a bluff rectangular plate. *International Journal of Heat and Fluid Flow* 21 (5), 655-663.

Syms, G.F., 2004. Numerical Simulation of Frigate Airwakes. *International Journal of Computational Fluid Dynamics* 18 (2), 199-207.

Syms, G.F., 2008. Simulation of simplified-frigate airwakes using a lattice-Boltzmann method. *Journal of Wind Engineering and Industrial Aerodynamics* 96 (6), 1197-1206.

Tai, T.C., Carico, D., 1995. Simulation of DD-963 ship airwake by Navier-Stokes method. *Journal of Aircraft* 32 (6), 1399-1401.

Thornber, B., Starr, M., Drikakis, D., 2010. Implicit large eddy simulation of ship airwakes. *The Aeronautical Journal* 114 (1162), 715-736.

Timmins, B.H., Wilson, B.W., Smith, B.L., Vlachos, P.P., 2012. A method for automatic estimation of instantaneous local uncertainty in particle image velocimetry measurements. *Experiments in Fluids* 53 (4), 1133-1147.

Tinney, C.E., Ukeiley, L.S., 2009. A study of a 3-D double backward-facing step. *Experiments in Fluids* 47 (3), 427-438.

Toffoletto, R., Reddy, K.R., Lewis, J., 2003. Effect of Ship Frontal Variation on the Flow Field in the Flight-Deck Region, in: Armfield, S.W., Morgan, P., Srinivas, K. (Eds.), *Computational Fluid Dynamics 2002*. Springer Berlin Heidelberg, Berlin, Heidelberg, pp. 191-196.

van Doorn, E., Dhruva, B., Sreenivasan, K.R., Cassella, V., 2000. Statistics of wind direction and its increments. *Physics of Fluids* 12 (6), 1529-1534.

Van Muijden, J., Boelens, O., van der Vorst, J., Gooden, J., 2013. Computational ship airwake determination to support helicopter-ship dynamic interface assessment, 21st AIAA Computational Fluid Dynamics Conference. American Institute of Aeronautics and Astronautics.

VardMarine, 2019. Polar Icebreaker 9 206 public report. <https://vardmarine.com/wp-content/uploads/2018/12/VARD-9-206.pdf>.

- Welsh, M.C., Stokes, A.N., Parker, R., 1984. Flow-resonant sound interaction in a duct containing a plate, part I: Semi-circular leading edge. *Journal of Sound and Vibration* 95 (3), 305-323.
- West, G.S., Apelt, C.J., 1982. The effects of tunnel blockage and aspect ratio on the mean flow past a circular cylinder with Reynolds numbers between 104 and 105. *Journal of Fluid Mechanics* 114, 361-377.
- Wieneke, B., 2015. PIV uncertainty quantification from correlation statistics. *Measurement Science and Technology* 26 (7), 074002.
- Wilkinson, C., Zan, S., Gilbert, N., Funk, J., 1998. Modelling and Simulation of Ship Air Wakes for Helicopter Operations, Fluid dynamics problems of vehicles operating near or in the air-sea interface, Amsterdam, The Netherlands.
- Woodson, S., Ghee, T., 2005. A Computational and Experimental Determination of the Air Flow Around the Landing Deck of a U.S. Navy Destroyer (DDG), 23rd AIAA Applied Aerodynamics Conference. American Institute of Aeronautics and Astronautics.
- Wynanski, I., Champagne, F., Marasli, B., 1986. On the large-scale structures in two-dimensional, small-deficit, turbulent wakes. *Journal of Fluid Mechanics* 168, 31-71.
- Yesilel, H., Edis, F.O., 2007. Ship Airwake Analysis by CFD Methods. AIP Conference Proceedings 936 (1), 674-677.
- Zan, S., 2001. Surface flow topology for a simple frigate shape. *Canadian Aeronautics and Space Journal* 47 (1), 33-43.
- Zan, S., 2002. Experimental Determination of Rotor Thrust in a Ship Airwake. *Journal of the American Helicopter Society* 47.
- Zan, S., Syms, G., Cheney, B., 1998. Analysis of patrol frigate air wakes, Fluid dynamics problems of vehicles operating near or in the air-sea interface, Amsterdam, The Netherlands, pp. 1-7.
- Zhou, Y., Kareem, A., 2002. Definition of Wind Profiles in ASCE 7. *Journal of Structural Engineering* 128 (8), 1082-1086.

## Appendix A Uncertainty of PIV measurements

In the present research, the velocity fields were obtained by application of PIV, which is associated with two main types of errors, namely (i) systematic (bias) and (ii) random (precision) errors. The systematic error is generally caused by the measuring instruments (Holman, 2012). For the flow measurement technique of PIV, the systematic error is attributed to the optical system calibration, implementation of a cross-correlation method, as well as the algorithm implemented for peak-finding (Wieneke, 2015). The random errors can be attributed to the unknown changes in the experimental conditions, which usually follow a certain statistical distribution. The random errors are mainly due to the finite sample size and are commonly quantified by a measure of the scatter in the measured data, such as sample standard deviation of and cross-correlation coefficients between measured quantities (Sciacchitano and Wieneke, 2016).

Several methods have been developed to quantify the systematic error involved in the instantaneous PIV measurements, namely uncertainty surface (Timmins et al. 2012) and peak ratio method (Charonko and Vlachos, 2013). In the present work, a more recent method of the correlation statistics (Wieneke, 2015) was used. In this method, the uncertainty of the displacement vector, hence the instantaneous velocity vector fields, is obtained by deriving a relationship between the standard deviation of intensity differences in each interrogation window and the expected asymmetry of the correlation peak. This correlation statistics method and the related algorithms are embedded in the software used for calculating the velocity fields, LaVision DaVis version 8.0, which allowed the calculation of the uncertainty of the instantaneous data simultaneous with the post-processing the PIV images. In the present research, it was found that maximum uncertainty in the instantaneous velocity field at the inlet of the water channel (used to obtain the characteristic velocity) was 2%. Moreover, the maximum uncertainty of the instantaneous velocity components obtained over the helicopter platform of the scaled model of the CCG icebreaker was associated with the vertical velocity component of velocity and was found to be 6.5% of the characteristic velocity. The maximum uncertainty of the instantaneous velocity fields in the near wake of the perforated plates was observed for the transverse velocity components (5.4% of the characteristic velocity).

In this research, the random uncertainty, i.e. statistical uncertainty associated with the sampling of random processes, was quantified following the work of Benedict and Gould (1996) and Sciacchitano and Wieneke (2016):

$$\varepsilon_{\langle u \rangle} = \frac{\sigma_u}{\sqrt{N}}, \quad \varepsilon_{\langle v \rangle} = \frac{\sigma_v}{\sqrt{N}}, \quad \varepsilon_{\langle w \rangle} = \frac{\sigma_w}{\sqrt{N}}, \quad (\text{A-1})$$

$$\varepsilon_{\sigma_u} = \frac{\sigma_u}{\sqrt{2(N-1)}}, \quad \varepsilon_{\sigma_v} = \frac{\sigma_v}{\sqrt{2(N-1)}}, \quad \varepsilon_{\sigma_w} = \frac{\sigma_w}{\sqrt{2(N-1)}}, \quad (\text{A-2})$$

$$\varepsilon_{R_{uu}} = \sigma_u^2 \sqrt{\frac{1 + \rho_{uu}^2}{N-1}}, \quad \varepsilon_{R_{ww}} = \sigma_w^2 \sqrt{\frac{1 + \rho_{ww}^2}{N-1}}, \quad \varepsilon_{R_{uw}} = \sigma_u \sigma_w \sqrt{\frac{1 + \rho_{uw}^2}{N-1}}. \quad (\text{A-3})$$

Here,  $\varepsilon_{\langle u \rangle}$ ,  $\varepsilon_{\langle v \rangle}$  and  $\varepsilon_{\langle w \rangle}$  are the random uncertainty for the time-averaged components of the velocity vector,  $\varepsilon_{\sigma_u}$ ,  $\varepsilon_{\sigma_v}$  and  $\varepsilon_{\sigma_w}$  are the random uncertainty for the standard deviation of the components of the velocity vector, and  $\varepsilon_{R_{uu}}$ ,  $\varepsilon_{R_{ww}}$  and  $\varepsilon_{R_{uw}}$  are the random uncertainty for the components of the Reynolds stress tensor. Moreover,  $\sigma_u$ ,  $\sigma_v$  and  $\sigma_w$  are standard deviation of the velocity components, and  $\rho_{uu}$ ,  $\rho_{ww}$  and  $\rho_{uw}$  are the correlation coefficients for components of the velocity vector. Furthermore, considering the propagation of uncertainty, the uncertainty of the turbulence intensity was calculated as:

$$\varepsilon_{I_u} = \left[ \left( \frac{\varepsilon_{\sigma_u}}{U} \right)^2 + \left( \frac{\sigma_u}{U^2} \varepsilon_U \right)^2 \right]^{1/2}, \quad \varepsilon_{I_w} = \left[ \left( \frac{\varepsilon_{\sigma_w}}{U} \right)^2 + \left( \frac{\sigma_w}{U^2} \varepsilon_U \right)^2 \right]^{1/2}. \quad (\text{A-4})$$

For investigation of the wake of the superstructure of the CCG icebreaker, the maximum uncertainty of the inflow velocity at the entrance of the water channel, i.e. the characteristic velocity, was found to be 1.1%, which was observed for the highest inflow velocity,  $U = 1.17$  m/s. Moreover, for the case of stationary scaled model, the maximum uncertainty of the velocity field over the helicopter platform was observed for the streamwise velocity component associated with the simulated ABL, which was 1.9% of the characteristic velocity. The maximum uncertainty for the components of the Reynolds

stress tensor were also observed for the streamwise velocity components observed for the simulated ABL and was evaluated at 1.5%. The maximum uncertainty of the turbulence intensity was also associated with the streamwise velocity components, which was 2.0%. For the case of the scaled model exposed to the transient change of the inflow direction, the maximum uncertainty for the phase-averaged velocity field and the associated turbulence intensity were associated with streamwise velocity component and were found to be 3% and 6% respectively.

The maximum uncertainty of the velocity field in the near wake of the perforated plates was observed for the highest Reynolds number, i.e. characteristic velocity of  $U = 0.55$  m/s. It was found that the maximum uncertainty of 0.5% and 0.3% of the characteristic velocity were associated with streamwise and transverse component of velocity respectively. Moreover, the maximum uncertainty in calculation of  $v_{rms}$  was 0.5% of the characteristic velocity.

## Appendix B Permission letters for copyrighted materials

Permission to reprint the following published material:

M. Rahimpour, P. Oshkai, 2016. Experimental investigation of airflow over the helicopter platform of a polar icebreaker, *Ocean Engineering*, 121, 98-111.

DOI: 10.1016/j.oceaneng.2016.05.023.



Dear Mostafa Rahimpour

We hereby grant you permission to reprint the material detailed below at no charge **in your thesis** subject to the following conditions:

1. If any part of the material to be used (for example, figures) has appeared in our publication with credit or acknowledgement to another source, permission must also be sought from that source. If such permission is not obtained then that material may not be included in your publication/copies.
2. Suitable acknowledgment to the source must be made, either as a footnote or in a reference list at the end of your publication, as follows:  
  
 “This article was published in Publication title, Vol number, Author(s), Title of article, Page Nos, Copyright Elsevier (or appropriate Society name) (Year).”
3. Your thesis may be submitted to your institution in either print or electronic form.
4. Reproduction of this material is confined to the purpose for which permission is hereby given.
5. This permission is granted for non-exclusive world **English** rights only. For other languages please reapply separately for each one required. Permission excludes use in an electronic form other than submission. Should you have a specific electronic project in mind please reapply for permission
6. This includes permission for the Library and Archives of Canada to supply single copies, on demand, of the complete thesis. Should your thesis be published commercially, please reapply for permission.

**Elsevier Limited, a company registered in England and Wales with company number 1982084, whose registered office is The Boulevard, Langford Lane, Kidlington, Oxford, OX5 1GB, United Kingdom.**

04 Jul 2018 7:55pm

Question	Answer
Title	Mr.
First name	Mostafa
Last name	Rahimpour
Institute/company	University of Victoria
Address	Department of Mechanical Engineering
Post/Zip Code	V8P5C2
City	Victoria
State/Territory	British Columbia
Country	Canada
Please select the type of publication	Journal
Journal - Title	Ocean Engineering
Journal - ISSN	0029-8018
Journal - Volume	121
Journal - Issue	July 2016
Journal - Year	2016
Journal - Pages from	98
Journal - Pages to	111
Journal - Author	Mostafa Rahimpour, Peter Oshkai
Journal - Article Title	Experimental investigation of airflow over the helicopter platform of a polar icebreaker
I would like to use (please select one of the following options)	Full article/chapter
If using figures/tables or illustrations please specify the quantity	
If using excerpts please provide a total word count	
Are you the author of the Elsevier material?	Yes
If not, is the Elsevier author involved with your project?	Yes
If yes, please provide details of how the Elsevier author is involved	I am the first author of the article.
In what format will you use the material?	Print and Electronic

Question	Answer
Will you be translating the material? If yes, please specify the languages	No

---

Elsevier Limited. Registered Office: The Boulevard, Langford Lane, Kidlington, Oxford, OX5 1GB, United Kingdom, Registration No. 1982084, Registered in England and Wales.

Permission to reprint the following published material:

M. Rahimpour, P. Oshkai, 2019. The effects of unsteady change in wind direction on the airflow over the helicopter platform of a polar icebreaker, *Ocean Engineering*, 172, 22-30. DOI: 10.1016/j.oceaneng.2018.11.049.



Dear Mostafa Rahimpour

We hereby grant you permission to reprint the material detailed below at no charge **in your thesis** subject to the following conditions:

1. If any part of the material to be used (for example, figures) has appeared in our publication with credit or acknowledgement to another source, permission must also be sought from that source. If such permission is not obtained then that material may not be included in your publication/copies.
2. Suitable acknowledgment to the source must be made, either as a footnote or in a reference list at the end of your publication, as follows:  
  
“This article was published in Publication title, Vol number, Author(s), Title of article, Page Nos, Copyright Elsevier (or appropriate Society name) (Year).”
3. Your thesis may be submitted to your institution in either print or electronic form.
4. Reproduction of this material is confined to the purpose for which permission is hereby given.
5. This permission is granted for non-exclusive world **English** rights only. For other languages please reapply separately for each one required. Permission excludes use in an electronic form other than submission. Should you have a specific electronic project in mind please reapply for permission
6. This includes permission for the Library and Archives of Canada to supply single copies, on demand, of the complete thesis. Should your thesis be published commercially, please reapply for permission.

**Elsevier Limited, a company registered in England and Wales with company number 1982084, whose registered office is The Boulevard, Langford Lane, Kidlington, Oxford, OX5 1GB, United Kingdom.**

19 Feb 2019 10:30am

Question	Answer
Title	Mr.
First name	Mostafa
Last name	Rahimpour
Institute/company	University of Victoria
Address	Department of Mechanical Engineering
Post/Zip Code	V8P5C2
City	Victoria
State/Territory	British Columbia
Country	Canada
Please select the type of publication	Journal
Journal - Title	Ocean Engineering
Journal - ISSN	0029-8018
Journal - Volume	172
Journal - Issue	January 2019
Journal - Year	2019
Journal - Pages from	22
Journal - Pages to	30
Journal - Author	Mostafa Rahimpour, Peter Oshkai
Journal - Article Title	The effects of unsteady change in wind direction on the airflow over the helicopter platform of a polar icebreaker
I would like to use (please select one of the following options)	Full article/chapter
If using figures/tables or illustrations please specify the quantity	
If using excerpts please provide a total word count	
Are you the author of the Elsevier material?	Yes
If not, is the Elsevier author involved with your project?	Yes
If yes, please provide details of how the Elsevier author is involved	I am the first author of the article.
In what format will you use the material?	Print and Electronic

Question	Answer
----------	--------

Will you be translating the material? No	
--	--

If yes, please specify the languages	
--------------------------------------	--

---

Elsevier Limited. Registered Office: The Boulevard, Langford Lane, Kidlington, Oxford, OX5 1GB, United Kingdom, Registration No. 1982084, Registered in England and Wales.

Permission to reprint the following published material:

M. Rahimpour, F.C. Bossi, O. Barannyk, S. Malavasi, P. Oshkai, 2018. Flow-induced loading on and unsteady flow structure in the wake of bluff perforated plates at zero incidence, *Journal of Fluids and Structures*, 81, 712-727.

DOI: /10.1016/j.jfluidstructs.2018.06.007.



Dear Mostafa Rahimpour

We hereby grant you permission to reprint the material detailed below at no charge **in your thesis** subject to the following conditions:

1. If any part of the material to be used (for example, figures) has appeared in our publication with credit or acknowledgement to another source, permission must also be sought from that source. If such permission is not obtained then that material may not be included in your publication/copies.
2. Suitable acknowledgment to the source must be made, either as a footnote or in a reference list at the end of your publication, as follows:  
  
“This article was published in Publication title, Vol number, Author(s), Title of article, Page Nos, Copyright Elsevier (or appropriate Society name) (Year).”
3. Your thesis may be submitted to your institution in either print or electronic form.
4. Reproduction of this material is confined to the purpose for which permission is hereby given.
5. This permission is granted for non-exclusive world **English** rights only. For other languages please reapply separately for each one required. Permission excludes use in an electronic form other than submission. Should you have a specific electronic project in mind please reapply for permission
6. This includes permission for the Library and Archives of Canada to supply single copies, on demand, of the complete thesis. This includes permission for UMI to

supply single copies, on demand, of the complete thesis. Should your thesis be published commercially, please reapply for permission.

**Elsevier Limited, a company registered in England and Wales with company number 1982084, whose registered office is The Boulevard, Langford Lane, Kidlington, Oxford, OX5 1GB, United Kingdom.**

04 Jul 2018 7:52pm

Question	Answer
Title	Mr.
First name	Mostafa
Last name	Rahimpour
Institute/company	University of Victoria
Address	Department of Mechanical Engineering
Post/Zip Code	V8P5C2
City	Victoria
State/Territory	British Columbia
Country	Canada
Please select the type of publication	Journal
Journal - Title	Journal of Fluids and Structures
Journal - ISSN	0889-9746
Journal - Volume	81
Journal - Issue	August 2018
Journal - Year	2018
Journal - Pages from	712
Journal - Pages to	727
Journal - Author	Mostafa Rahimpour, Filippo Carlo Bossi, Oleksandr Barannyk, Stefano Malavasi, Peter Oshkai
Journal - Article Title	Flow-induced loading on and unsteady flow structure in the wake of bluff perforated plates at zero incidence
I would like to use (please select one of the following options)	Full article/chapter
If using figures/tables or illustrations please specify the quantity	
If using excerpts please provide a total word count	
Are you the author of the Elsevier material?	Yes
If not, is the Elsevier author involved with your project?	Yes

Question	Answer
If yes, please provide details of how the Elsevier author is involved	I am the first author of the article.
In what format will you use the material?	Print and Electronic
Will you be translating the material? No	
If yes, please specify the languages	
Information about your proposed use	Reuse in a thesis/dissertation

---

Elsevier Limited. Registered Office: The Boulevard, Langford Lane, Kidlington, Oxford, OX5 1GB, United Kingdom, Registration No. 1982084, Registered in England and Wales.